The University Of Sheffield

Department of Materials Science and Engineering

Structure-Property Relations in Rare Earth Doped $BiFeO_3$

Thesis by: **Sarah Karimi**

In partial fulfilment of the requirements for the degree of
Doctor of Philosophy

Thesis Supervisor: **Prof. I. M. Reaney**

Spring 2011

To My parent Ashraf & Bashir

To Andrew

تقدیم به مامان و بابا که همیشه پشتیبان من بوده اند.

تقدیم به شریک زندگیم که در تمام مراحل تحصیل دکترا همراه و یاورم بود.

و

با تشکر از همه دوستان عزیزم که سال های درس و مدرسه را به یادماندنی کردند.

Abstract

RE-doped $BiFeO_3$ (RE = La, Nd, Sm, Gd) compositions have been produced and investigated with a view to establishing a broad overview of their crystal chemistry and domain structure. For less than 10% RE dopant, the perovskite phase in all compositions could be indexed according to the rhombohedral, *R3c* cell of $BiFeO_3$. For La, Nd and Sm doped compositions with more than 15% dopant, a new antipolar phase was stabilised similar in structure to $PbZrO_3$ *Pbam* symmetry with a $\sqrt{2}a_c, 2\sqrt{2}a_c, 4a_c$ unit cell where a_c is the psuedocubic unit cell. The orthoferrite, *Pnma* structure was present in all RE-doped $BiFeO_3$ compounds with higher dopant concentration. The compositional window over which the $PbZrO_3$-like phase was stable increased with increasing end-member tolerance factor, t (effectively controlled by the RE ionic radius). On heating, the $PbZrO_3$-like phase transformed to the orthoferrite, *Pnma* structure. T_C for all compositions decreased with decreasing A-site, average ionic polarizabilty and end member tolerance factor. For compositions with *R3c* symmetry, superstructure and orientational and translational (anti-phase) domains were observed in a manner typical of an anti-phase tilted, ferroelectric perovskite. For the new $PbZrO_3$-like phase orientational domains were observed along with antiphase boundaries associated with quadrupling of the unit cell due to the antipolar displacements of the Bi/RE-ions

Neutron powder diffraction was used to determine changes in the nuclear and magnetic structures across the phase transitions that relate the high-temperature non-polar *(Pnma)* to the low temperature polar *(R3c)* and anti-polar *(Pbam)* structures, respectively. The high-temperature *Pnma* phase has a $\sqrt{2}a_c,\sqrt{2}a_c,2a_c$ cell with an $a^-a^-c^+$ octahedral tilting. The low-temperature polar *R3c* structure is similar to the ß-phase of pure $BiFeO_3$ and is rhombohedral with $a^-a^-a^-$ octahedral rotations and cation displacements along the peudocubic [111] direction. Although electron diffraction revealed weak additional doubling along *c* (denoted by the appearance of ¼{00l} in addition to ¼{110} reflections) of the $PbZrO_3$ cell, Neutron and X-ray diffraction could not reliably refine a larger cell. This is attributed to the weak intensity of the ¼{001} reflections and the short coherence length of the $4a_c$ modulation in the *c*-direction.

The transitions from the high temperature *Pnma* phase to both low temperature phases are accompanied by a large discontinuous expansion of the lattice volume in the low-temperature structure. The *Pnma* to *R3c* transition occurs in the paramagnetic state and generates no detectable changes in the magnetic structure. In contrast, the *Pnma* to *Pbam* transition, which occurs in the magnetic state, is accompanied by abrupt 90 ° reorientation of the magnetic dipoles. Coupling between the nuclear and magnetic structures is manifested in a significant magnetization anomaly. The dielectric properties were studied as a function of temperature but no anomalies were recorded that were coincident with the structural phase transitions observed by differential

scanning calorimetry. The absence of peaks in permittivity at T_C was attributed to high conductivity with space charge polarisation dominating the dielectric response.

Acknowledgements

I would love to thank my supervisor Prof. I. M. Reaney for his support and guidance all through my not very easy years PhD.

Thanks to Dr. I. Levin, Dr. J. Pokorny, Dr. T. Comyn, Dr. S. Miao, Dr. Y. Han and Prof. J. Hlinka for the research collaborations and Prof. D. C. Sinclair and Prof. A. J. Bell for useful discussions.

Thanks to all academic, technical and secretarial staff at the Department of Material Science and Engineering specially Dr. I. Sterianou, Mr. A. Mould, Ms. K. Burton and Ms. A. Newbould.

Thanks to my colleagues and friends specially Dr. B. Zalinska, Dr. I. Sterianou and Dr. T. Sebastian for making my time in Sheffield as memorable as possible especially with our regular dinners, movie nights, parties and barbeques.

Contents

Chapter 1: Introduction

$BiFeO_3$ is a rhombohedrally distorted perovskite with space group *R3c* at room temperature and an $a^-a^-a^-$ tilt system in which the FeO_6 octahedra are rotated in anti-phase around the rhombohedral axis. The cations displace off their centre of symmetry along $[111]_p$ direction with the Bi^{3+} ions having a larger displacement due to the active lone pair electrons and this results in the O^{2-} ions being effectively four-fold coordinated to two Bi^{3+} ions and two Fe^{3+} ions. [Michel *et al.*, 1969a, Sosnowska *et al.*, 1982, Karimi *et al.*, 2009a]

$BiFeO_3$ is ferroelectric below T_C ($\approx$ 830 °C) and although based on the theoretical calculations, the spontaneous polarisation in $BiFeO_3$ is expected to be high due to the large displacements of the cations, it does not exhibit a saturated polarisation vs. electric field loop due to a combination of the high T_C and conductivity. [Kumar *et al.*, 2000a, Neaton *et al.*, 2005, Teague *et al.*, 1970]

$BiFeO_3$ is antiferromagnetic below T_N = 370 °C and the magnetic ordering is a cycloidal spiral in the $[110]_h$ direction with a period of λ = 620 Å within a $(110)_h$ spin rotation plane. The presence of a space modulated spin structure is considered to inhibit the linear magnetoelectric effect. [Fischer *et al.*, 1980, Kubel and Schmid, 1990, Sosnowska *et al.*, 1996]

$BiFeO_3$ has gained considerable importance both technologically and scientifically because of the coexistence of ferroelectric and anti-ferromagnetic ordering and the magnetoelectric coupling between spin and charge which gives it a tremendous potential for applications in the field of information storage, sensing and actuation, etc. [Fedulov *et al.*, 1964, Hill, 2000]

Partial substitution of Bi^{3+} ions by rare earth ions, RE^{3+}, has been shown to improve ferroelectric properties and magnetization by eliminating impurity phases and reputedly destroying the cycloidal spin structure resulting in uniform canted antiferromagnetic ordering which increases the magnetization. [Das *et al.*, 2006, Lee *et al.*, 2006, Zhang *et al.*, 2006b, Nalwa and Garg, 2008, Nalwa *et al.*, 2008a, Uniyal and Yadav, 2008]

To predict the behaviour of $BiFeO_3$ as a function RE concentration, comparisons with other systems, such as $Pb(Zr,Ti)O_3$, are potentially useful. In PZT, the larger less polarisable Zr^{4+} substitutes for Ti^{4+} ions decreasing the tolerance factor, t, and ferroelectric T_C and increasing the driving force for octahedral rotation which ultimately transforms the structure from ferroelectric rhombohedral to the antiferroelectric orthorhombic. By analogy with PZT, the reduction of polarisability by RE substitution is also likely to induce a transition from polar to antipolar order in $BiFeO_3$ before ultimately transforming the structure to that of the orthoferrite RE endmember phase. [Michel et al., 1969a, Jaffe *et al.*, 1971, Woodward, 2004, Karimi et al., 2009a, Karimi *et al.*, 2009b]

Despite the simple crystal chemistry, there is a significant confusion in the scientific literature as to the phase evolution within $REFeO_3$-$BiFeO_3$ solid solutions. This study attempts to clarify the phase evolution and establish a coherent set of sstructure property relations for RE doped $BiFeO_3$.

Chapter 2: Literature Review

2.1. Oxide Perovskites

A rare natural mineral, perovskite $CaTiO_3$, has given name to a structural class in which extensive range of materials adopt the perovskite structure or derivatives of it. The general formula of perovskites is: ABX_3 where A and B are cations and X the anion which is mostly oxygen, ABO_3.

Oxide perovskites offer diverse range of properties from insulation to metallic conduction, ionic conduction, (anti-)ferroelectricity, (anti-)ferromagnetism and electrooptic responses. [Moulson and Herbert, 1990, Navarotsky, 1998, Mitchell, 2002]

In an ideal perovskite with the cubic structure and space group $Pm\bar{3}m$, the A cations are similar in size to O anions (1.4 Å) and occupy the cubo-octahedral 12-coordinated positions whereas the smaller B cations are in 6-coordinated octahedral sites. The O anions are surrounded by four A and two B cations. [Mitchell, 2002, Sterianou, 2008]

If the unit cell representation is chosen in which B cations occupy the body centre of the cube, O occupies the face centre positions with A cations at the corners, Figure 2.1.a. Alternatively the A cations may be placed at the body centre, B cations at the corners and Oxygens along the edges of the cube, Figure 2.1.b. [Mitchell, 2002]

The main advantage of the perovskite structure is the ability of the large 12- and smaller 6-fold co-ordinated sites to accommodate a wide range of cations of different size and charge. Consequently, materials adopting the perovskite structure may be tailored by appropriate cation substitution to give specific electrical or magnetic properties.

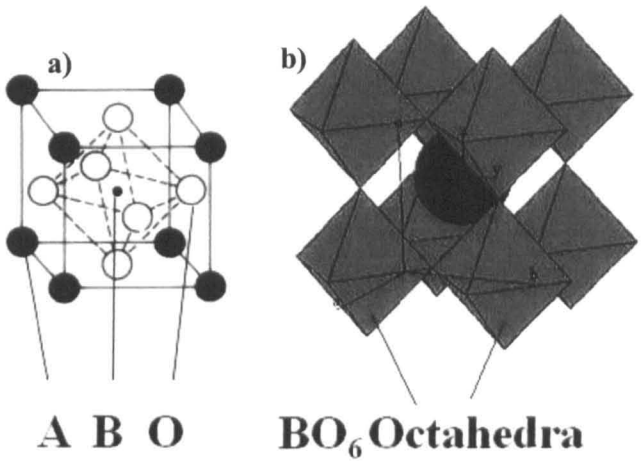

Figure 2.1. Ideal perovskite structures with a) B and b) A at the centre of the cubic unit cell. [Mitchell, 2002]

2.1.1. Tolerance factor, *t*

If the ions are considered as rigid spheres, an ideal perovskite structure will have the cations surrounded by as many anions as can touch them according to their co-ordination number. The perfectly sized ions create a structure of touching spheres where the cations cannot rattle around in the interstices between the anions. The geometrical relationship between the ions' radii in this ideal cubic perovskite structure is expressed by Equation 2.1:

$$(R_A+R_O) = \sqrt{2}(R_B+R_O) \quad (2.1)$$

However ionic radii depend on the form of bonding and electronic configuration and actual materials rarely show ideal ionic radii. Tolerance factor, *t*, may therefore be introduced as a

parameter on how well the ions fit into the perovskite structure, Equation 2.2. [Goldschmidt, 1926]

$$t = \frac{(R_A + R_O)}{\sqrt{2}\,(R_B + R_O)} \tag{2.2}$$

At $t = 1$ the structure is a perfect cubic perovskite and the ions are ideally packed. Strontium titanate, $SrTiO_3$, with tolerance factor of $t = 1.002$ is one of the closest perovskites to ideal. In general when $0.8 < t < 1.05$, the perovskite structure is usually stable but deviations from the ideal value of 1 result in structural distortions of the perovskite cell that result in interesting functional properties. [Goldschmidt, 1926, Mitchell, 2002, Woodward, 2004]

2.1.2. Distorted perovskites

The deviation from the ideal perovskite structure can be described as a result of either ionic displacement, chemical ordering, tilting of the BO_6 octahedra or combinations thereof [Jaffe *et al.*, 1971]. Generally these distortions are minor and the cubic structure will still be recognised in diffraction patterns. Line splitting, and in some cases extra lines in X-ray diffraction and extra reflections in electron diffraction will occur if the structure is distorted. These extra features in the diffraction patterns can be used to determine the true nature of the structure [Mitchell, 2002, Woodward, 2004].

Often for simplicity planes, directions and lattice parameters of the non-ideal perovskite are expressed in terms of the ideal cubic unit cell. This makes discussing a heavily distorted

perovskite or comparison between perovskites much simpler and easier. These indices are referred to as 'pseudo-cubic' and are indicated by use of a subscript '*p*' [Woodward, 2004].

Ionic Displacement:

There are two possibilities of displacement for any single ion: parallel and anti-parallel. For parallel displacement all ions shift from the cubic positions by equal vectors. For anti-parallel displacement neighbouring ions are displaced by opposite vectors. Anti-parallel displacement of cations results in superlattice reflections in X-ray, neutron and electron diffraction patterns due to the multiplication of the unit cell. [Jaffe et al., 1971, Mitchell, 2002]

Lead titanate, $PbTiO_3$, is an example of parallel displacement at room temperature. Displacement of both Ti^{4+} and O^{2-} along the $<001>_p$ direction, results in a tetragonal unit cell with one formula unit. Lead zirconate, $PbZrO_3$, has the anti-parallel displacement of Pb^{2+} cations along the $<110>_p$ direction resulting in an orthorhombic symmetry with multiple formula units.

Chemical Ordering:

Chemical ordering occurs when the A-site or B-site are occupied by more than one type of cation species resulting in complex perovskites with multiplication of the unit cell. The long-range symmetry remains the same if these mixed species distribute themselves in a disordered manner. This mostly happens when mixed cations have the same valence. The symmetry reduces when the mixed cations show an environmental preference. This mainly is the case when the mixed species have different valence and cations tend to occupy the

alternate $\{111\}_p$ planes in a ratio that depends on the formula unit of the perovskite. [Woodward, 2004]

For example lead scandium tantalate, $Pb(Sc_{1/2}Ta_{1/2})O_3$, orders in a 1:1 sequence and strontium magnesium niobate, $Sr(Mg_{1/3}Nb_{2/3})O_3$, orders in a 1:2 sequence. [Randall *et al.*, 1986, Zheng *et al.*, 2003]

BO_6 octahedral tilting:

Octahedral tilting is the mechanism responsible for the largest number of phase transitions in a perovskite. The onset of octahedral tilting usually occurs in compounds with low tolerance factor, e.g. when Sr^{2+} (1.44 Å) is substituted by Ca^{2+} (1.35 Å) in $SrTiO_3$ [Shannon and Prewitt, 1969], the cation no longer completely fills the 12-fold A-site interstice and the octahedra will try and reduce the volume of the site by rotating or tilting the octahedron which ultimately results in an orthorhombic rather than the cubic structure [Mitchell, 2002, Knudsen, 2002].

Megaw [Megaw, 1946, Megaw, 1973] initiated a way to understand the distortions of the perovskite structure which was further developed by Glazer [Glazer, 1972, Glazer, 1975]. Based on this system, combinations of component tilts about the three tetrad axes are used to describe the type of octahedral tilting. The component tilts are considered to be about the pseudocubic axes for small tilt angles. The letters a_p, b_p and c_p denote the tilt about $[100]_p$, $[010]_p$ and $[001]_p$ axis respectively. Where letters are repeated the magnitude of tilt around each axis is identical so that '*aaa*' refers to equal tilts about all three axes and '*abc*' refers to unequal tilts [Glazer, 1972].

When an octahedron tilts, the neighbouring octahedra in the plane normal to the tilt axis are constrained and tilt in the opposite sense, Figure 2.2b, but at the same time the octahedra directly above and below are not constrained and this allows tilt in one of two ways possible.

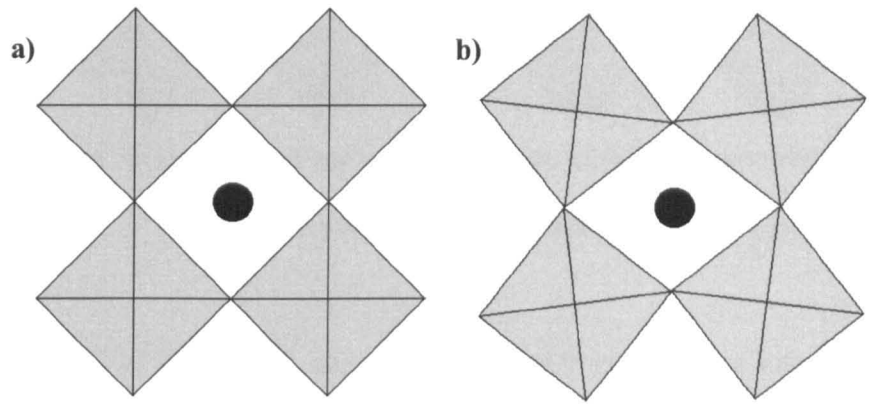

Figure 2.2. a) the untilted cubic perovskite viewed along a $<100>_p$ type axis and b) the tilted perovskite structure viewed parallel to the $<100>_p$ type tilt axis [Woodward, 2004].

The tilt is called 'in-phase' if the octahedra rotate in the same way as the central octahedron, Figure 2.3a, and it is denoted by '+' superscript. An 'anti-phase' tilt is when the octahedra above and below tilt in the opposite sense, Figure 2.3.b, which is denoted by '-' superscript. Superscript '*0*' is to show that there is no tilt about an axis, e.g. $a^0a^0c^-$ shows a perovskite with anti-phase tilting only about the pseudo-cubic c axis where $a_p = b_p < c_p$.

BO_6 octahedral tilting results in doubling of the unit cell which produces extra reflections at half-integer positions in the diffraction pattern. With respect to the doubled unit cell these reflections can be indexed with some indices odd while the main reflections all have indices even. For example, c^+ creates reflections with indices odd-odd-even where $h \neq k$, e.g. *310*, whereas c^- creates reflections with indices odd-odd-odd where $h \neq k$ e.g. *311* [Glazer, 1975].

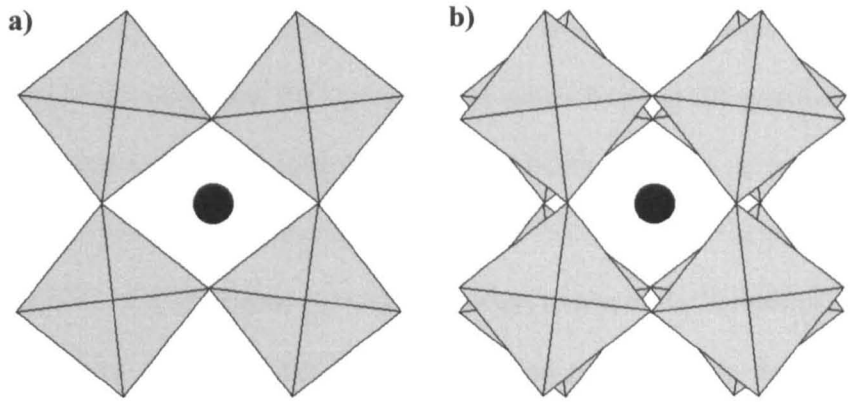

Figure2.3. a) An 'in-phase' tilted and b) an 'anti-phase' tilted perovskite view parallel to the tilt axis [Woodward, 2004].

Glazer identified 23 tilt systems and consequent space groups for a unit cell based on a pseudocubic cell doubled along each axis and containing 8 formula units, Table 2.1 [Glazer, 1972].

Later Howard and Stokes demonstrated that in tilt systems $a^+a^+a^-$, $a^+b^+b^-$, $a^+a^+c^-$, $a^+b^+c^-$ and $a^0b^+b^-$ it was not possible for the tilt transition to occur while preserving a three-dimensional network without the octahedra being distorted from the perfect structure [Glazer, 1972, Howard and Stokes, 1998]. It was also shown that the tilt systems with octahedral distortions were not uniquely linked to one space group and this was related to the way in which the octahedra were distorted. While none of the space groups assigned by Glazer to these tilt systems were incorrect, more information than solely the tilt system was required to identify the space group [Mitchell, 2002]. Woodward suggested that the tilt systems where all the A-sites are crystallographically equivalent are strongly favoured when there is only a single A-site species, resulting in the $a^+b^-b^-$ being the most common, followed by the $a^-a^-a^-$ and the $a^0a^0a^0$. When there are two or more A-site species, tilt systems with non-equivalent

A-site environments are favoured [Woodward, 1997]. Howard and Stokes argued that there could only be 15 corresponding tilt systems, since when different tilt systems result in the same space group, the tilt system with the lowest symmetry dominate. According to Howard and Stokes the unnecessary tilt systems are $a^0b^+b^-$, $a^0b^+c^+$, $a^+a^-a^-$, $a^+a^-c^-$, $a^+a^+a^-$, $a^+b^+b^-$, $a^+b^+c^-$ and $a^+b^+b^+$ and no known perovskite structures have these 'forbidden' tilt systems. Based on this idea they established a group-subgroup relationship between these tilt systems/space groups where a tilt system is considered a subgroup of another tilt system when it can be obtained by an infinitesimal change to another, Figure 2.4 [Howard and Stokes, 1998].

Table 2.1. Examples of tilt systems (*e* = even, *o* = odd indices) [Glazer, 1972, Glazer, 1975, Knudsen, 2002].

Tilt system	**Symbol**	**Reflections**	**Multiple cell**	**Relative pseudocubic unit cell parameters**	**Space group**
Three-tilt	$a^-a^-a^-$	*eee, ooo (k≠l)*	$2a_p$x$2b_p$x$2c_p$	$a_p=c_p=c_p$ $\alpha=\beta=\gamma\neq90^o$	*R3c*
Two-tilt	$a^0b^+b^+$	*eee, oeo (h≠l)*	$2a_p$x$2b_p$x$2c_p$	$a_p<b_p=c_p$	*I4/mmm*
One-tilt	$a^0a^0c^-$	*eee, ooo (h≠k)*	$2a_p$x$2b_p$x$2c_p$	$a_p=b_p<c_p$	*F4/mcm*
Zero-tilt	$a^0a^0a^0$	*eee*	a_pxb_pxc_p	$a_p=b_p=c_p$	*Pm3m*

It should be noted that although according to the group-subgroup relationship direct transitions from *R3c* to *Pnma* are not permitted, they are commonly observed in perovskites with rare earth elements in the A-site [Mitchell, 2002, Knudsen, 2002].

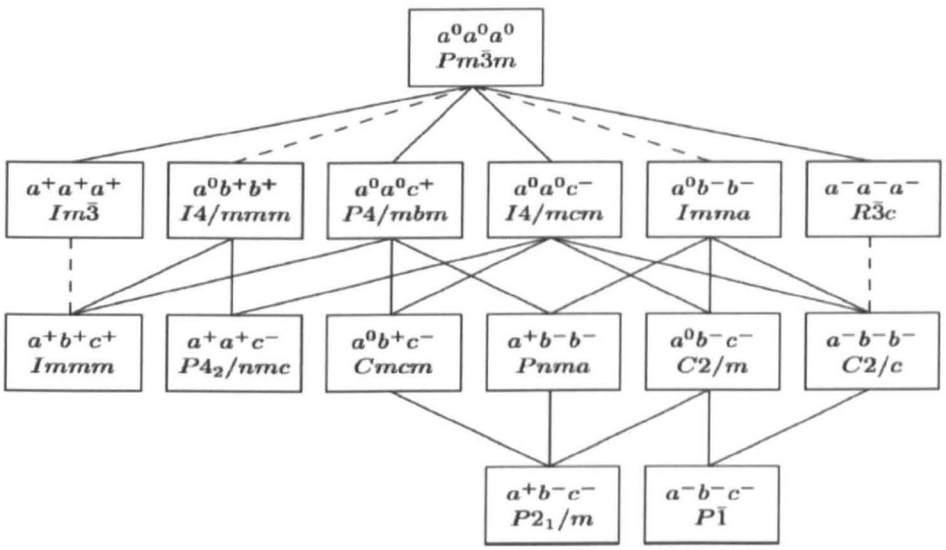

Figure 2.4. The group-subgroup relationship between the 15 perovskite space groups/ tilt systems where a dashed line joining two space groups indicates that the corresponding phase transition has a discontinuous nature [Howard and Stokes, 1998].

Generally the perovskite phase is stable if t is close enough to one. However as t decreases the A-site cations become too small for the cuboctahedral sites. With a tilt occurring, the volume of the interstice reduces and the structural stability improves. Reaney et al. showed, Figure 2.5, that perovskites with $0.985 < t < 1.06$ at room temperature have untilted structures. With $0.964 < t < 0.985$ at room temperature perovskites have anti-phase tilt and with $t < 0.964$ they are expected to have in-phase and anti-phase tilting at room temperature [Reaney *et al.*, 1994].

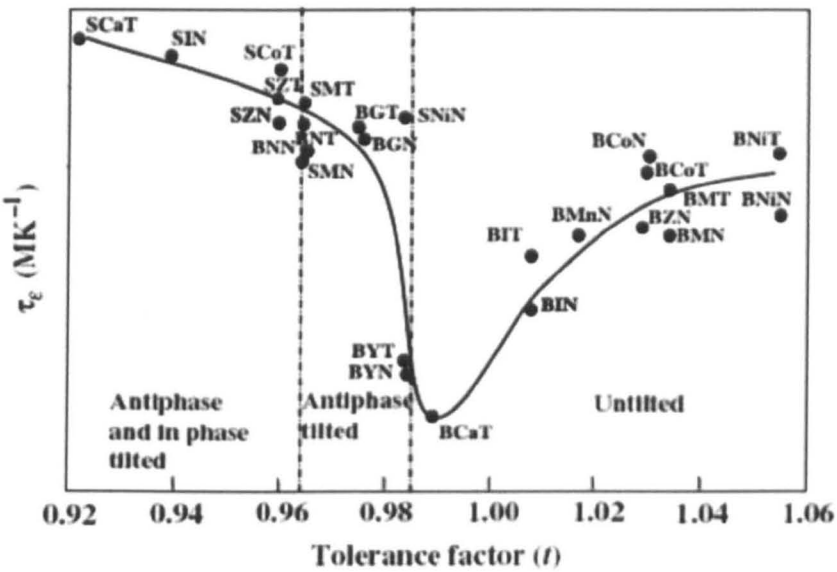

Figure 2.5. Effect of tolerance factor on octahedral tilting in perovskites with Ba or/and Sr on the A-site and mixed B-sites [Reaney *et al.*, 1994].

2.2. Characterisation of Perovskites

2.2.1. X-ray Diffraction

Long range order and lattice constants are best obtained by X-ray single crystal and powder diffraction methods. X-ray powder diffraction patterns provide the simplest ways of identifying perovskites and showing the deviations from the ideal cubic *Pm-3m* symmetry. X-ray diffraction patterns for the ideal perovskite are relatively simple and show an alternating sequence of strong $(h+k+l) = 2n$ and weak $(h+k+l) \neq 2n$ lines. Regardless of whether or not the perovskite is distorted, these patterns of reflections are characteristic of all perovskite-type compounds and account for their strong pseudo-symmetry. The intensity of weak reflections decreases as the difference (Δ_Z) between the atomic numbers of the cations and the total number of electrons in the perovskite increases. This effect is more evident with respect to the intensity of the *111* reflection relative to the *110* and *200* reflections. Usually the strongest line in a cubic perovskite X-ray diffraction pattern is the *110* reflection, Figure 2.6.A [Mitchell, 2002].

2.2.2. Neutron Diffraction

X-ray and neutron diffraction together can be used to determine the crystal structure of perovskite-type compounds as each technique provides data on different aspects of the structure but as neutron diffraction facilities are not always readily available, perovskites are more commonly characterized by X-ray diffraction methods.

Neutron diffraction provides better signal to background ratio than X-ray and it allows better recognition of weak superlattice reflections. The use of neutron diffraction becomes more important for investigating the superlattice peaks originated from displacement of anions, establishing the anion location and identification of the space group [Mitchell, 2002]. The low atomic scattering factor for oxygen makes anion disorder in perovskites very difficult to recognize by X-ray diffraction. Anion positions, bond lengths and displacement parameters are best determined by neutron powder diffraction [West, 1999, Mitchell, 2002].

Neutron diffraction patterns are characterised by major *111*, *311*, *211*, and *222* reflections due to the presence of close-packed layers of anions lying along *{111}* and *{100}* planes, Figure 2.6.B. In neutron diffraction the *110* reflection is weak and *220* and *420* reflections are strong, which is in contrast with X-ray patterns [Mitchell, 2002].

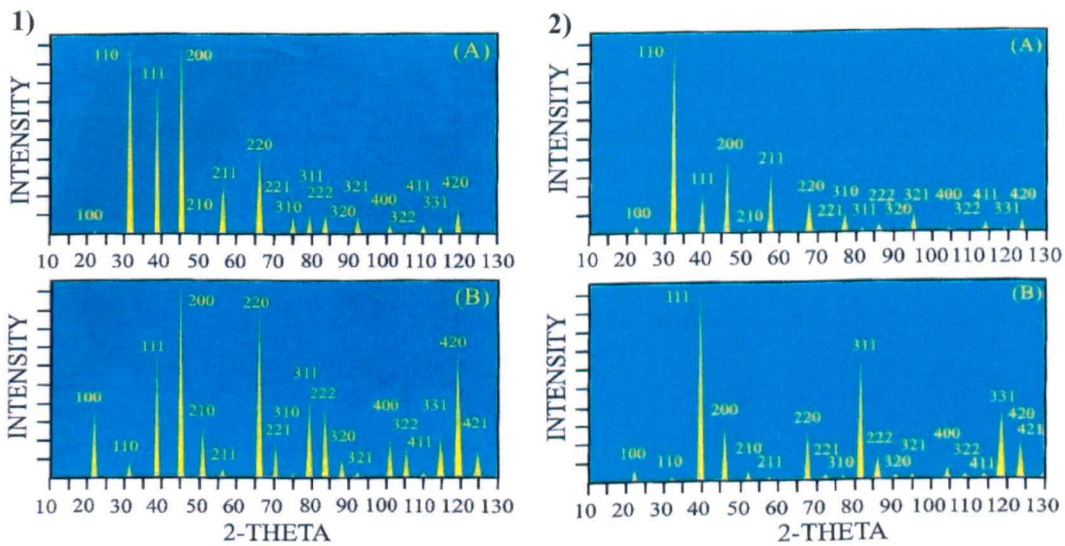

Figure 2.6. Calculated A) X-ray and B) Neutron diffraction patterns of 1) $KMgF_3$ and 2) $SrTiO_3$ perovskite [Mitchell, 2002].

2.2.3. Electron Diffraction

Electron diffraction plays a great role in the study of perovskites. Electron diffraction provides greater clarity for studying single domain data and weak cell doubling phenomena in perovskites in comparison with X-ray or neutron diffraction [Woodward *et al.*, 2006]. Effects of structural changes in perovskites on their electron diffraction patterns have been comprehensively reviewed by Reaney and co-workers who extended Glazer's general diffraction rules by taking the dynamical nature of electron diffraction into account which can generate reflections forbidden by the space group but not by the point group symmetry [Glazer, 1972, Reaney et al., 1994, Reaney, 1996].

Fundamental Reflections:

Fundamental reflection patterns contain the simple cubic prototype reflections and they appear in diffraction patterns from every perovskite, Figure 2.7. All the $<100>_p$ type diffraction patterns are identical for an ideal perovskite and this is the same for the $<110>_p$ and $<111>_p$ type diffractions [Woodward, 2004].

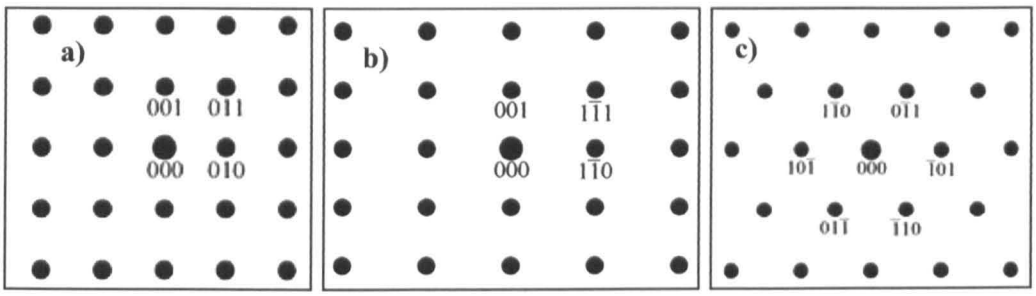

Figure 2.7. Fundamental reflections in electron diffraction patterns of the cubic perovskite prototype, observed along the principal zone axes: a) $[100]_p$, b) $[110]_p$, and c) $[111]_p$ [Woodward, 2004].

Superstructure Reflections:

Structural distortions cause fundamental reflections to move relative to each other. However, when a distortion leads to multiplication of the unit cell additional spots appear in the diffraction pattern. Depending on the nature of the corresponding distortion, their zone axis and locations relative to the fundamental spots change [Woodward, 2004].

Anti-phase tilting of the BO_6 octahedra causes the appearance of spots of type $\frac{1}{2}\{ooo\}_p$ (where '*o*' refers to an odd number) only in $\langle 110\rangle_p$ zone axis, only if the zone axis is not normal to the tilt axis, and not in $\langle 100\rangle_p$ or $\langle 111\rangle_p$, Figure 2.8. From the 12 zone axes of type $\langle 110\rangle_p$ the number of them exhibiting $\frac{1}{2}\{ooo\}_p$ reflections is used as an indication of the possible tilt systems and space groups although the preferred orientation of domains, especially if the perovskite has a particularly strained unit cell, can affect this, Table 2.2 [Woodward, 2004].

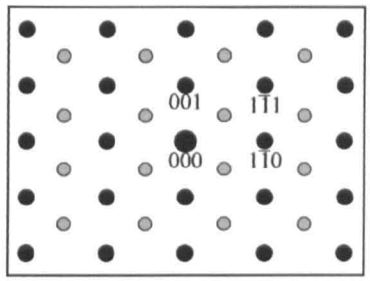

Figure 2.8. Superstructure reflections arising from anti-phase tilting (grey spots) at $\frac{1}{2}\{ooo\}_p$ positions in a $<110>_p$ zone axis diffraction pattern [Woodward, 2004].

In-phase tilting of octahedra causes the appearance of spots of type $\frac{1}{2}\{ooe\}_p$, where '*o*' refers to an odd number, in $<100>_p$ and $<111>_p$ zone axis but not $<110>_p$, Figures 2.9 and 2.10 [Woodward, 2004].

With the introduction of other cell multiplication mechanisms in addition to tilting, identification of the tilt system and space group becomes more complicated as more than one type of distortion can result in one type of superstructure reflection [Mitchell, 2002].

Antiparallel shifts of the A-site cations result in the appearance of superstructure reflections which depend on the vectors of their displacements, their arrangements and the symmetry changes that are generated the type of reflections and the zone axes in which they appear [Woodward, 2004]. For example, the antiparallel arrangement of Pb^{2+} ions in the $PbZrO_3$ structure, discussed in the ionic displacement section, causes the presence of $\pm\frac{1}{4}(hk0)_p$ $h \neq k$ reflections in a single direction in the $[001]_p$ zone axis diffraction patterns. The structure of $PbZrO_3$ is discussed further in section 2.6.2.

Table 2.2. The relationship of the number of $<110>_p$ zone axes exhibiting $½\{ooo\}_p$ reflections with the tilt system [Woodward *et al.*, 2006].

Tilt System	No. of $<110>_p$ zone axes exhibiting $½\{ooo\}_p$ reflections
$a^0a^0a^0$	0
$a^0a^0c^-$	8
$a^0b^-b^-$	10
$a^-a^-a^-$	6
$a^0b^-c^-$	12
$a^-b^-b^-$	10
$a^-b^-c^-$	12

Reaney et al. illustrated that the onset of in-phase tilting in some perovskites is associated with the anti-parallel cation displacements that cause cell doubling in a $<100>_p$ direction which results in the presence of reflections of type $½\{h00\}_p$ in some $<100>_p$ and $<110>_p$ zone axis diffraction patterns [Reaney *et al.*, 1994].

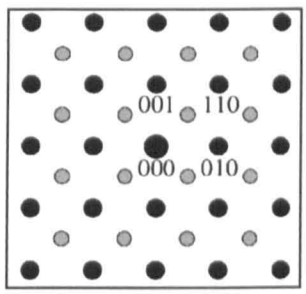

Figure 2.9. Superstructure reflections arising from in-phase tilting (grey spots) at $½\{ooe\}_p$ positions in a $<100>_p$ zone axis diffraction pattern [Woodward, 2004].

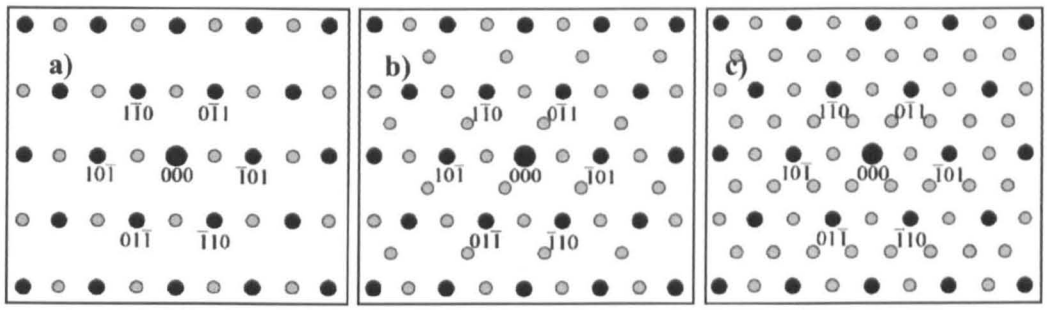

Figure 2.10. In-phase tilting corresponding to a) tilt system $a^0a^0c^+$, b) and c) more complex in-phase tilt systems resulting in $<111>_p$ zone axes diffraction patterns with superstructure reflections (grey) [Reaney *et al.*, 1994, Woodward *et al.*, 2006].

2.3. (Anti)Ferromagnetism

2.3.1. Magnetism

Magnetism comes from the word "magnetite", Fe_3O_4, which is the first known magnetic material, but modern research on magnetic materials started with the invention of electromagnets (1825) following the great discovery of Oersted that an electric current produces a magnetic field. We can think of any magnet as being made up of a number of dipoles where the total moment of the magnet is the sum of the moments of its constituent dipoles.

In inorganic solids, magnetism often results from inclusion of ions with unpaired *d* and *f* orbital electrons. Depending on the relative position and interaction of the magnetic ions, different types of magnetism can be revealed. The magnetic moment of an unpaired electron is quantified based on the electron spin and electron orbital motion, quantum mechanical parameters. Equation 2.3 shows the relationship between the spin quantum number, *S*, and the magnetic spin moment, μ_s,

$$\mu_s = g\sqrt{S(S+1)} \tag{2.3}$$

where *S* is half the sum of unpaired electrons for an ion and *g* (~2.0) is the gyromagnetic ratio [Ferrarelli, 2008].

For inorganic solids, the effect of electron orbital motion, observed in free atoms and ions is restricted and often an adjustment of *g* is required.

2.3.2. Different Types of Magnetism

Materials can be categorized based on their behaviour in a magnetic field and how the magnetic flux (ϕ) changes when the material is in the field (observed state) with when it is not (current state) so that the material adds to or substracts from the lines of magnetic flux due to the field, H. The relative quantity of $\phi_{observed}$ and $\phi_{current}$ are used to classify all the materials into 5 categories; diamagnetic ($\phi_{observed} < \phi_{current}$), paramagnetic or antiferromagnetic ($\phi_{observed} > \phi_{current}$) and ferrimagnetic or ferromagnetic ($\phi_{observed} >> \phi_{current}$) [Cullity and Graham, 2009].

The magnetization, M, is zero for empty space, very small and negative for diamagnetics, very small and positive for paramagnetics and antiferromagnetics and large and positive for ferromagnetic and ferrimagnetics.

Generally magnetic scientists take H as the fundamental magnetic field which produces magnetization M in magnetic materials. Changes in flux density or induction, B, generates voltage through Faraday's law and magnetic properties of materials are characterized by the magnitude and sign of M and the way it varies with H and susceptibility χ.

Typical curves of M vs. H are linear for dia-, para- and anti-ferromagnetics under normal circumstances and show no magnetism in the absence of the field, Figure 2.11a and b. The magnetization curve for ferro- and ferrimagnetics is nonlinear and χ changes with H and reaches a maximum value defining saturation and hysteresis, Figure 2.11c. As H goes toward higher values, magnetization becomes constant as it reaches the saturation value, M_s. Beyond saturation, M does not reduce to zero by removing the field. This phenomenon is

called hysteresis, a Greek word meaning "to lag behind" as the effect, M, lags behind the cause, H [Cullity and Graham, 2009].

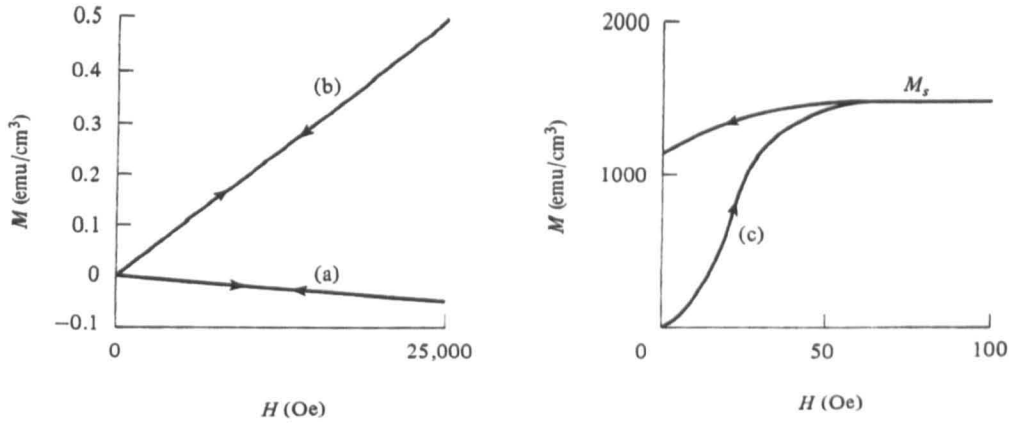

Figure 2.11. Magnetization curves of a) diamagnetics, b) paramagnetics/antiferromagnetics and c) ferromagnetic/ferrimagnetics [Cullity and Graham, 2009].

The curve of induction B, vs. field, is also called a magnetization curve and the ratio of B to H is called permeability μ, Figure 2.12. This curve can be found more useful than the M/H curve.

Permeability varies with the applied field and is strongly sensitive to purity, heat treatment, deformation and other structural factors. Magnetic behaviour of all substances can be categorized based on their values of χ and μ:

- $\chi = 0$ and $\mu = 1$, Empty space
- χ : small and negative and μ : slightly less than 1, diamagnetic.
- χ : small and positive and μ : slightly greater than 1, para- and antiferromagnetic.
- χ and μ : large and positive and functions of H, ferro- and ferromagnetic.

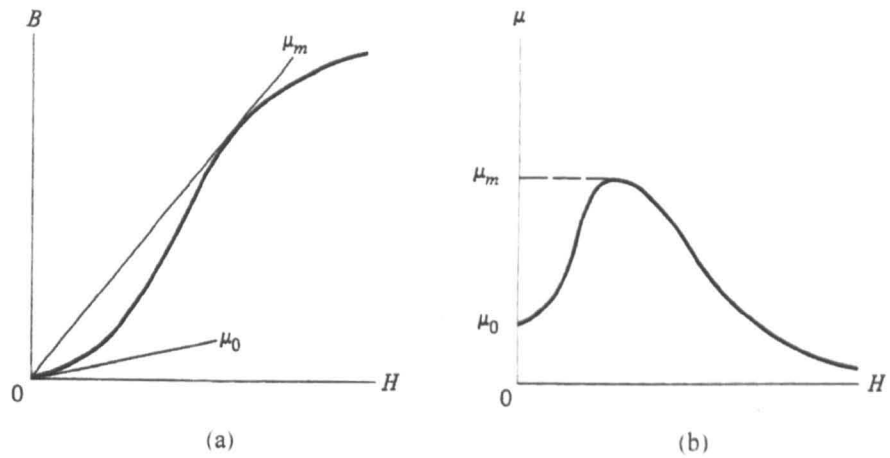

Figure 2.12. Ferromagnetic/ferrimagnetic curves of a) B vs. H and b) μ vs. H [Cullity and Graham, 2009].

Although magnetization stays constant after saturation, induction increases with increasing applied field and the slope of the curve is one beyond the saturation induction, B_s. The B vs. H curve from the demagnetized state to the saturation is the normal magnetization or normal induction curve, Figure 2.13. If H is reduced to zero after saturation has been reached in the positive direction, the induction in a ring specimen will decrease from B_s to B_r, the residual induction. If the applied field then reversed the induction will decrease to zero when the negative applied field reaches H_c, coercivity. This is the reverse field needed to "coerce" the material back to zero induction [Cullity and Graham, 2009].

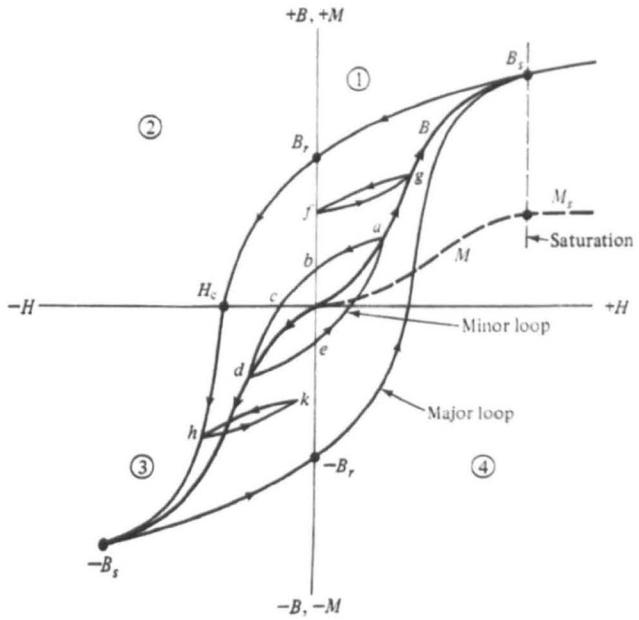

Figure 2.13. Magnetization curves and hysteresis loops. Height of M relative to B is exaggerated [Cullity and Graham, 2009].

2.3.3. Antiferromagnetism

The theory of antiferromagnetism was developed mainly by Neel [Neel, 1932]. Antiferromagnetic substances have a small positive susceptibility at all temperatures, but their susceptibility changes with temperature in an unusual way. In these materials as the temperature decreases, susceptibility increases and would go through a maximum at a critical temperature called the Neel temperature (T_N) above which the substance is paramagnetic and below which antiferromagnetic, Figure 2.14 [Cullity and Graham, 2009]. Most but not all antiferromagnetics, which are more common than ferromagnetics, are ionic compounds like oxides and sulphides.

The clue to understanding the behaviour of an antiferromagnet is in the way its susceptibility varies with temperature above T_N as the material obeys a Curie-Weiss law but with a negative value of θ. A plot of $1/\chi$ -vs. T is a straight line above T_N and this line extrapolates to a negative temperature at $1/\chi = 0$, Figure 2.14.

On a very localised scale, any tendency of a particular ionic moment to point in one direction is immediately counteracted by a tendency for the moment on an adjacent ion to point in the opposite direction and the exchange force is negative. As the randomising effect of thermal energy is low below T_N, the tendency toward an antiparallel alignment of moments is strong enough to act even in the absence of an applied field. The lattice of magnetic ions then breaks up into two sublattices A and B with opposite moments, Figure 2.15.

Below T_N the antiparallel arrangement is stronger and at 0K is perfect. At 0K an antiferromagnetic consists of two sublattices of magnetic ions with spontaneous magnetization in opposite directions in zero applied field causing the net spontaneous moment to be zero. In strong field however, the magnetisation is present. In contrast, a ferromagnetic material has a single lattice spontaneously magnetized with non-zero net moment irrespective of the applied field [Cullity and Graham, 2009].

Neel temperature for antiferromagnetics plays the same role as Curie temperature for ferromagnetics, dividing the temperature scale into a magnetically ordered region below it and a disordered (paramagnetic) region above it. The analogies to ferromagnetism makes the term "antiferromagnetism" clearly appropriate.

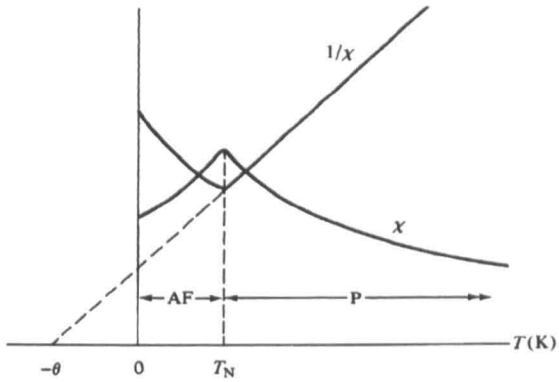

Figure 2.14. Schematic temperature dependence of susceptibility and inverse susceptibility for an antiferromagnetic material where AF stands for antiferromagnetic and P for paramagnetic [Cullity and Graham, 2009].

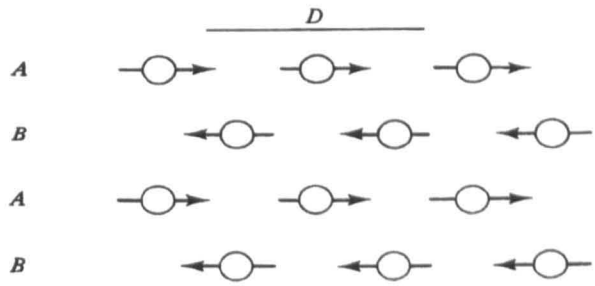

Figure 2.15. Antiferromagnetic arrangement of A and B sublattices [Cullity and Graham, 2009].

Antiferromagnetism in perovskites is often observed if the compound contains elements with unpaired $3d$ and $4f$ electrons. In these materials exchange coupling causes atoms to adopt anti-parallel spins such that the macroscopic magnetic moment is zero. Antiferromagnetic ordering is observed below T_N and can be recognized by appearance of 'magnetic bragg' peaks in neutron diffraction patterns [Mitchell, 2002].

2.4. Ferroelectricity

Many materials with perovskite structure exhibit ferroelectricity which is defined as the appearance of a spontaneous polarisation reversible by an applied electric field. Ferroelectricity is a subgroup of a wider group of materials known as pyroelectrics, which are a subgroup of a group called piezoelectric [Jona and Shirane, 1962].

2.4.1. Dielectric Materials

An electrical insulator that develops an electric polarisation when subjected to an applied electric field is a dielectric and developing a polarization in response to the applied field in an insulator is called 'dielectric behaviour'. An ideal dielectric has a polarisation independent of temperature with linear dependence on the applied electric field which with the removal of the field returns to zero. Paraelectric materials also develop electric polarisation with linear dependence on the applied electric field, but the polarisation is temperature-dependent.

2.4.2. Pyroelectricity

Pyroelectric crystals have a macroscopic polarisation, called the 'spontaneous polarisation' (P_S) which is the result of a net distance between the centres of the positive and negative charges in a unit cell. In a pyroelectric crystal, this displacement occurs along a unique polar axis. Spontaneous polarisation is normally temperature dependent and a change in charge flow can be detected when uniformly heating the material. This is called the 'pyroelectric effect' [Jaffe et al., 1971].

2.4.3. Piezoelectricity

The development of an electric dipole with application of stress is called direct piezoelectricity whereas the development of strain with application of an electric field is converse piezoelectricity. All materials develop a strain when placed in an electric field, a phenomenon known as electrostriction, but this differs from the converse piezoelectric effect, as reversal of the field causes no change in the strain and hence electric field and strain are not directly proportional [Jaffe *et al.*, 1971].

All crystals are assigned a 'point group' defining their crystal symmetry and there are 32 point groups. For a crystal to be piezoelectric, the point group must be non-centrosymmetric. A centrosymmetric crystal will show no polar properties since a centre of symmetry results in compensations for any charge displacements within the lattice. There are 21 point groups that lack a centre of symmetry, one of which is symmetrically constrained in a way that it cannot be piezoelectric, cubic 432 [Nye, 1985]. All the other 20 groups are all piezoelectric of which 10 are characterised by having a permanent electrical dipole moment, or a spontaneous polarisation, in the absence of a stress and therefore pyroelectric as well as piezoelectric [Moulson and Herbert, 1990, Sterianou, 2008].

2.4.4. Ferroelectricity

A crystal is ferroelectric if it exhibits a spontaneous polarisation reversible by an applied electric field. This polarisation consists of unit cell dipole moments aligned in one direction with neighbouring columns of unit cells aligned in a parallel manner. Towards the end of the 19^{th} century Rochelle salt, a medicinal crystal first prepared in the 17^{th} century, was found to

exhibit piezoelectricity [Curie and Curie, 1880]. In 1921 Valasek revealed that the electric polarisation measured along the x-axis of the crystal was not linearly dependent on the applied electric field and the exact value of the polarisation was not uniquely defined by the applied field, but dependent also on its immediate history [Valasek, 1921].

The resultant graph of polarisation P, vs. applied electric field E, for Rochelle salt showed a loop defining the range of polarisation at a given field strength. This is referred to as a 'dielectric hysteresis' loop where the term 'hysteresis' is used to describe the phenomenon of a fixed variable resulting in a range of permitted values for a dependent variable [Moulson and Herbert, 1990]. Rochelle salt was thus shown to be neither dielectric nor paraelectric in behaviour.

As in ferromagnets an applied magnetic field causes the formation of magnetic polarisation with a similar hysteresis effect, Valasek who had noted these similarities used the term 'ferroelectricity' to describe the phenomenon he observed in Rochelle salt [Valasek, 1921].

Figure 2.16 illustrates the polarisation vs. electric field behaviour of a ferroelectric single crystal where the field is applied parallel with the direction of spontaneous polarisation. As the field strength increases, the polarisation response becomes constant as it approaches its saturation value P_{SAT}. When the field is removed the polarisation does not return to zero but instead returns to a slightly lower value called the remnant polarisation P_r. If a reverse field is applied, the polarisation decreases first to zero and then to the negative saturation value $-P_{SAT}$. The value of the field when polarization is zero is called the 'coercive field' E_c, which is the field required to depolarise the crystal.

On cooling a polycrystalline ferroelectric ceramic from high temperature through its ferroelectric T_C each crystallite, or grain, will spontaneously polarise in a different direction.

The imposed stress to the ceramic creates a strain which is minimised by creating domains of different polarisation direction within the individual grain [Moulson and Herbert, 1990].

With a large enough electric field the polarisation of domains switches to other crystallographically identical orientations provided they have a larger component parallel with the applied field.

The random orientation of domains in a ceramic makes it easier for some domains to align or switch. Because of the resistance to domain switching, the polarisation in a ceramic is not fully reversible with field. This remnant polarization tends to be around half the value for the single crystal. For a ferroelectric ceramic the polarisation does not change as sharply around E_C, due to the orientation-dependent switching of domains which makes the dielectric hysteresis loop different from that of the single crystal, Figure 2.17.

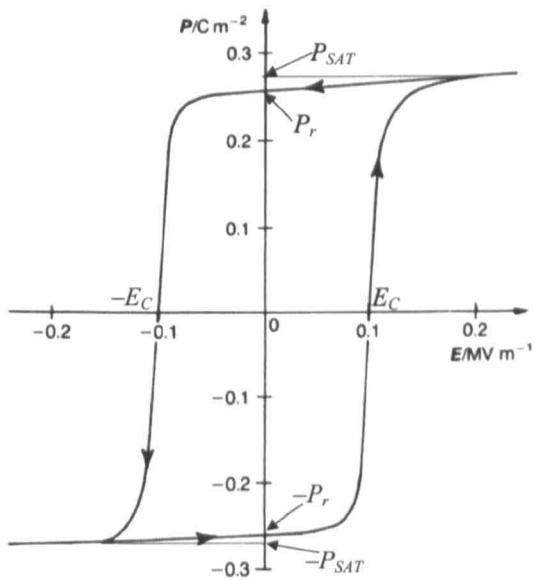

Figure 2.16. Dielectric loop of a ferroelectric single crystal [Moulson and Herbert, 1990].

When domains are aligned and there is a net polarisation the ceramic is 'poled'. A poled state is an essential state if the ceramic is to be used for its ferroelectric or piezoelectric properties, Figure 2.18 [Moulson and Herbert, 1990].

On cooling a ferroelectric through T_C two types of domains are generally observed: inversion and orientational often referred to as 180° and 90° domains, respectively [Wonratschek and Jeitschko, 1976, Putnis, 1992]. Domain walls separate the domains and it is the motion of the domain walls under applied field which is key to understanding macroscopic ferroelectric and piezoelectric properties.

For ferroelectrics, permittivity ε_r, vs. temperature T, behaviour has a sharp maximum at T_C. Above T_C, permittivity follows the Curie-Weiss law, Equation 2.4:

$$\varepsilon_r = \frac{C}{T - T_O} \tag{2.4}$$

where C is a material constant and T_O is a temperature close to T_C.

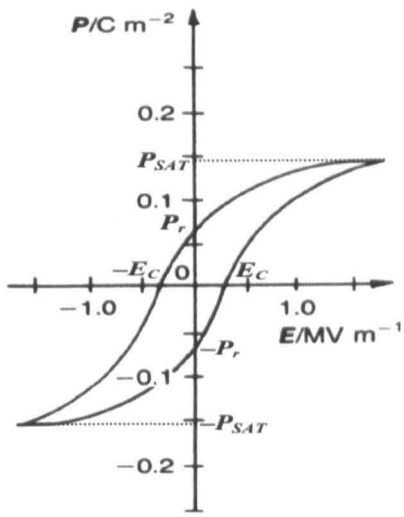

Figure 2.17. Dielectric hysteresis loop of $BaTiO_3$ ceramic [Moulson and Herbert, 1990].

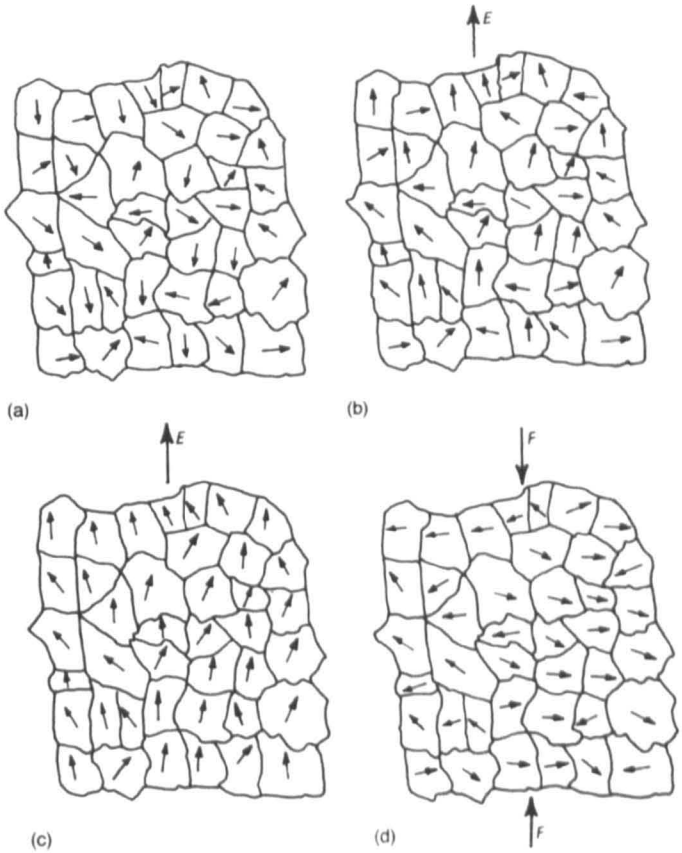

Figure 2.18. Two-dimensional illustration of poling a ceramic. a) Randomly oriented crystallites, b) Application of an electric field, *E*, causing 180° switching of some domain orientations, c) Application of a larger electric field, causing 180° and 90° switching of domain orientations and a change in macroscopic dimensions, d) 90° switching of domain orientations and destruction of macroscopic polarisation by applied stress *F* [Moulson and Herbert, 1990].

2.4.5. Antiferroelectricity

In some materials including perovskites the ions are displaced from the cubic positions in a way that neighbouring ions have displacement vectors with opposite directions, i.e. antiparallel displacement. If the magnitude of the displacement vectors are equal making a final zero net polarization the material is called 'antiferroelectric', analogous to the term antiferromagnetic in magnetic materials [Woodward, 2004].

An antiferroelectric crystal is defined as a crystal whose structure can be considered as being composed of two sublattices polarized spontaneously in antiparallel direction and whose ferroelectric phase can be induced by applying an electric field. When a low frequency AC field with suitable strength is applied, the reversal of spontaneous polarization in ferroelectrics result in a single hysteresis loop but in some antiferroelectrics (e.g. $PbZrO_3$ and $NaNbO_3$) results in a double hysteresis loop, Figure 2.19. This behaviour is not exclusive to antiferroelectrics and not all antiferroelectrics exhibit this double hysteresis loops. This behaviour also occurs when the structure exhibits ferroelectric-like behaviour as a result of the applied field. This is referred to as a field-induced phase transition [Moulson and Herbert, 1990, Woodward, 2004].

With the application of an external electric field, displacements in an antiferroelectric material can be switched to a parallel configuration but will revert to the antiparallel configuration on removal of the field. Figure 2.20 shows a summary of P vs. E behaviour for ferroelectric, antiferroelectric and paraelectric materials.

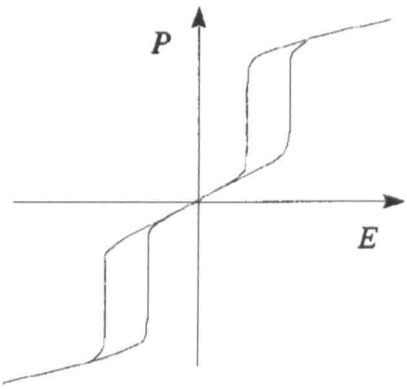

Figure 2.19. Dielectric behaviour of an antiferroelectric material, exhibiting field-induced ferroelectricity [Hatt and Cao, 2000].

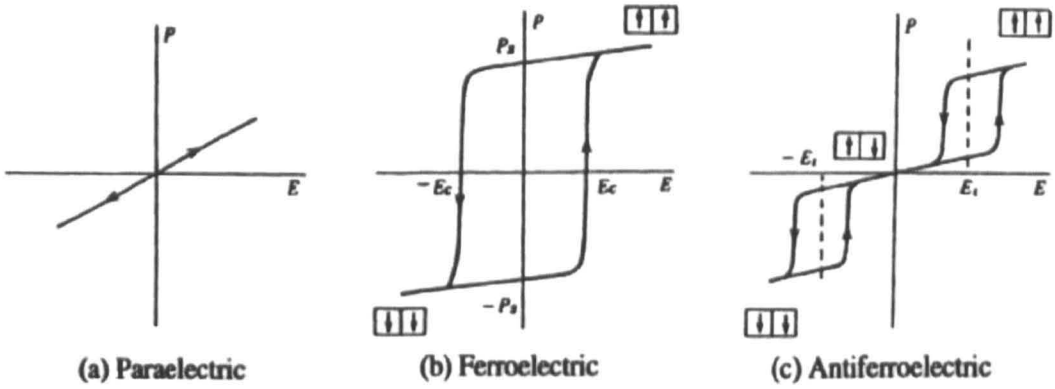

Figure 2.20. Typical hysteresis loops in paralectric, ferroelectric and antiferroelectric materials [Uchino, 1997].

2.5. Bismuth Ferrite, $BiFeO_3$

2.5.1. Structure of $BiFeO_3$

$BiFeO_3$ was first synthesised in 1957 [Royen and Swars, 1957] and since then has been the subject of many investigations to reveal its structure and properties. $BiFeO_3$ is reported to have a rhombohedrally distorted perovskite structure, *R3c*, where Bi^{3+} ions are in the cubo-octahedral positions and Fe^{3+} ions are in the octahedral positions. It has parallel off-centre displacement of both Fe^{3+} and Bi^{3+} sublattices along the $[111]_p$ direction and an $a^-a^-a^-$ tilt system in which the FeO_6 octahedra rotate in anti-phase about $[111]_p$ direction. The resulting unit cell contains two formula units, Figure 2.21. The Bi^{3+} ions have a larger displacement, in comparison to the Fe^{3+} ions, along the $[111]_p$ direction due to the active lone pair electrons in Bi^{3+} ions and this results in the oxygen being effectively fourfold coordinated to two Bi^{3+} ions and two Fe^{3+} ions [Kiselev *et al.*, 1962, Roginska.Ye *et al.*, 1966, Michel *et al.*, 1969b, Moreau *et al.*, 1971, Kubel and Schmid, 1990].

Figure 2.21a shows the relationship of the rhombohedral cell produced by $a^-a^-a^-$ tilting to the cubic cell. Although it is a rhombohedral perovskite, $a_r \approx \sqrt{2}\, a_c$; $\alpha \approx 60^o$; $V_r \approx 2a_c^3$, with lattice parameters of a_r = 5.637 Å and α = 59.344° , $BiFeO_3$ is often described in a hexagonal unit cell, $a_h \approx \sqrt{2}\, a_c$; $c_h \approx 2\sqrt{3}\, a_c$; $V_h \approx 6a_c^3$, with the lattice parameters of a_h = 5.5775(5) Å and c_h = 13.8616(8) Å, Figure 2.21b [Sosnowska *et al.*, 1996, Mitchell, 2002].

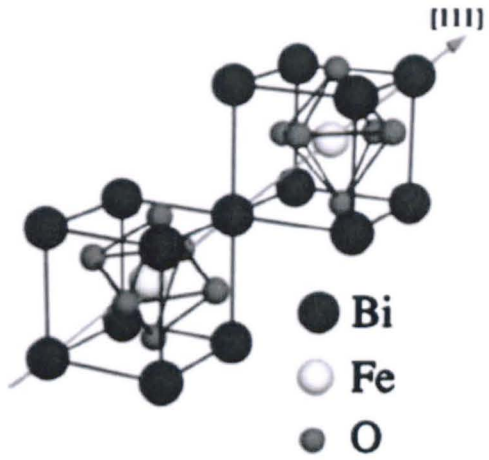

Figure 2.20. Rhombohedrally distorted perovskite structure of $BiFeO_3$ which shows the anti-phase rotation of FeO_6 octahedra along the $[111]_p$ direction and the displacement of cations relative to oxygen anions [Neaton *et al.*, 2005].

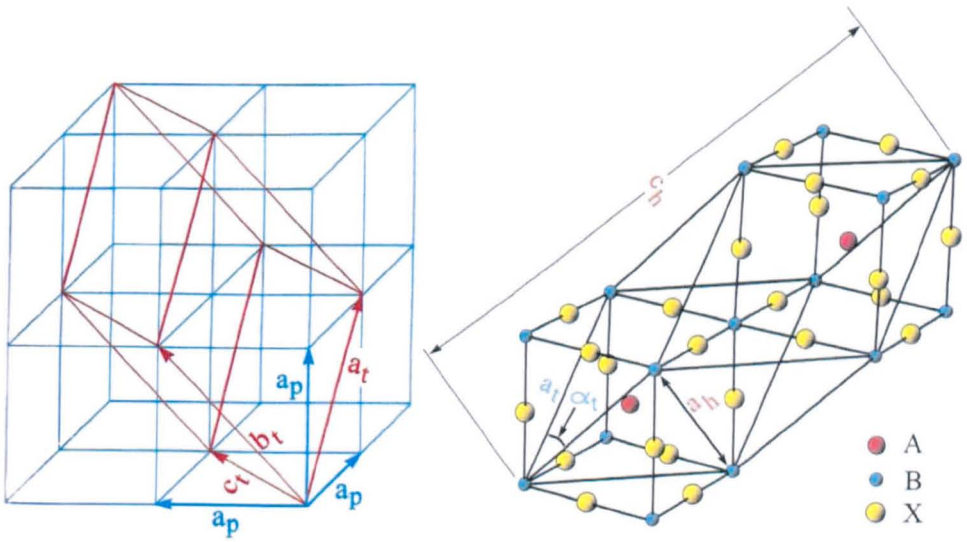

Figure 2.21. Relationship of the rhombohedral cell produced by $a^-a^-a^-$ to cubic cell in a) rhombohedral unit cell and b) hexagonal unit cell [Mitchell, 2002].

2.5.2. Properties of $BiFeO_3$

Ferroelectricity

$BiFeO_3$ exhibits ferroelectric behaviour below the curie temperature of $T_c \sim 830$ °C but the hysteresis loops of polarisation vs. applied electric field are not saturated, even at very low temperatures. However theoretical calculations suggest that the spontaneous polarisation is large due to the large displacements of the cations [Fedulov, 1961, Teague *et al.*, 1970, Kumar *et al.*, 1998, Neaton et al., 2005]. Teague et al. measured a spontaneous polarisation of 6.1 $\mu C\ cm^{-2}$ at 77 K along the $<111>_p$ direction and concluded that for a distorted ferroelectric perovskite with such a high T_C this measured polarization was unexpectedly low, around a tenth of what they expected from the atomic coordinates [Teague et al., 1970]. However, recent studies on $BiFeO_3$ thin films have revealed that the spontaneous polarisation found in thin films is closer to the theoretical value and almost an order of magnitude larger than values measured for bulk ceramics [Wang *et al.*, 2003, Yun *et al.*, 2004].

The T_C was first measured via linear expansion and permittivity measurements to be in the interval 840 – 850 °C [Krainik *et al.*, 1966] but recently differential scanning calorimetry, DSC, showed a more precise value of the phase transition at $T_C = 836$ °C [Kumar *et al.*, 2000a].

On heating $BiFeO_3$ to temperatures above T_C, the ferroelectric rhombohedral phase undergoes a transition to a paraelectric orthorhombic phase with a $GdFeO_3$-type structure exhibiting *Pbnm* space group with $a^+b^-b^-$ octahedral tilt system. This high temperature phase

has a unit cell of $\sqrt{2}a_c$ x $\sqrt{2}a_c$ x $2a_c$ where $a_c \approx 4$ Å [Marezio *et al.*, 1970a, Glazer, 1972, Arnold *et al.*, 2009, Levin *et al.*, 2010].

Antiferromagnetism

Magnetic susceptibility measurement in 1963 showed that $BiFeO_3$ is antiferromagnetic below the Neel temperature of $T_N \sim 370$ °C [Smolenskii *et al.*, 1963, Fischer *et al.*, 1980] and neutron diffraction [Kiselev *et al.*, 1963] revealed a G-type anti-ferromagnetic spin configuration where Fe^{3+} ions have six nearest neighbours with anti-parallel spins. However in 1982 using high resolution neutron diffraction Sosnowska et al. showed that the spin structure of $BiFeO_3$ is not satisfactorily described by G-type ordering and instead they suggested that the magnetic ordering follows a cycloidal spiral in the $[110]_h$ direction with a period of $\lambda = 620$ Å and the $(110)_h$ spin rotation plane which is unusual for perovskites. According to Sasnowka et al. $BiFeO_3$ exhibits week ferromagnetism at room temperature as a result of residual magnetic moments caused by canted spin magnetic structure [Sosnowska *et al.*, 1982].

Magnetoelectricity

The existence of both ferroelectric and antiferromagnetic ordering makes $BiFeO_3$ a magnetoelectric material. However, it is a matter of great debate whether there is any direct coupling of electric and magnetic subsystems. The *R3c* space group allows a linear magneto-electric effect but this effect has not been observed in $BiFeO_3$, purportedly due to the space

modulated spin structure [Fischer *et al.*, 1980, Kubel and Schmid, 1990, Sosnowska *et al.*, 1996].

Despite very limited evidence of direct coupling, the dependence of spontaneous magnetization and spontaneous polarization on the electric and magnetic fields, respectively, has created much interest for its use in applications in the field of information storage, sensors and electric field controlled ferromagnetic resonance devices and transducers with magnetically modulated piezoelectricity [Kanai *et al.*, 2001, Fiebig *et al.*, 2002, Hill, 2000, Wang *et al.*, 2003].

2.5.3. Difficulties with $BiFeO_3$

To realize the potential magneto-electric effect, the $BiFeO_3$ samples should have the following properties:

- Exhibit low-leakage ferroelectric behaviour with reasonably large piezoelectric properties or, in general long-range ferroelectric order as the low resistivity makes it difficult to draw out the intrinsic ferroelectricity.

The high leakage current mainly results from the valence fluctuations of Fe ions, volatilization of Bi ions, and the existence of secondary phases which can all be suppressed by optimizing the fabrication process or/and making solid solutions based on bismuth ferrite [Kumar et al., 2000a, Palkar *et al.*, 2002, Fiebig, 2005, Uchida *et al.*, 2005, Das *et al.*, 2006, Jun *et al.*, 2007].

- Display large remnant magnetization (or at least nonzero) or long-range ferromagnetic order or long-range canted anti-ferromagnetic order. The inhomogeneous spin structure cancels the macroscopic magnetization and prohibits observing the linear magnetoelectric effects.

The spatially modulated, cycloidal spin structure can be suppressed by strain, high magnetic field, temperature, and making bismuth ferrite-based solid solutions. Also according to Shan-Tao Zhang et al. the spin cycloids are correlated to the *R3c* space group of $BiFeO_3$ and as a result a structural phase transition might destroy the inhomogeneous spin structure [Sosnowska *et al.*, 1982, Sosnowska *et al.*, 1994, Sosnowska *et al.*, 2002, Pradhan *et al.*, 2005, Bai *et al.*, 2005].

If these problems remain unsolved then it is unlikely that $BiFeO_3$ will be used in many applications.

Preparation of phase pure bismuth ferrite is reported to be difficult mainly due to the narrow temperature range of phase stabilization. Filip'ev et al. reported that the samples fired at temperatures above 750 °C contained Fe_2O_3, which was residual in the sample after Bi_2O_3 volatilised [Filip'ev *et al.*, 1960]. Bucci et al. claimed that decomposition begins slowly at 810 °C and increases with temperature [Bucci *et al.*, 1972]. At 870 °C, they reported that their samples had completely decomposed while a phase diagram of the Bi_2O_3 – Fe_2O_3 binary system made in 1965 had shown that $BiFeO_3$ is stable up to 930 °C [Speranskaya *et al.*, 1965]. These conflicting reports demonstrate the complexity of processing $BiFeO_3$ whose instability is likely due to secondary phases which compete with the perovskite phase, such

as $Bi_2Fe_4O_9$, $Bi_{12}(Bi_{0.5}Fe_{0.5})O_{19.5}$ and $Bi_{25}FeO_{40}$ [Sosnowska *et al.*, 1982, Kumar *et al.*, 2000a]. The most common techniques suggested to avoid secondary phases are:

- Making solid solutions with other oxide perovskites [Smith *et al.*, 1968, Kumar *et al.*, 2000b, Comyn *et al.*, 2004, Stevenson *et al.*, 2007].
- Leaching secondary phases with nitric acid [Filip'ev *et al.*, 1960, Achenbach *et al.*, 1967].
- Rapid liquid phase sintering [Wang *et al.*, 2004, Yuan *et al.*, 2006b].
- Doping with rare earth elements [Zalesskii *et al.*, 2003, Lee *et al.*, 2006, Yuan and Or, 2006b, Yuan *et al.*, 2006a, Yuan and Or, 2006a, Yuan *et al.*, 2007, Nalwa and Garg, 2008, Nalwa *et al.*, 2008b, Cheng *et al.*, 2008b].

2.5.4. Doping of $BiFeO_3$

Doping of $BiFeO_3$ often gives a beneficial effect on properties, such as an increase in dielectric constant, the decrease in the leakage current and the destruction of the space modulated spin structure. Rare earth cations are considered the most suitable substitutes for Bi^{3+} ions as they can easily be accommodated in the structure. Partial substitution of Bi^{3+} ions by lanthanides has been shown to improve ferroelectric properties and magnetization. A-site substitution results in a uniform canted anti-ferromagnetic ordering and reportedly increases magneto-electric interaction [Zalesskii *et al.*, 2003, Lee *et al.*, 2006, Yuan and Or, 2006b].

Rare earths and rare earth orthoferrite perovskites

Rare earth oxides, RE_2O_3, are thermodynamically very stable [Aspinall, 2001]. The $RE^{3+}\_O^{2-}$ bond is stronger than $Bi^{3+}\_O^{2-}$ which enhances the stability of the perovskite phase minimizing the bismuth volatilization and reducing the number of oxygen vacancies [Palkar *et al.*, 2003].

The perovskite structured RE orthoferrites, from $LaFeO_3$ to $LuFeO_3$, adopt the $GdFeO_3$-type structure with *Pbnm* space group. Throughout the Lanthanide series from La to Lu with increasing the atomic number the *a* and *c* parameters increase while the *b* parameter passes through a maximum for Gd [Mitchell, 2002]. Many research groups have investigated substituting RE ions for Bi in $BiFeO_3$ with many conflicting reports, e.g.

- La^{3+}:

Several research groups have reported that La substitution at Bi-site in $BiFeO_3$ eliminates the impurity phases and enhances the magnetoelectric coupling [Mathe *et al.*, 2002, Zalesskii *et al.*, 2003, Zhang *et al.*, 2006a, Zhang *et al.*, 2006b, Das *et al.*, 2006, Jiang *et al.*, 2006, Das *et al.*, 2007, Yuan *et al.*, 2007, Ravinski *et al.*, 2007, Yoneda *et al.*, 2007, Lin *et al.*, 2007, Cheng *et al.*, 2008a, Chena *et al.*, 2008]. There is general agreement that La enhances the magnetic properties by destroying the cycloidal spin structure as the compound transforms from a *R3c* to an orthorhombic structure. There are also reports that the leakage current reduces [Cheng *et al.*, 2008a], dielectric properties improve [Das *et al.*, 2006], piezoelectric coefficient can be measured [Yuan *et al.*, 2007] and electrical polarization loop can be obtained [Cheng *et al.*, 2008a].

- Nd^{3+}:

Doping $BiFeO_3$ with Nd reputedly destroys the space modulated spin structure at ~ 20% as a result of structural transformation accompanied by better magnetization and some evidence of a ferromagnetic response at room temperature. The leakage current is reduced resulting in better ferroelectric properties and reportedly stronger magnetoelectric coupling near the T_N. In addition, large piezoelectric coefficients have been reported [Mathe *et al.*, 2004, Huang *et al.*, 2006, Yuan and Or, 2006a, Yuan *et al.*, 2006a, Huang *et al.*, 2008, Pandit *et al.*, 2009].

- Sm^{3+}:

Doping $BiFeO_3$ with Sm on the Bi-site is reported to eliminate secondary phases and change the crystal structure. The latter results in destruction of the space modulated spin structure and improved magnetic properties. Yuan and Or obtained a large piezoelectric coefficient and high remnant polarization suggesting the existence of long-range ferroelectric order while Nalwa et al. suggested Sm doping improves the polarization at the same time as increasing the leakage current [Yuan and Or, 2006b, Nalwa *et al.*, 2008b, Nalwa and Garg, 2008].

- Gd^{3+}:

Reports on Gd-substituted bismuth ferrite have stated a decrease in the amount of impurity phases, decrease in T_N to about 150 °C, enhancements in magnetization with observation of ferroelectric and magnetic loops while the increased dielectric constant and decreased dielectric loss were strongly dependent on composition and frequency. There are no reports

on the structural phase transitions in these systems while some reports present evidence for both lattice constants *a* and *c* decreasing as the Gd^{3+} content increases [Fanggao *et al.*, 2006, Hu *et al.*, 2007, Uniyal and Yadav, 2008].

- Y^{3+}:

To prove that the changes in multiferroic properties on rare earth-substitution on Bi-site is originally a cation size effect, Mishra et al. doped $BiFeO_3$ with a non-rare earth ion Y with an ionic radius similar to that of reported rare earths. They revealed compositionally driven structural changes and reduction of secondary phases along with considerable changes in dielectric, ferroelectric and magnetic properties of $BiFeO_3$. They reported a remarkable increase in macroscopic magnetization which they indicated was field dependant even at room temperature [Mishra *et al.*, 2008].

2.6. PZT solid solution and analogy with RE-doped $BiFeO_3$

2.6.1. Lead titanate ($PbTiO_3$)

Lead titanate was first fabricated in 1937 through solid state reaction of PbO and TiO_2 across a range of temperatures [Cole and Espenshied, 1937]. However, at the time of discovery, it was not known to be a ferroelectric and it was not until extensive experiments by Shirane and co-workers in the 1950's that it became apparent that $PbTiO_3$ was a ferroelctric. These authors substituted Pb^{2+} for Ba^{2+} in barium titanate and observed that the ferroelectric properties were retained to higher temperatures as the amount of Pb^{2+} increased [Shirane *et al.*, 1950, Shirane and Suzuki, 1951].

$PbTiO_3$ has the same room temperature structure as barium titanate, tetragonal, but its degree of tetragonality is higher. It has a ferroelectric Curie temperature of $T_C \sim 490$ °C. The space group is *Pm-3m* above and *P4mm* below the T_C. The lattice parameters are $a = 3.894$ Å and $c = 4.140$ Å and tetragonality of $c/a = 1.06$ at room temperature [Shirane *et al.*, 1950].

$PbTiO_3$ in ceramic form is hard to pole and often disintegrates under high DC fields [Moulson and Herbert, 1990]. There are not many phases with energy of formation close to that of $PbTiO_3$ and phase pure preparation is therefore straightforward. It is also an ideal candidate to stabilise the perovskite phase in solid solutions with less stable end members [Eitel *et al.*, 2001].

2.6.2. Lead zirconate ($PbZrO_3$)

$PbZrO_3$ was first fabricated in 1950 by Roberts [Roberts, 1950] and was shown by Sawaguchi et al. to undergo a phase transition from cubic paraelectric to an anti-ferroelectric orthorhombic structure, at about 230°C. It has anti-parallel arrangement of Pb^{2+} ions which results in a cell whose dimensions are approximately $\sqrt{2}\ a_c$ x $2\sqrt{2}\ a_c$ x $2a_c$, a = 5.8820 Å ; b = 11.7830 Å ; c = 8.2280 Å, Figure 2.22. The space group symmetry is *Pbam* which arises from a combination of antiparallel displacements and an $a^-a^-a^0$ tilt system [Glazer *et al.*, 1993, Roberts, 1950, Sawaguchi *et al.*, 1951b, Roberts, 1951, Sawaguchi *et al.*, 1951a].

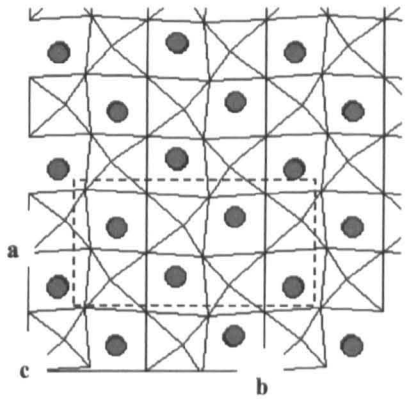

Figure 2.22. *c* axis view of $PbZrO_3$, illustrating the antiparallel displacements of the Pb^{2+} ions (grey circles) in the *a-b* plane, responsible for antiferroelectricity in the crystal. The dashed box show the boundary of the unit cell in this plane [Woodward, 2004].

2.6.3. PZT Solid Solution, $Pb(Zr_{1-x}Ti_x)O_3$

Shirane and Takeda [Shirane and Takeda, 1952] showed that by replacing up to 10 % of the Zr^{4+} in $PbZrO_3$ with Ti^{4+}, a ferroelectric structure was obtained. This initial discovery ultimately led to the formation of the PZT phase diagram, Figure 2.23.

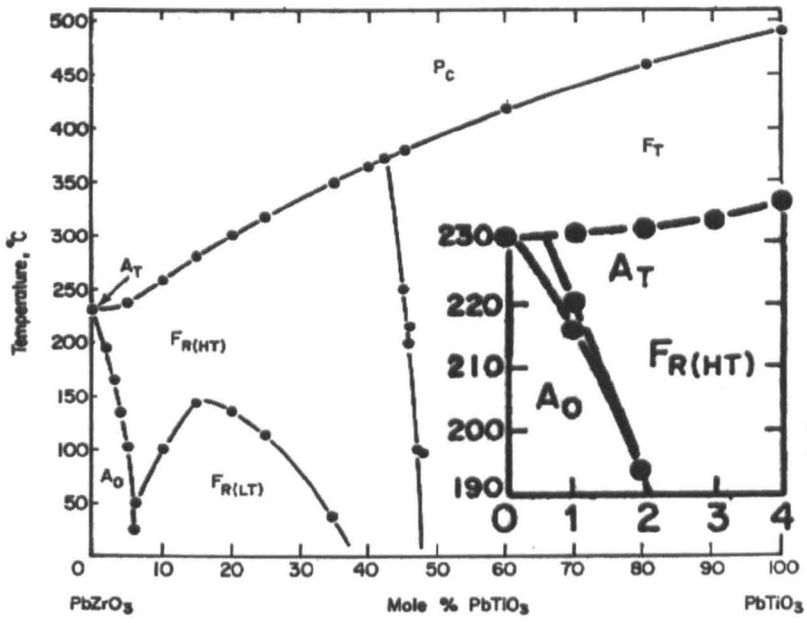

Figure 7.23. Phase diagram of the $Pb(Zr_{1-x}Ti_x)O_3$. The letters P, F and A refer to paraelectric, ferroelectric and antiferroelectric phases respectively. The subscripts C, T, R and O refer to cubic, tetragonal, rhombohedral and orthorhombic unit cells respectively [Jaffe *et al.*, 1971].

In addition to the antiferroelectric $PbZrO_3$ structure, there are two rhombohedral phases, of which one exists at high temperatures and is untilted with space group *R3m* and the other one at lower temperatures with an $a^-a^-a^-$ anti-phase tilt system and space group *R3c*. As Ti^{4+}

concentration increases, the tolerance factor t, increases and at ~ 48% Ti a tetragonal structure is stabilised, similar to that of $PbTiO_3$ [Michel *et al.*, 1969a, Jaffe *et al.*, 1971, Woodward, 2004]. The phase boundary between the rhombohedral and tetragonal phases is largely temperature independent and is referred to as the morphotropic phase boundary, MPB.

2.6.4. Concept of this Research, 'RE-doped $BiFeO_3$: an analogy with PZT'

To predict the behaviour of $BiFeO_3$ as a function of increasing RE concentration comparisons with other systems, such as PZT, are potentially useful. In PZT, when the larger, less polarisable Zr^{4+} substitutes for Ti^{4+} ions, two key crystallochemical factors are affected: i) the tolerance factor decreases; and ii) the average polarisability of the ions within the structure decreases. A direct consequence of the decrease in polarisability is a decrease in ferroelectric T_C. However, t simultaneously decreases resulting in an increase in the driving force for octahedral rotation. Initially, this results in a transition from *R3m* to *R3c* but ultimately an antiferroelectric, *Pbam* phase is stabilised for low Ti concentrations, < 6% [Michel *et al.*, 1969a, Jaffe *et al.*, 1971, Woodward, 2004].

Table 2.3 shows the t and space group symmetries of the end members for several $BiFeO_3$ – $REFeO_3$ solid solutions. From this data it is evident that in any given solid solution, as the RE concentration increases, there is a decrease in tolerance factor and average polarizability of the ions in the structure [Shannon and Prewitt, 1969, Shannon, 1993]. This situation is similar to that observed in PZT as a function of increasing Zr concentration and by analogy it

is postulated that an antiferroelectric structure may be stabilised within the (Bi,RE)FeO_3 family of materials.

More trivially, as the RE concentration further increases, the solid solution will favour the orthoferrite, ($a^-a^-c^+$, *Pnma*) rather than rhombohedral ($a^-a^-a^-$, *R3c*) structure [Marezio *et al.*, 1970b, Marezio *et al.*, 1970a, Karimi *et al.*, 2009a, Karimi *et al.*, 2009b].

The goal of the thesis is to establish a deep understanding of the structure property relations in RE doped $BiFeO_3$ and thereby determine whether the above hypotheses are correct.

Table 2.3. Tolerance factor and apace group symmetry of bismuth ferrite and rare earth orthoferrites [Shannon and Prewitt, 1969, Karimi *et al.*, 2009a].

Composition	$BiFeO_3$	$LaFeO_3$	$NdFeO_3$	$SmFeO_3$	$GdFeO_3$
Tolerance factor	0.96	0.95	0.93	0.92	0.91
Average A-site Polarisability	6.12	5.5	5.01	4.74	4.37
Symmetry	*R3c*	*Pnma*	*Pnma*	*Pnma*	*Pnma*

2.7. References

ACHENBACH, G. D., JAMES, W. J. & GERSON, R. (1967) *Preparation of Single-Phase Polycrystalline $BiFeO_3$.* Journal of the American Ceramic Society, **50,** 437.

ARNOLD, D. C., KNIGHT, K. S., MORRISON, F. D. & LIGHTFOOT, P. (2009) *Ferroelectric-Paraelectric Transition in $BiFeO_3$: Crystal Structure of the Orthorhombic beta Phase.* Physical Review Letters, **102,** 027602.

ASPINALL, H. C. (2001) *Chemistry of the f-block Elements,* Amsterdam, Gordon and Breach Science Publishers.

BAI, F. M., WANG, J. L., WUTTIG, M., LI, J. F., WANG, N. G., PYATAKOV, A. P., ZVEZDIN, A. K., CROSS, L. E. & VIEHLAND, D. (2005) *Destruction of Spin Cycloid in (111)(c)-Oriented $BiFeO_3$ Thin Films by Epitaxial Constraint: Enhanced Polarization and Release of Latent Magnetization.* Applied Physics Letters, **86,** 032511.

BUCCI, J. D., ROBERTSON, B. K. & JAMES, W. J. (1972) *The Precision Determination of the Lattice Parameters and the Coefficients of Thermal Expansion of $BiFeO_3$.* Journal of Applied Crystallography, **5,** 187.

CHENA, J. R., WANG, W. L., LIA, J. B. & RAO, G. H. (2008) *X-ray diffraction analysis and specific heat capacity of $(Bi_{1-x}La_x)FeO_3$ perovskites.* Journal of Alloys and Compounds, **459,** 66.

CHENG, Z. X., LI, A. H., WANG, X. L., DOU, S. X., OZAWA, K., KIMURA, H., ZHANG, S. J. & SHROUT, T. R. (2008a) *Structure, ferroelectric properties, and*

magnetic properties of the La-doped bismuth ferrite. Journal of Applied Physics, **103**, 07E507.

CHENG, Z. X., WANG, X. L., DOU, S. X., KIMURA, H. & OZAWA, K. (2008b) *Enhancement of Ferroelectricity and Ferromagnetism in Rare Earth Element Doped $BiFeO_3$*. Journal of Applied Physics, **104**, 116109.

COLE, S. S. & ESPENSHIED, H. (1937) *Lead Titanate: Crystal Structure, Temperature of Formation and Specific Gravity Data* Journal of Physical Chemistry, **41**, 445.

COMYN, T. P., MCBRIDE, S. P. & BELL, A. J. (2004) *Processing and electrical properties of $BiFeO_3$-$PbTiO_3$ ceramics*. Materials Letters, **58**, 3844.

CULLITY, B. D. & GRAHAM, C. D. (2009) *Introduction to Magnetic Materials*, Hoboken, NJ, USA, John Wiley & Sons, Inc.

CURIE, J. & CURIE, P. (1880) *Development by Pressure of Polar Electricity in Hemihedral Crystals with Inclined Faces*. Bulletin de la Societe Minerale de France, **3**, 90.

DAS, S. R., BHATTACHARYA, P., CHOUDHARY, R. N. P. & KATIYAR, R. S. (2006) *Effect of La substitution on structural and electrical properties of $BiFeO_3$ thin film*. Journal of Applied Physics, **99**, 066107.

DAS, S. R., CHOUDHARY, R. N. P., BHATTACHARYA, P., KATIYAR, R. S., DUTTA, P., MANIVANNAN, A. & SEEHRA, M. S. (2007) *Structural and multiferroic properties of La-modified $BiFeO_3$ ceramics*. Journal of Applied Physics, **101**, 034104.

EITEL, R. E. & RANDALL, C. A. (2007) *Octahedral Tilt-Suppression of Ferroelectric Domain Wall Dynamics and the Associated Piezoelectric Activity in $Pb(Zr,Ti)O_3$* Physical Review B, **B75**, 094106.

EITEL, R. E., RANDALL, C. A., SHROUT, T. R., REHRIG, P. W., HACKENBERGER, W. & PARK, S. E. (2001) *New High Temperature Morphotropic Phase Boundary Piezoelectrics Based on $Bi(Me)O_3$–$PbTiO_3$ Ceramics* Japanese Journal of Applied Physics, **40**, 5999.

FANGGAO, C., GUILIN, S., KUN, F., PING, Q. & QIJUN, Z. (2006) *Effect of Gadolinium Substitution on Dielectric Properties of Bismuth Ferrite.* Journal of Rare Earths, **24**, 273.

FEDULOV, S. A. (1961) *Determination of Curie temperature for ferroelectric $BiFeO_3$.* Dokl. Akad. Nauk. SSSR, **139**, 1345.

FEDULOV, S. A., LADYZHINSKII, P. B., PYATIGORSKAYA, I. L. & VENEVTSEV, Y. N. (1964) *Complete Phase Diagram of the $PbTiO_3$-$BiFeO_3$ System.* Soviet Physics-Solid State, **6**, 375.

FERRARELLI, M. C. (2008) Structure-Composition-Property Relations in The $ACu_3Ti_4O_{12}$ Structure-Type. *Engineering Materials.* Sheffield, The University of Sheffield.

FIEBIG, M. (2005) *Revival of the magnetoelectric effect.* Journal of Physics D-Applied Physics, **38**, R123.

FIEBIG, M., LOTTERMOSER, T., FROHLICH, D., GOLTSEV, A. V. & PISAREV, R. V. (2002) *Observation of Coupled Magnetic and Electric Domains.* Nature, **419**, 818.

FILIP'EV, V. S., SMOL'YANINOV, I. P., FESENKO, E. G. & BELYAEY, I. I. (1960) *Synthesis of $BiFeO_3$ and Determination of the Unit Cell.* Soviet Physics - Crystallography, **5,** 913.

FISCHER, P., POLOMSKA, M., SOSNOWSKA, I. & SZYMANSKI, M. (1980) *Temperature-Dependence of the Crystal and Magnetic-Structures of $BiFeO_3$.* Journal of Physics C-Solid State Physics, **13,** 1931.

GLAZER, A. M. (1972) *The Classification of Tilted Octahedra in Perovskites.* Acta Crystallographica, **B28,** 3384.

GLAZER, A. M. (1975) *Simple Ways of Determining Perovskite Structures.* Acta Crystallographica, **A31,** 756.

GLAZER, A. M., ROLEDER, K. & DEC, J. (1993) *Structure and Disorder in Single-Crystal Lead Zirconate, $PbZrO_3$* Acta Crystallographica, **B49,** 846.

GOLDSCHMIDT, V. M. (1926) *Geochemische Verteilungsgesetze Der Elemente.* **Skrifter utg. Av det Norske Viedenskaps-Akademi i Oslo,** 1.

HAERTLING, G. H. (1999) *Ferroelectric Ceramics: History and Technology.* Journal of American Ceramic Society, **82,** 797.

HATT, R. A. & CAO, W. (2000) *Landu-Ginzburg Model for Antiferroelectric Phase Transitions Based in Microscopic Symmetry.* Physical Review, **B58,** 565.

HILL, N. A. (2000) *Why Are There So Few Magnetic Ferroelectrics?* . Journal of Physical Chemistry C, **B24,** 6694.

HOWARD, C. J. & STOKES, H. T. (1998) *Group-theoretical analysis of octahedral tilting in perovskites.* Acta Crystallographica, **B54,** 782.

HU, G. D., CHENG, X., WU, W. B. & YANG, C. H. (2007) *Effects of Gd substitution on structure and ferroelectric properties of $BiFeO_3$ thin films prepared using metal organic decomposition.* Applied Physics Letters, **91,** 232909.

HUANG, F. Z., LU, X. M., LIN, W. W., WU, X. M., KAN, Y. & ZHU, J. S. (2006) *Effect of Nd dopant on magnetic and electric properties of $BiFeO_3$ thin films prepared by metal organic deposition method.* Applied Physics Letters, **89,** 2404942.

HUANG, F. Z., LU, X. M., WANG, Z., XU, S., WU, X. M. & ZHU, J. S. (2008) *Improved electric properties of Nd-doped $BiFeO_3$ thin films prepared by metal organic decomposition method.* Integrated Ferroelectrics, **96,** 112.

JAFFE, B., COOK, W. R. J. & JAFFE, H. (1971) *Piezoelectric Ceramics,* London, Academic Press.

JIANG, Q. H., NAN, C. W. & SHEN, Z. J. (2006) *Synthesis and properties of multiferroic La-modified $BiFeO_3$ ceramics.* Journal of the American Ceramic Society, **89,** 2123.

JONA, F. & SHIRANE, G. (1962) *Ferroelectric Crystals,* London, Pergamon Press.

JUN, Y.-K., LEE, S. B., KIM, M., HONG, S.-H., KIM, J. W. & KIM, K. H. (2007) *Dielectric and Magnetic Properties in Ta-Substituted $BiFeO_3$ Ceramics.* Journal of Materials Research, **22,** 3397.

KANAI, T., OHKOSHI, S., NAKAJIMA, A., WATANABE, T. & HASHIMOTO, K. (2001) *A ferroelectric ferromagnet composed of $(PLZT)_{(x)}(BiFeO_3)_{(1-x)}$ solid solution.* Advanced Materials, **13,** 487.

KARIMI, S., REANEY, I. M., HAN, Y., POKORNY, J. & STERIANOU, I. (2009a) *Crystal Chemistry and Domain Structure of Rare-Earth Doped $BiFeO_3$ Ceramics.* Journal of Materials Science, **44,** 5102.

KARIMI, S., REANEY, I. M., LEVIN, I. & STERIANOU, I. (2009b) *Nd-doped $BiFeO_3$ Ceramics with Antipolar Order.* Applied Physics Letters, **94,** 112903.

KISELEV, S. V., ZHDANOV, G. S. & OZEROV, R. P. (1962) *Detection of Magnetic Arrangement in Bifeo3 Ferroelectric by Means of Neutron Diffraction Study.* Doklady Akademii Nauk Sssr, **145,** 1255.

KISELEV, S. V., ZHDANOV, G. S. & OZEROV, R. P. (1963) *Detection of Magnetic Arrangement in $BiFeO_3$ Ferroelectric by Neutron Diffraction Study.* Soviet Physics - Crystallography, **7,** 742.

KNUDSEN, J. (2002) Structure-Property Relations ar the Antiferroelectric/Ferroelectric Phase Boundary in Undoped and La Doped $Pb(Zr,Ti)O_3$. *Engineering Materials.* Sheffield, The University of Sheffield.

KRAINIK, N. N., KHUCHUA, N. P., ZHDANOVA, V. V. & ESVEEV, V. A. (1966) *Phase Transitions in $BiFeO_3$.* Soviet Physics Solid State,Ussr, **8,** 654.

KUBEL, F. & SCHMID, H. (1990) *Structure of a Ferroelectric and Ferroelastic Monodomain Crystal of the Perovskite $BiFeO_3$.* Acta Crystallographica Section B-Structural Science, **46,** 698.

KUMAR, M. M., PALKAR, V. R., SRINIVAS, K. & SURYANARAYANA, S. V. (2000a) *Ferroelectricity in a pure $BiFeO_3$ ceramic.* Applied Physics Letters, **76,** 2764.

KUMAR, M. M., SRINATH, S., KUMAR, G. S. & SURYANARAYANA, S. V. (1998) *Spontaneous magnetic moment in $BiFeO_3$-$BaTiO_3$ solid solutions at low temperatures.* Journal of Magnetism and Magnetic Materials, **188,** 203.

KUMAR, M. M., SRINIVAS, A. & SURYANARAYANA, S. V. (2000b) *Structure property relations in $BiFeO_3$/$BaTiO_3$ solid solutions.* Journal of Applied Physics, **87,** 855.

LEE, Y. H., WU, J. M. & LAI, C. H. (2006) *Influence of La doping in multiferroic properties of $BiFeO_3$ thin films.* Applied Physics Letters, **88,** 042903.

LEVIN, I., KARIMI, S., PROVENZANO, V., DENNIS, C. L., WU, H., COMYN, T. P., STEVENSON, T. J., SMITH, R. I. & REANEY, I. M. (2010) *Reorientation of Magnetic Dipoles at the Antiferroelectric-Paraelectric Phase Transition of $Bi_{1-x}Nd_xFeO_3$ ($0.15 \leq x \leq 0.25$).* Physical Review B, **81,** 020103.

LIN, Y. H., JIANG, Q. H., WANG, Y., NAN, C. W., CHEN, L. & YU, J. (2007) *Enhancement of ferromagnetic properties in $BiFeO_3$ polycrystalline ceramic by La doping.* Applied Physics Letters, **90,** 172507.

MAREZIO, M., REMEIKA, J. P. & DERNIER, P. D. (1970a) *Crystal Chemistry of Rare Earth Orthoferrites*. Acta Crystallographica Section B-Structural Crystallography and Crystal Chemistry, **B 26,** 2008.

MAREZIO, M., REMEIKA, J. P. & DERNIER, P. D. (1970b) *On Space Group of Rare Earth Orthoferrites and Related Compounds*. Acta Crystallographica Section B-Structural Crystallography and Crystal Chemistry, **B 26,** 300.

MATHE, V. L., PATANKAR, K. K., PATIL, R. N. & LOKHANDE, C. D. (2004) *Synthesis and dielectric properties of $Bi_{1-x}Nd_xFeO_3$ perovskites*. Journal of Magnetism and Magnetic Materials, **270,** 380.

MATHE, V. L., PATANKAR, K. K., ROTHALE, M. B., KULKARNI, S. B., JOSHI, P. B. & PATIL, S. A. (2002) *Preparation, structural analysis and dielectric properties of $Bi_xLa_{1-x}FeO_3$ perovskite*. Pramana-Journal of Physics, **58,** 1105.

MEGAW, H. D. (1946) *Crystal Structure of Double Oxides of the Perovskite Type*. Proceedings of the Physical Society, **58,** 133.

MEGAW, H. D. (1973) *Crystal Structures: A Working Approach,* London, W. B. Saunders Company.

MICHEL, C., MOREAU, J.-M., ACHENBACH, G. D., GERSON, R. & JAMES, W. J. (1969a) *Atomic Structure of Two Rhombohedral Ferroelectric Phases in the $Pb(Zr,Ti)O_3$ Solid Solution Series*. Solid State Communications, **7,** 865.

MICHEL, C., MOREAU, J. M., ACHENBAC.GD, GERSON, R. & JAMES, W. J. (1969b) *Atomic Structure of $BiFeO_3$*. Solid State Communications, **7,** 701.

MISHRA, R. K., PRADHAN, D. K., CHOUDHARY, R. N. P. & BANERJEE, A. (2008) *Effect of yttrium on improvement of dielectric properties and magnetic switching behaviour in $BiFeO_3$*. Journal of Physics-Condensed Matter, **20**, 04521.

MITCHELL, R. H. (2002) *Perovskites Modern and Ancient,* Thunder Bay, Ontario, Canada, Almaz Press Inc.

MOREAU, J. M., MICHEL, C., GERSON, R. & JAMES, W. J. (1971) *Ferroelectric $BiFeO_3$ X-Ray and Neutron Diffraction Study*. Journal of Physics and Chemistry of Solids, **32,** 1315.

MOULSON, A. J. & HERBERT, J. M. (1990) *Electroceramics Materials. Propertis. Applications,* London, England, Chapman and Hall.

NALWA, K. S. & GARG, A. (2008) *Phase Evolution, Magnetic and Electrical Properties in Sm-Doped Bismuth Ferrite*. Journal of Applied Physics, **103**, 044101.

NALWA, K. S., GARG, A. & UPADHAYAYA, A. (2008a) *Solid state synthesis and characterization of multiferroic $BiFeO_3$ ceramics*. Indian Journal of Engineering and Materials Sciences, **15,** 91.

NALWA, K. S., GARG, A. & UPADHYAYA, A. (2008b) *Effect of samarium doping on the properties of solid-state synthesized multiferroic bismuth ferrite*. Materials Letters, **62,** 878.

NAVAROTSKY, A. (1998) *Energetics and Crystal Chemical Systematic Among Ilmenite, Lithium Niobate, and Perovskite Structure*. Chemistry of Materials, **10,** 1903.

NEATON, J. B., EDERER, C., WAGHMARE, U. V., SPALDIN, N. A. & RABE, K. M. (2005) *First Principle Study of Spontaneous Polarization in Multiferroic $BiFeO_3$* physical Review B, **71**, 014113.

NEEL, L. (1932) *Ann. de. Physique 17.*

NYE, J. F. (1985) *Physical Properties of Crystals: Their Representation by Tensors and Matrices,* Oxford, Clarendon Press.

PALKAR, V. R., JOHN, J. & PINTO, R. (2002) *Observation of saturated polarization and dielectric anomaly in magnetoelectric $BiFeO_3$ thin films.* Applied Physics Letters, **80,** 1628.

PALKAR, V. R., KUNDALIYA, D. C. & MALIK, S. K. (2003) *Effect of Mn substitution on magnetoelectric properties of bismuth ferrite system.* Journal of Applied Physics, **93,** 7834.

PANDIT, P., SATAPATHY, S., GUPTA, P. K. & SATHE, V. G. (2009) *Effect of coalesce doping of Nd and La on structure, dielectric, and magnetic properties of $BiFeO_3$.* Journal of Applied Physics, **106,** 7.

PRADHAN, A. K., ZHANG, K., HUNTER, D., DADSON, J. B., LOIUTTS, G. B., BHATTACHARYA, P., KATIYAR, R., ZHANG, J., SELLMYER, D. J., ROY, U. N., CUI, Y. & BURGER, A. (2005) *Magnetic and electrical properties of single-phase multiferroic $BiFeO_3$.* Journal of Applied Physics, **97**, 093903.

PUTNIS, A. (1992) *Introduction to Mineral Sciences* Cambridge, Cambridge University Press.

RANDALL, C. A., BARBER, D. J., WHATMORE, R. W. & GROVES, P. (1986) *A TEM Study of Ordering in Perovskites, $Pb(Sc_{1/2}Ta_{1/2})O_3$.* Journal of Material Science, **21,** 4456.

RAVINSKI, A. F., MAKOED, II, KOKOSHKEVICH, K., YANUSHKEVICH, K. I., GALYAS, A. I. & TRIGUK, V. V. (2007) *Magnetic properties and electron density distribution of $La_xBi_{1-x}FeO_3$.* Inorganic Materials, **43,** 860.

REANEY, I. M. (1996) Superlattices in Perovskites and Related Materials *Electroceramics V.* Portugal.

REANEY, I. M., COLLA, E. L. & SETTER, N. (1994) *Dielectric and Structural Characteristics of Ba- and Sr-Based Complex Perovskites as a Function of Tolerance Factor* Japanese Journal of Applied Physics **33,** 3984.

ROBERTS, S. (1950) *Dielectric Properties of Lead Zirconate and Barium-Lead Zirconate* Journal of American Ceramic Society, **32,** 63.

ROBERTS, S. (1951) *Piezoelectric Effect in Lead Zirconate.* Physical Review, **83,** 1078.

ROGINSKA.YE, TOMASHPO.YY, VENEVTSE.YN, PETROV, V. M. & ZHDANOV, G. S. (1966) *Nature of Dielectric and Magnetic Properties of $BiFeO_3$.* Soviet Physics Jetp-Ussr, **23,** 47.

ROYEN, P. & SWARS, K. (1957) *Das System Wismutoxyd-Eisenoxyd im Bereich von 0 bis 55 mol% eisenoxyd.* Angew. Chem., **69,** 779.

SAWAGUCHI, E., MANIWA, H. & HOSHINO, S. (1951a) *Antiferroelectric Structure of Lead Zirconate.* Pysical Review, Letters To The Editors, 1078.

SAWAGUCHI, E., SHIRANE, G. & TAGAKI, Y. (1951b) *Phase Transition in Lead Zirconate* Journal of Physical Society of Japan, **6,** 333.

SHANNON, R. D. (1993) *Dielectric Polarizabilities of Ions in Oxides and Fluorides* Journal of Applied Physics, **73,** 348.

SHANNON, R. D. & PREWITT, C. T. (1969) *Effective Ionic Radii in Oxides and Fluorides.* Acta Crystallographica, **B25,** 925.

SHIRANE, G., HOSHINO, S. & SUZUKI, K. (1950) *X-Ray Study of The Phase Transition in Lead Titanate* Physical Review Letters, **80,** 1105.

SHIRANE, G. & SUZUKI, K. (1951) *On the Phase Transition in Barium-Lead Titanate (1)* Journal of Physical Society of Japan, **6,** 274.

SHIRANE, G. & TAKEDA, A. (1952) *Phase Transitions in Solid Solutions of $PbZrO_3$ and $PbTiO_3$ (I) Small concentrations of $PbTiO_3$.* Journal of Physical Society of Japan, **7,** 5.

SMITH, R. T., ACHENBAC.GD, GERSON, R. & JAMES, W. J. (1968) *Dielectric Properties of Solid Solutions of $BiFeO_3$ with $Pb(Ti,Zr)O_3$ at High Temperature.* Journal of Applied Physics, **39,** 70.

SMOLENSKII, G. A., YUDIN, V. M., SHER, E. S. & STOLYPIN, Y. E. (1963) *Antiferromagnetic Properties of Some Perovskites.* Soviet Physics - Crystallography, **16,** 622.

SOSNOWSKA, I., PETERLIN-NEUMAIER, T. & STEICHELE, E. (1982) *Spiral Magnetic Ordering in Bismuth Ferrite.* Journal of Physics C: Solid State Physics, **15,** 4835.

SOSNOWSKA, I., PRZENIOSLO, R., FISCHER, P. & MURASHOV, V. A. (1994) *Investigation of Crystal and Magnetic-Structure of $BiFeO_3$ Using Neutron-Diffraction.* Acta Physica Polonica A, **86,** 629.

SOSNOWSKA, I., PRZENIOSLO, R., FISCHER, P. & MURASHOV, V. A. (1996) *Neutron diffraction studies of the crystal and magnetic structures of $BiFeO_3$ and $Bi_{0.93}La_{0.07}FeO_3$.* Journal of Magnetism and Magnetic Materials, **160,** 384.

SOSNOWSKA, I., SCHAFFER, W., KOCKELMANN, W., ANDERSEN, K. H. & TROYANCHUK, I. O. (2002) *Crystal structure and spiral magnetic ordering of $BiFeO_3$ doped with manganese.* Applied Physics A-Materials Science & Processing, **74,** S1040.

SPERANSKAYA, E. I., SKORIKOV, V. M., RODE, E. Y. & TEREKHOVA, V. A. (1965) *Phase diagram of the system of bismuth oxide-iron oxide.* Bull. Acad. Sci. USSR. Div. Chem. Sci. (English Translation) **5,** 873.

STERIANOU, I. (2008) Bismuth-Based Perovskites for High Temperature Piezoelectric Applications. *Engineering Materials.* Sheffield, The University of Sheffield.

STEVENSON, T., COMYN, T. P., BELL, A. J. & CYWINSKI, R. (2007) *Multiferroic (ferroelectro-magnetic) properties of bismuth ferrite lead titanate (x)($BiFeO_3$)-(1-x)($PbTiO_3$).* 2007 Sixteenth Ieee International Symposium on the Applications of Ferroelectrics, Vols 1 and 2, 421.

TEAGUE, J. R., GERSON, R. & JAMES, W. J. (1970) *Dielectric hysteresis in single crystal $BiFeO_3$.* Solid State Communications, **8,** 1073.

UCHIDA, H., YENO, R., NAKAKI, H., FANAKUBO, H. & KODA, S. (2005) *Ion Modification for Improvement of Insulating and Ferroelectric Properties of $BiFeO_3$ Thin Films Fabricated by Chemical Solution Deposition.* Japanese Journal of Applied Physics, **44,** L561.

UCHINO, K. (1997) *Piezoelectric Actuators and Ultrasonic Motors*, Kluwar Academic Publishers.

UNIYAL, P. & YADAV, K. L. (2008) *Study of dielectric, magnetic and ferroelectric properties in $Bi_{1-x}Gd_xFeO_3$.* Materials Letters, **62,** 2858.

VALASEK, J. (1921) *Piezo-electric and Allied Phenomena in Rochelle Salt.* Physical Review **17,** 475.

WANG, J., NEATON, J. B., ZHENG, H., NAGARAJAN, V., OGALE, S. B., LIU, B., VIEHLAND, D., VAITHYANATHAN, V., SCHLOM, D. G., WAGHMARE, U. V., SPALDIN, N. A., RABE, K. M., WUTTIG, M. & RAMESH, R. (2003) *Epitaxial $BiFeO_3$ Multiferroic Thin Film Heterostructures.* Science, **299,** 1719.

WANG, Y. P., ZHOU, L., ZHANG, M. F., CHEN, X. Y., LIU, J. M. & LIU, Z. G. (2004) *Room-temperature saturated ferroelectric polarization in $BiFeO_3$ ceramics synthesized by rapid liquid phase sintering.* Applied Physics Letters, **84,** 1731.

WEST, A. R. (1999) *Basic Solid State Chemistry,* Chichester, West Sussex, England, John Wiley & Sons Ltd.

WONRATSCHEK, H. & JEITSCHKO, W. (1976) *Twin Domains and Antiphase Domains.* Acta Crystallographica, **A32,** 664.

WOODWARD, D. I. (2004) The Crystal Chemistry of Bismuth-Based Perovskite Solid Solutions. *Engineering Materials.* Sheffield, The University of Sheffield.

WOODWARD, D. I., WISE, P. L., LEE, W. E. & REANEY, I. M. (2006) *Space Group Symmetry of $(Ca_xSr_{1-x})TiO_3$ Determined Using Electron Diffraction* Journal of Physics: Condensed Matter, **18,** 2401.

WOODWARD, P. M. (1997) *Octahedral tilting in perovskites. II. Structure stabilizing forces.* Acta Crystallographica, **B53,** 44.

YONEDA, Y., YOSHII, K., SAITOH, H. & MIZUKI, J. (2007) *Magnetic and ferroelectric properties of $(Bi_{1-x}La_x)FeO_3$.* Ferroelectrics, **348,** 435.

YUAN, G. L. & OR, S. W. (2006a) *Enhanced piezoelectric and pyroelectric effects in single-phase multiferroic $Bi_{1-x}Nd_xFeO_3$ (x=0-0.15) ceramics.* Applied Physics Letters, **88,** 062905.

YUAN, G. L. & OR, S. W. (2006b) *Multiferroicity in polarized single-phase $Bi_{0.875}Sm_{0.125}FeO_3$ ceramics.* Journal of Applied Physics, **100,** 024109.

YUAN, G. L., OR, S. W. & CHAN, H. L. W. (2007) *Structural transformation and ferroelectric-paraelectric phase transition in $Bi_{1-x}La_xFeO_3$ (x=0-0.25) multiferroic ceramics.* Journal of Physics D-Applied Physics, **40,** 1196.

YUAN, G. L., OR, S. W., LIU, J. M. & LIU, Z. G. (2006a) *Structural transformation and ferroelectromagnetic behaviour in single-phase $Bi_{1-x}Nd_xFeO_3$ multiferroic ceramics.* Applied Physics Letters, **89,** 052905.

YUAN, G. L., OR, S. W., WANG, Y. P., LIU, Z. G. & LIU, J. M. (2006b) *Preparation and multi-properties of insulated single-phase $BiFeO_3$ ceramics*. Solid State Communications, **138,** 76.

YUN, K. Y., RICINSCHI, D., KANASHIMA, T., NODA, M. & OKUYAMA, M. (2004) *Giant ferroelectric polarization beyond 150 mu C/cm(2) in $BiFeO_3$ thin film*. Japanese Journal of Applied Physics Part 2-Letters & Express Letters, **43,** L647.

ZALESSKII, A. V., FROLOV, A. A., KHIMICH, T. A. & BUSH, A. A. (2003) *Composition-induced transition of spin-modulated structure into a uniform antiferromagnetic state in a $Bi_{1-x}La_xFeO_3$ system studied using Fe-57 NMR*. Physics of the Solid State, **45,** 141.

ZHANG, S. T., PANG, L. H., ZHANG, Y., LU, M. H. & CHEN, Y. F. (2006a) *Preparation, structures, and multiferroic properties of single phase $Bi_{1-x}La_xFeO_3$ (x=0-0.40) ceramics*. Journal of Applied Physics, **100**, 114108.

ZHANG, S. T., ZHANG, Y., LU, M. H., DU, C. L., CHEN, Y. F., LIU, Z. G., ZHU, Y. Y., MING, N. B. & PAN, X. Q. (2006b) *Substitution-induced phase transition and enhanced multiferroic properties of $Bi_{1-x}La_xFeO_3$ ceramics*. Applied Physics Letters, **88**, 162901.

ZHENG, H., BAGSHAW, H., REANEY, I. M., UBIC, R. & YARWOOD, J. (2003) *Raman Spectroscopy and Microwave Properties of $CaTiO_3$-Based Ceramics*. Journal of Applied Physics, **94,** 2948.

Chapter 3: Experimental Procedure

3.1. Ceramic Processing

3.1.1. Synthesis

$(Bi_{1-x}Re_x)FeO_3$ compositions, based on Table 3.1, were produced using Bi_2O_3 (99.9 %, Acros Organics), Fe_2O_3 (99.8 %, Alfa Aesar), La_2O_3 (99.99 %, Sigma Aldrich), Nd_2O_3 (99.9 %, Sigma Aldrich), Sm_2O_3 (99.9 %, Acros Organics), and Gd_2O_3 (99.9 %, Acros Organics) as the starting materials.

Table 3.1. Compositions

RE ion	x
La^{3+}	0, 5, 10, 15, 20, 25, 30, 35, 40
Nd^{3+}	0, 5, 10, 15, 17.5, 20, 25
Sm^{3+}	0, 5, 10, 12.5, 15, 17.5
Gd^{3+}	0, 5, 7.5, 10, 12.5

After drying the oxides for 2 hours at temperatures listed in Table 3.2 , the appropriate powders were weighed out in stoichiometric amounts in batches of ~ 50 g to an accuracy of 0.01 g and milled in a Union Process attrition miller Szegvari attritor type:B size:01HD (Akron, Ohio) for 1 hour using 3 mm diameter Y_2O_3-stabilised ZrO_2 milling media in propan-2-ol. The slurry was then dried at 80 °C for a day and the powder was collected and ground with a pestle and mortar in order to pass through a 355 μm mesh sieve.

Mixed powders were reacted in air in a lidded Al_2O_3 crucible for 3 hours at the optimum reaction temperature for each composition, which was 830 °C for undoped samples and 870 °C for doped samples, with a heating rate of 2 °C per minute. The optimum reaction temperature was determined as the lowest temperature at which only the perovskite phase was present by X-ray diffraction or when the least amount of secondary phase was present. After reacting, the powders were allowed to cool to room temperature in the furnace.

Table 3.2. Drying temperature of the raw material oxides

Temperature	Oxide
500 °C	Bi_2O_3, Fe_2O_3
900 °C	La_2O_3, Nd_2O_3, Sm_2O_3, Gd_2O_3

Reacted powders were attrition milled for 0.5 hour before being dried, ground and sieved as before. Approximately 5 g of powder was uniaxially pressed into a pellet of 10 mm diameter and sintered, covered in the same powder, in air on a CaO-stabilised ZrO_2 tile covered with Pt foil, beneath an upturned alumina crucible. Pellets were sintered for 3 hours at temperatures of 850 °C for $BiFeO_3$ without dopant, 960 °C for La-doped compositions and 920 °C for other compositions. A heating rate of 2 °C per minute was used and after sintering the pellets were allowed to cool to room temperature in the furnace. The optimum sintering temperature was judged to be that at which the proportion of secondary phases was minimal and density > 95% theoretical.

3.1.2. Density Measurements

Archimedes Bulk Density Measurement

The density of final pellets was measured using the 'Archimedes' method following the Equation 3.1. Pellets were weighed on an Oertling R20 (London, UK) mechanical balance (Tokyo, Japan) to an accuracy of 0.0001 g. A thin piece of string was tied around the pellets and reweighed (m_2) to the same accuracy. Pellets were then suspended in a small beaker of distilled water at a known temperature and their weight recorded (m_3). Finally, the pellets were reweighed after drying and removing the string (m_4). The principle of this method is that the difference between weights m_2 and m_3 is equal to the mass of water displaced by the pellet. By knowing the density of the water at the appropriate temperature, the volume of the pellet can be accurately determined.

$$\rho_{pellet} = \frac{m_1 \times \rho_{H2O}}{(m_2 - m_3) + (m_4 - m_1)} \tag{3.1}$$

Where:

ρ_{H2O} is the density of water at the experiment temperature (g/mm^3).

m_1 is the weight of pellet (g).

m_2 is the weight of pellet plus the string (g).

m_3 is the weight of the pellet plus the string in the water (g).

m_4 is the weight of the pellet in air after removal from water (g).

For each sintering temperature, a mean density and standard deviation was acquired.

Theoretical Density Calculation

The theoretical density was calculated based on Equation 3.2 for each composition. [West, 1999]

$$\rho_t = \frac{m \times Z}{N_A \times V_{cell}} \times 10^{27} \quad (3.2)$$

Where:

ρ_t : Theoretical density (kg/m^3)

m : Molecular weight (g)

Z : Number of formula units per unit cell

N_A : Avogadro constant (6.022141 × 10^{23} mol^{-1})

V_{cell} : Volume of the unit cell (Å^3), obtained from the least squares fit from the XRD traces of powdered pellets.

3.2. Characterisation

3.2.1. Particle Size Analysis

Particle size analysis (PSA) was performed on the reactants, the milled mixed oxides immediately prior to reacting, and the milled reacted oxides immediately prior to pellet formation. A Coulter LS130 laser particle size analyser (Beckman Coulter Ltd., High Wycombe, Bucks, UK) was used to obtain a size distribution profile for each powder, based on the diffraction of a laser beam by the suspension of particles in the machine. The diffracted beam is focussed by a Fourier lens and the 'Fraunhofer' general optical model used to produce the size distribution. A small sample of powder was placed on a watch glass and stirred into a few drops of an aqueous solution containing 5 volume% of Dispex N40 (Allied Colloids Group PLC, Bradford, UK). This was transferred to a small beaker, filled with water and placed in an ultrasonic bath for a few minutes to break up agglomerates. The particle size analyser was filled with 1.5 litres of water and the sample added with a pipette until the particle concentration was deemed appropriate by the automatic control. Each run was performed for 90 seconds with sonication, and after each run, 20 ml of an aqueous solution containing 5 volume% of Dispex N40 was added as a deflocculant. The combination of deflocculant and sonication breaks up the agglomerated particles, and a more accurate distribution is approached. When the addition of Dispex caused a negligible change to the particle sizes, the distribution was deemed to be accurate. Excess deflocculant is known to cause re-agglomeration and the particle size distribution therefore is taken as the smallest d_{90} value, 90 Vol% of particles less than this value.

3.2.2. X-ray Diffraction

X-ray diffraction (XRD) was used primarily to identify the phase assemblage of reactants, reacted powders and crushed sintered pellets. Pellets were crushed and ground to a powder with a pestle and mortar in acetone and treated as other powders. Powders were compressed into aluminium sample holders and placed in a Siemens D500 diffractometer operating at 40 kV and 30 mA and exposed to Copper Kα radiation with a wavelength of $\lambda = 1.540562$ Å. Hiltonbrooks software was used to run the diffractometer and the diffracted intensity measured in steps of 0.02 ° at a speed of 1 ° per minute across the 2θ-range of 20° - 70°. The subsequent data was formatted and analysed using the computer program 'STOE WinXPow'. Where the XRD data were used to fit lattice parameters, the crushed pellets were mixed with silicon in a powder to silicon weight ratio of ~ 2:1. The peak positions of the silicon (JCPDS card [27-1402]) were used to create a linear calibration polynomial. A refinement function in the WinXPow software was used to apply a least-squares fit to the calibrated peaks in order to obtain lattice parameters for a given crystal structure.

3.2.3. Scanning Electron Microscopy

Scanning electron microscopy (SEM) was performed on the raw materials, reacted and milled powder and the final sintered pellets. Powder samples were prepared by scattering a small amount of powder over a sticky carbon pad, fixed to an Al stub. Excess powder was knocked off and the stub and powder was carbon coated using an Edwards 'Speedivac' model 12E6/1598 coating unit (Crawley, UK).

For characterization of sintered pellets, samples were broken in half, mounted on Al stubs with the broken surface upright. The flat surfaces of the pellets painted with Acheson electrodag 1415M silver paint (Acheson Colloids Co., Cannock, UK) before carbon coating. Samples were examined with a JEOL JSM6400 (Tokyo, Japan) operating at 10-20 kV. The microscope was equipped with an INCAx-sight energy dispersive spectroscopy (EDS) X-ray detector (OXFORD Instrument, UK), which was used to collect spectra. Spectra were processed using INCA software in order to obtain qualitative chemical analysis of the sample.

3.2.4. Transmission Electron Microscopy

Transmission electron microscopy (TEM) was used to study grain boundary and domain morphologies. Further structural data was obtained using electron diffraction. Pellets were mounted on a grinding disc using a heat sensitive resin and both sides ground with silicon carbide paper to a final thickness of ~ 30 μm. A 3.05 mm diameter copper ring with a 1 mm diameter aperture was attached to the section with Devcon epoxy resin (Wellingborough, UK). A Gatan dual ion mill 600 model (Pleasanton, California, USA) operated with an accelerating voltage of 6 kV at a combined gun current of 0.6 mA and at an incidence angle of 12° or/and 15° was used to mill the samples to perforation. Samples were initially examined using a Philips EM420T (Eindhoven, Holland) microscope operating at 120 kV. However, the high density of many samples meant that this microscope was of limited usefulness and instead a Philips EM430T (Eindhoven, Holland) operating at 130 kV, was used to examine samples where greater sample penetration was required.

Simulations of electron diffraction patterns were created using CaRine Crystallography 3.1 software with the relevant structural parameters obtained from published data.

Temperature dependent in-situ diffraction patterns are courtesy of Dr. Ysong Han and Dr. Shu Miao.

3.2.5. Neutron Diffraction

Neutron Diffraction data was collected on POLARIS located on beamline N7 at the ISIS, Didcot, UK. POLARIS which receives a polychromatic beam of neutrons from the ambient temperature water moderator, as part of collaboration with Dr. T. Comyn, The University of Leeds. Sample position is 12.0 m from the moderator and the incident and transmitted neutron flux is monitored by two low frequency glass scintillator detectors positioned about 4m and 2.5 m before and after the sample position. POLARIS characteristic information is listed in Table 3.3 [ISIS, 2009].

During data collection powder samples, crushed sintered pellets, were held in thin walled 75mm long cylindrical vanadium sample cans with 11mm diameters. The sample cans were mounted on a 'candlestick' so that the centre of the sample is 314mm from the lower face of the aluminium plate on the candle stick, Figure 3.1.

The maximum beam dimensions at the sample position are 40mm high x 20mm wide. POLARIS detectors are arranged into four separate banks reffered to as A at very low angles, B at low angles, C at 2θ~90° and D at backscattering angles, Table 3.4 [ISIS, 2009].

Table 3.3. Characteristics of POLARIS neutron diffractor in ISIS [ISIS, 2009].

Beamline	N7
Moderator	316K H_2O poisoned at 1.5 cm
Sample position	12.0 m from moderator
Incident wavelength	0.1 - 6.0 Å
Incident energy	20 meV - 10 eV
Beam size at sample	4.0 cm (height) × 2.0 cm (width)
Data acquisition	Digital Alphastation 500/266

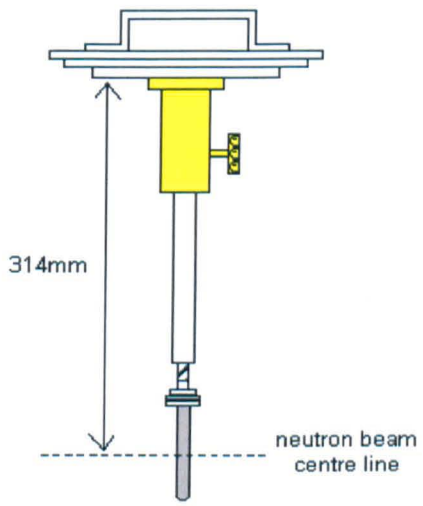

Figure 3.1. Sample alignment on POLARIS 'candlestick' [Smith and Hull, 2009].

Reitvield Refinements were performed by Dr. Igor Levin, NIST, USA using GSAS software package [Larson and Dreele, 2004]. The SARAh software was combined with GSAS for symmetry-constrained magnetic-structure refinements [Wills, 2000].

Table 3.4. POLARIS detector configuration [ISIS, 2009].

Bank position (Label)	Very low angle (A)	Low angle (B)	90 degrees (C)	Back scattering (E)
Type	ZnS scintillator	^{3}He gas tubes (½")	ZnS scintillator	^{3}He gas tubes (1")
No. of detectors	80	80	216	58
2θ range	13° - 15°	28° - 42°	85° - 95°	130° - 160°

3.2.6. Raman Spectroscopy

Raman Spectroscopy was used to investigate the short-range structural features in contrast to the average range structural features examined with X-ray and Neutron diffraction techniques. Renishaw InVia micro-Raman spectrometer was used to collect data from the polished surfaces of pellets. This spectrometer has five major parts as shown in Figure 3.2, including: excitation source, illumination of the sample and scattered light collecting system, sample stage, spectrograph or monochromator, and the detection system made of a detector, an amplifier and an output device [Gouadec and Colomban, 2007]. A more detailed diagram

of different components of a Raman Spectrometer is shown in Figure 3.3 [Ferraro *et al.*, 2003].

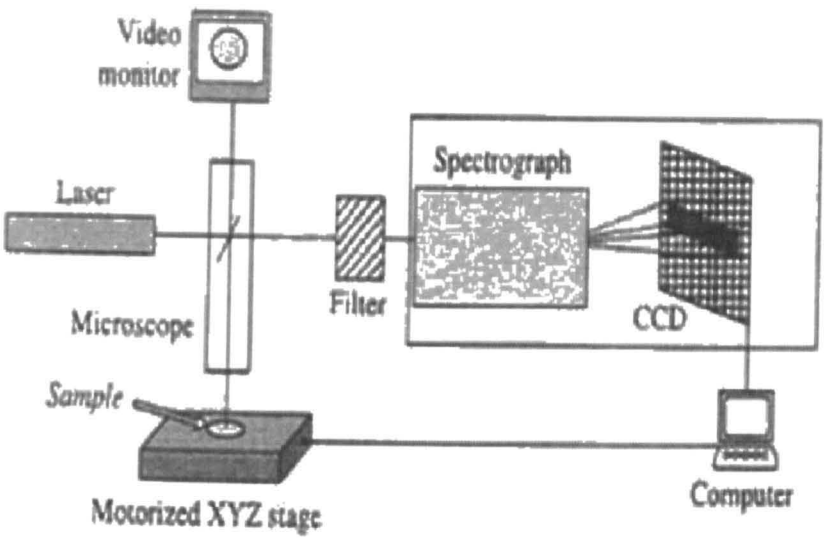

Figure 3.2. Principle of a conventional micro-Raman spectrometer [Gouadec and Colomban, 2007].

Unpolarised Raman spectra were excited with the 514.5 nm line of an Ar laser and recorded in back scattering geometry. Laser power of 4 mW was focused on a ~2 μm spot. The spectral resolution was ~1 cm^{-1}. A single-stage spectrograph, charge-coupled device detector and several types of filters were used to detect and filter the signal. The system was calibrated using Si spectra, at room temperature. For in-situ cooling and heating experiments, samples were placed in a Linkam cell (THMS600 Stage Linkam Scientific Instruments Ltd., 8 Epsom Downs Metro Centre, KT20 5HT, England). A TMS 94 temperature programmer was used to set the required heating/cooling cycles and the spectra were taken in the 100-1000 cm^{-1} range at 10 °C interval with the temperature stability of better than ± 1 °C.

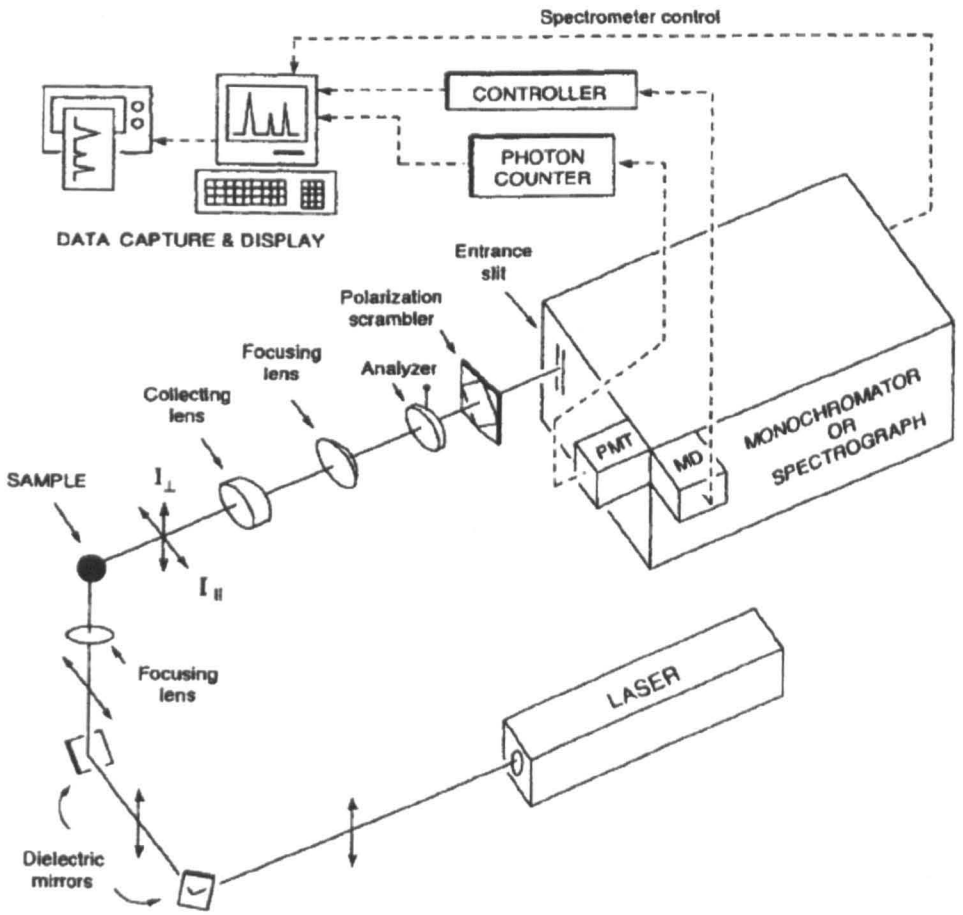

Figure 3.3. Schematic diagram of components of a Raman Spectrometer in more detail [Ferraro *et al.*, 2003].

3.2.7. Differential Scanning Calorimetry

Differential scanning calorimetry (DSC) was performed using a Netzsch DSC 404 C Pegasus controlled by a Netzsch Proteus software. Measurements were carried out in an air atmosphere with a constant cycle to remove volatile species from the furnace. Heating and cooling were carried out at 20 °C min^{-1}. Alumina crucibles were used with an empty crucible

serving as the reference. The sample crucible contained enough powder to fully cover the bottom of the crucible, about 40-50 mg weighed to 0.01 mg accuracy.

DSC is generally used to investigate structural phase transitions in materials by recording the heat input/output by comparing the energy required to maintain the sample and the reference at a set temperature. In a DSC there are two separate heating stages for the sample and the reference. For a sample with no thermal events the two stages will require the same amount of energy. However, if the sample undergoes and exothermic event the heating stage would require less energy than the reference stage needs to maintain the same temperature [West, 1999, Donovan, 2009].

3.2.8. Dielectric Measurements

Surface of disc-shaped pellets were coated with gold paste (T-10112, Metalor Technologies UK Ltd., Birmingham, UK). The gold coat was then sintered at 800 °C for 2 hours. A LCR meter (Model 4284A, Hewlett Packard) was used for capacitance and tanδ measurements. Measurements were carried out from temperature close to room temperature up to 830 °C with a heating rate of 1 °C min^{-1} with temperature, capacitance, and tanδ measured every 60 s. Capacitance values were converted to relative permittivity values using Equation 2.1. [Moulson and Herbert, 1990]

$$\varepsilon_r = \frac{C \times t}{\varepsilon_0 \times A} \qquad (2.1)$$

Where:

C: is capacitance (F).

t: is thickness of the disc shaped pellet (m).

A: is area of the disc surface (m^2).

ε_o: is the permittivity of free space 8.85419×10^{-12} (F/m).

3.2.9. Magnetic Measurements

Magnetic measurements are courtesy of Dr. Igor Levin, NIST, USA. Variable field and temperature magnetic measurements were performed on sintered pellets using a Quantum Design superconducting quantum interference device vibrating sample magnetometer working within the filed range of +5570 kA/m = 70000 Oe to -5570 kA/m and temperature range of 300 to 1000 K. The device is equipped with a sample oven that extends the maximum operating temperature to 1000 K. Before each variable-temperature scan the sample was first subjected to a strong magnetic field of 70000 Oe and the field was then reduced to a selected value [Levin, Karimi and co-workers, 2010].

3.3. References

DONOVAN, A. G. (2009) Structure-Property Relationships in Novel Bismuth-Based Electroceramics. *Engineering Materials.* The University of Sheffield.

FERRARO, J. R., NAKAMOTO, K. & BROWN, C. W. (2003) *Introductory Raman Spectroscopy*, Elsevier.

GOUADEC, G. & COLOMBAN, P. (2007) *Raman Spectroscopy of Nanomaterials: How Spectra Relate to Disorder, Particle Size and Mechanical Properties.* Progress in Crystal Growth and Characterization of Materials, **53,** 1.

ISIS (2009) Polaris Technical Information. http://www.isis.stfc.ac.uk/instruments/polaris/technical.

LARSON, A. C. & DREELE, R. B. V. (2004) General Structure Analysis System (GSAS). Los Alamos National Laboratory.

LEVIN, I., KARIMI, S., PROVENZANO, V., DENNIS, C. L., WU, H., COMYN, T. P., STEVENSON, T. J., SMITH, R. I. & REANEY, I. M. (2010) *Reorientation of Magnetic Dipoles at the Antiferroelectric-Paraelectric Phase Transition of $Bi_{1-x}Nd_xFeO_3$ ($0.15 \leq x \leq 0.25$).* Physical Review B, **81,** 020103.

MOULSON, A. J. & HERBERT, J. M. (1990) *Electroceramics Materials. Propertis. Applications,* London, England, Chapman and Hall.

SMITH, R. I. & HULL, S. (2009) User Guide for the Polaris Powder Diffractometer at ISIS. http://www.isis.stfc.ac.uk/instruments/polaris/documents.

WEST, A. R. (1999) *Basic Solid State Chemistry,* Chichester, West Sussex, England, John Wiley & Sons Ltd.

WILLS, A. S. (2000) *A New Protocol for the Determination of Magnetic Structures Using Simulated Annealing and Representational Analysis (SARAh).* Physica B-Condensed Matter, **276,** 680.

Chapter 4: Raw Materials and Processing

4.1. Characterisation of Raw Materials

4.1.1. Bismuth (III) Oxide, Bi_2O_3

Bismuth oxide, Bi_2O_3, purity 99.9 %, was supplied by Acros Organics (Geel, Belgium) with the manufacturer's assay listed in Table 4.1. The Bi_2O_3 powder is yellow and composed of plate-shaped particles with a mean diameter of 5 μm and d_{90} ~ 9 μm, Figures 4.1 and 4.2. The particle size distribution curve suggests a bimodal distribution of particles with the higher peak representing the plate-shaped particles and the lower peak representing sub-micron fragments. XRD and SEM (EDS) showed no impurity phases and the XRD pattern was fully indexed against the monoclinic α-Bi_2O_3 (ICDD card [41-1449]).

Table 4.1. Manufacturer's assay for Bi_2O_3.

Bi_2O_3	
Loss on drying	0.01 %
Trace analysis / Na	4.7 ppm
Cl	< 10 ppm
SO_4	< 10 ppm

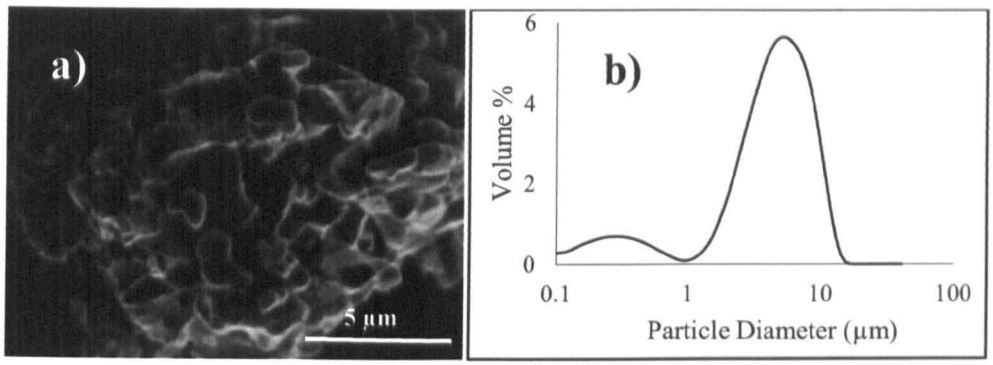

Figure 4.1. a) SEM image and b) particle size distribution for Bi_2O_3 powder.

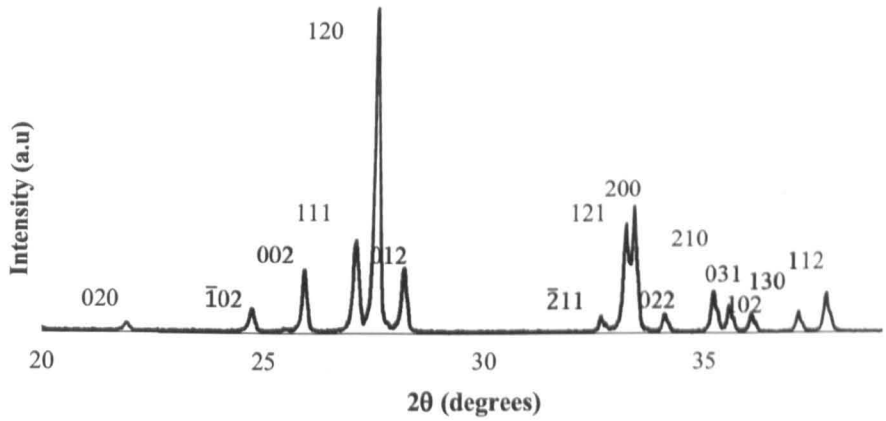

Figure 4.2. XRD trace of Bi_2O_3, indexed against ICDD card [41-1449].

4.1.2. Iron (III) Oxide, Fe_2O_3

Iron (III) oxide, Fe_2O_3, with +99% purity, was supplied by Alfa Aesar (Massachusetts, USA). The manufacturer's assay is listed in Table 4.2. The Fe_2O_3 powder has a deep red colour and is made of agglomerates exceeding 100 µm in diameter, Figure 4.3.

Table 4.2. Manufacturer's assay for Fe_2O_3.

Fe_2O_3	
Moisture	0.25 wt%
Water soluble salts	0.07 wt%

Particle size analysis gave a mean diameter of 1 μm and $d_{90} \sim 2$ μm and indicated that the primary Fe_2O_3 particles are sub-micron in diameter. However, the large agglomerates persisted, even with the addition of large volumes of deflocculant. No impurity phases were observed in the XRD traces, Figure 4.4, which was indexed successfully against rhombohedral Fe_2O_3 with ICDD card [33-664].

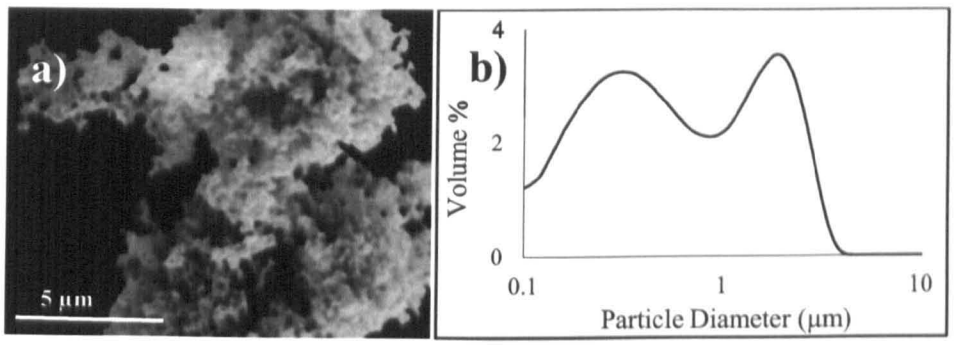

Figure 4.3. a) SEM image and b) particle size distribution for Fe_2O_3 powder.

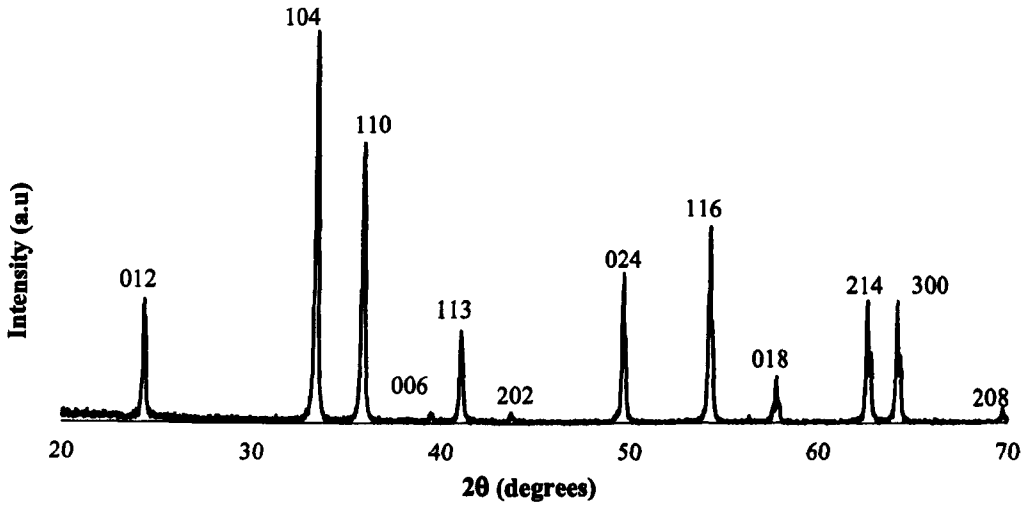

Figure 4.4. XRD trace of Fe_2O_3, indexed against the hematite structure, ICDD card [33-664].

4.1.3. Lanthanum Oxide, La_2O_3

La_2O_3, purity 99.99 %, was supplied by Sigma Aldrich Company Ltd (Dorset, UK) and the manufacturer's assay is listed in Table 4.3.

Table 4.3. Manufacturer's assay for La_2O_3.

La_2O_3	
Trace Metal Analysis	≤200.0 ppm
Ba, Ce, Fe, Nd, Pr, Th, Tm, V, Y, YB	ppm

La_2O_3 is a white powder consisting of agglomerates of micron and submicron sized primary particles, Figure 4.5. Particle size analysis gave a particle size distribution with a mean

diameter of 10 μm and d_{90} ~ 20 μm. It was concluded therefore, that the agglomerates persisted, even with the addition of large volumes of deflocculant.

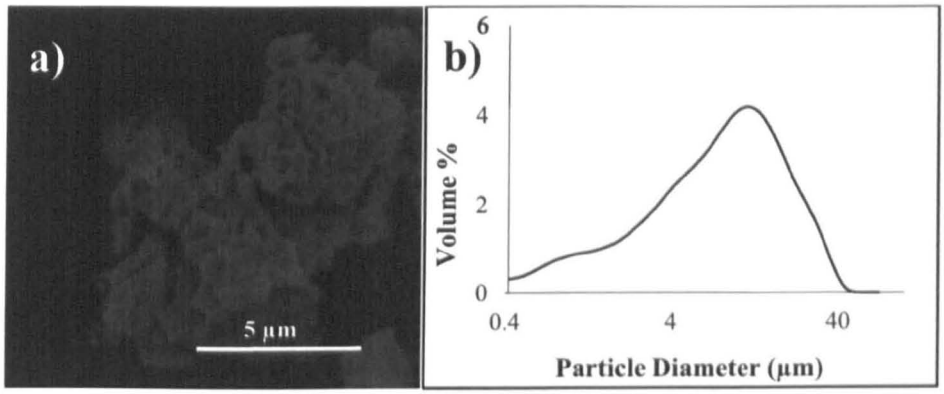

Figure 4.5. a) SEM image and b) particle size distribution for La_2O_3 powder.

No impurity phases were observed in the XRD traces, Figure 4.6, which could be indexed successfully against hexagonal La_2O_3 (ICDD cards [83-1344]).

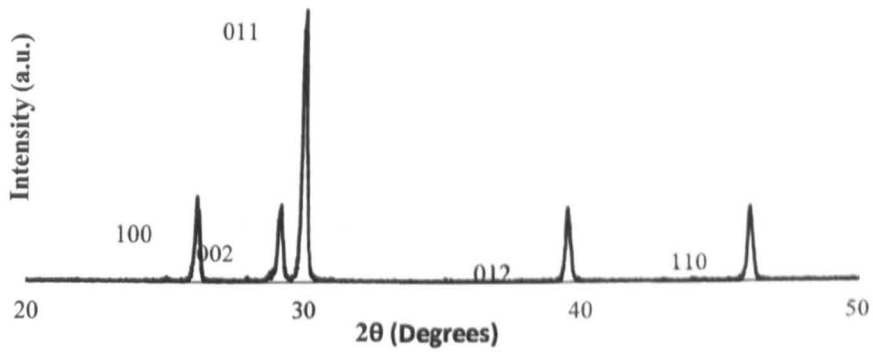

Figure 5.6. XRD trace of La2O3, indexed against the hexagonal structure, ICDD card [83-1344].

4.1.4. Neodymium Oxide, Nd_2O_3

Nd_2O_3, purity 99.90 %, was supplied by Sigma-Aldrich Company Ltd (Dorset, UK) and Table 4.4 shows the manufacturer's assay.

Table 4.4. Manufacturer's assay for Nd_2O_3.

Nd_2O_3	
Trace Rare Earth Analysis	≤ 2000.0 ppm
Mg, Yb	ppm

Nd_2O_3 is a light grey-blue powder that appears highly agglomerated, Figure 4.7. Even with the addition of a large volume of deflocculant the mean particle size did not decrease to < 7 μm with d_{90} ~ 14μm. No impurity were observed in the XRD traces, Figure 4.8, which were indexed successfully against hexagonal Nd_2O_3 (ICDD cards [74-1147]).

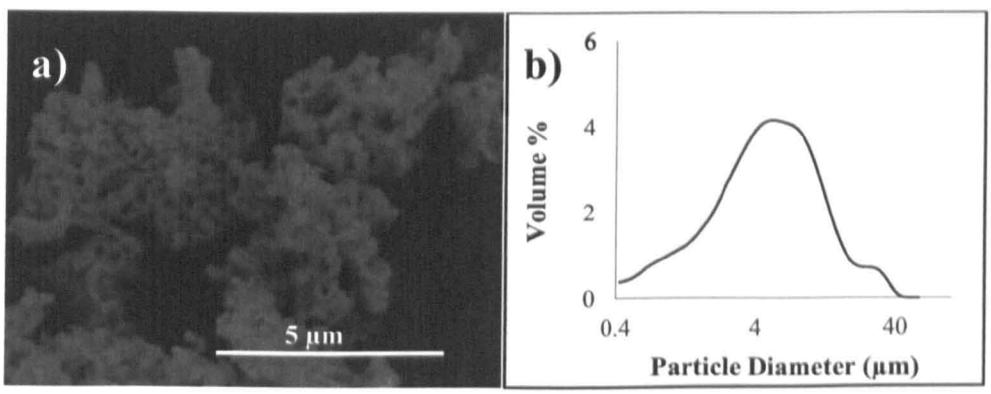

Figure 4.7. a) SEM image and b) particle size distribution for Nd_2O_3 powder.

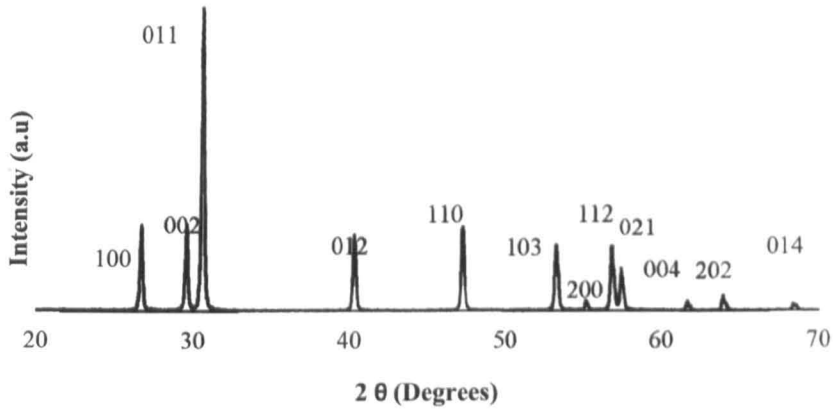

Figure 4.8. XRD trace of Nd2O3, indexed against the ICDD card [74-1147].

4.1.5. Samarium Oxide, Sm_2O_3

Sm_2O_3, purity 99.9 %, was supplied by Acros Organics (Geel, Belgium). Table 4.5 shows the manufacturer's assay. Sm_2O_3 is a cream-coloured powder composed agglomerated fine primary particles (10 μm diameter), Figure 4.9.

Table 4.5. Manufacturer's assay for Sm_2O_3.

Sm_2O_3	
Trace Rare Earth Analysis	≤2000.0 ppm
Na, Cs, Th, Ca, Sr, Ba, Y, Tb, Ti, Zn, La, Al, Ce, Cr, Pb, Pr, Bi, Fe, Yb	ppm

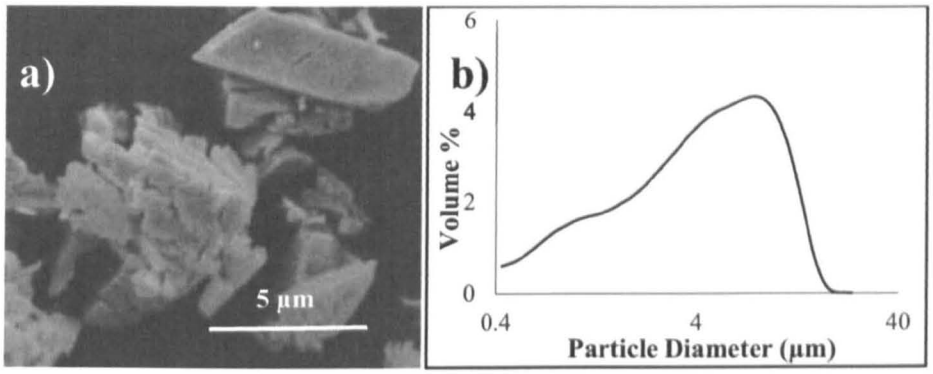

Figure 4.9. a) SEM image and b) particle size distribution for Sm_2O_3 powder.

Particle size analysis revealed a mean diameter of 5 μm and $d_{90} \sim 11\mu m$. No impurity peaks were found in the XRD which is indexed according to a mixture of monoclinic and cubic Sm_2O_3 (ICDD cards [74-1807] and [70-2642], respectively), Figure 4.10.

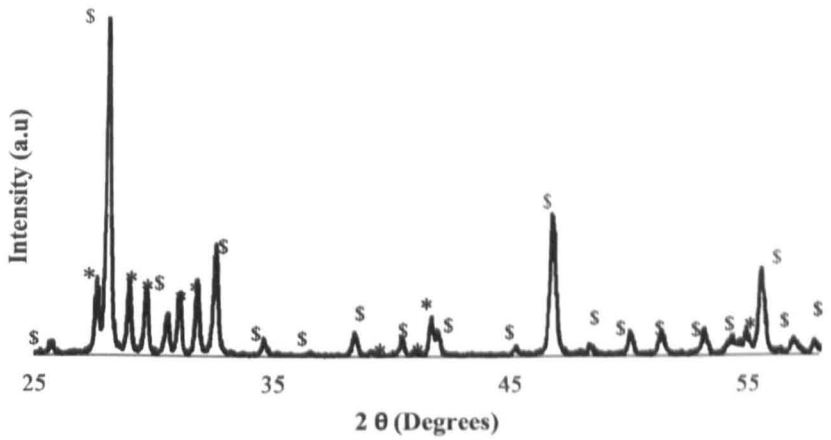

Figure 4.10. XRD trace of Sm2O3, indexed against the monoclinc * (ICDD card [70-2642]) and cubic $ (ICDD card [74-1807]) structures.

4.1.6. Gadolinium Oxide, Gd_2O_3

Gd_2O_3, purity 99.9 %, was supplied by Acros Organics (Geel, Belgium) with manufacturer's assay listed in Table 4.6. Gd_2O_3 came as a white powder composed of cuboid particles, Figure 4.11. XRD traces were indexed according to cubic symmetry, ICDD card [43-1014], with no impurity peaks, Figure 4.12. Particle size analysis confirmed the small size of particles observed by SEM, Figure 4.11, giving a mean diameter of 2 μm and d_{90} ~ 5 μm.

Table 4.6. Manufacturer's assay for Gd_2O_3.

Gd_2O_3	
Trace Rare Earth Analysis	≤2000.0 ppm
Na, K, Rb, Cs, Mg, Ca, Sr, Ag, Ba, Y, Tb, Hf, La, Dy, B, Al, Ce, Ho, Si, W, Pb, Pr, Er, Mn, Re, Nd, Tm, Fe, Os, Sm, Ir, Eu	ppm

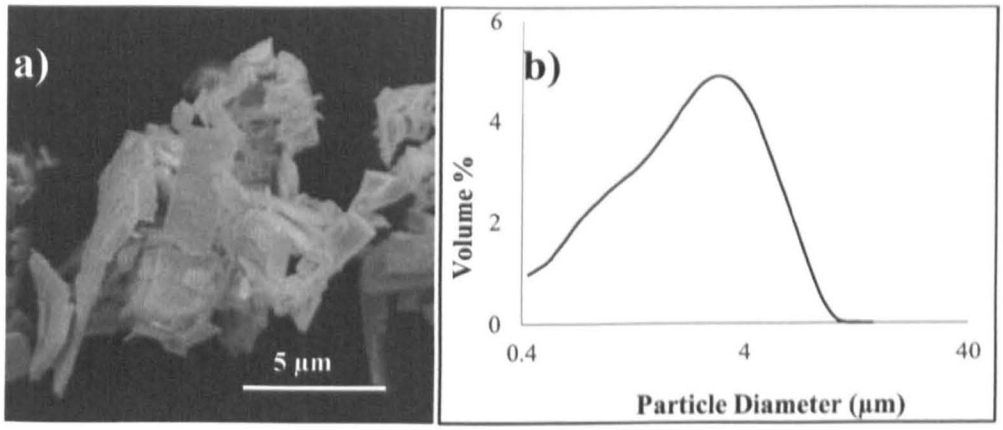

Figure 4.11. a) SEM image and b) particle size distribution for Gd_2O_3 powder.

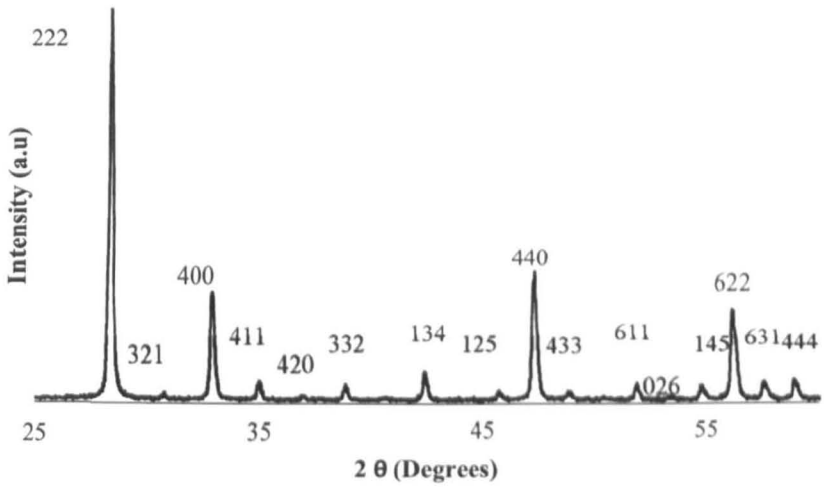

Figure 4.12. XRD trace of Gd_2O_3, indexed against cubic structure with ICDD card [43-1014].

4.2. Ceramic Processing

4.2.1. Reaction of Raw Materials

All batched oxides were attrition milled for 1h prior to reaction which led to a much smaller size and distribution of the reactants particles listed in Table 4.7. All the milled/mixed powders showed a similar particle size distribution in the range, 2-6 μm, considerably smaller than the size distribution of the starting raw materials. Smaller particles are desirable for making single-phase dense and homogenous ceramics at lower temperatures.

Table 4.7. Particle size of mixed oxides in $Bi_{1-x}RE_xFeO_3$ series after 1 hour of attrition milling before reacting.

$Bi_{1-x}La_xFeO_3$		**$Bi_{1-x}Nd_xFeO_3$**		**$Bi_{1-x}Sm_xFeO_3$**		**$Bi_{1-x}Gd_xFeO_3$**	
x	**d_{90} (μm)**	***x***	**d_{90} (μm)**	***x***	**d_{90} (μm)**	***x***	**d_{90} (μm)**
0	3	**0**	3	**0**	3	**0**	3
5	4	**5**	4	**5**	5	**5**	5
10	5	**10**	6	**10**	4	**7.5**	4
15	2	**15**	4	**12.5**	6	**10**	6
20	4	**17.5**	5	**15**	4	**12.5**	6
25	3	**20**	6	**17.5**	3	**15**	5
30	2	**25**	4	**20**	2	**20**	-
40	4						

The reaction temperatures for undoped and RE doped compositions were 830 °C and 860 °C, respectively. These temperatures were determined by undertaking a systematic reaction study

in the range of 780-900 °C. The optimum temperature was taken as the lowest reaction temperature at which only the target phase was present by XRD or when the least amount of secondary phase was present with the caveat that the resultant powder was soft enough not to cause difficulty with further processing.

The weight losses encountered during the reaction are listed in Table 4.8. The weight loss was assumed to be associated with the volatilisation of Bi_2O_3 in addition to the loss of absorbed water. The latter mechanism is consistent with the higher weight loss associated with the more hygroscopic compositions of the La-doped series.

Table 4.8. Weight loss for reacted powder in the $Bi_{1-x}RE_xFeO_3$ series.

$Bi_{1-x}La_xFeO_3$		$Bi_{1-x}Nd_xFeO_3$		$Bi_{1-x}Sm_xFeO_3$		$Bi_{1-x}Gd_xFeO_3$	
x	**Weight loss %**	***x***	**Weight loss %**	***x***	**Weight loss %**	***x***	**Weight loss %**
0	0.01	**0**	0.01	**0**	0.01	**0**	0.01
5	0.01	**5**	0.01	**5**	0.01	**5**	0.01
10	0.01	**10**	0.01	**10**	0.03	**7.5**	0.01
15	0.03	**15**	0.02	**12.5**	0.02	**10**	0.01
20	0.03	**17.5**	0.02	**15**	0.02	**12.5**	0.01
25	0.04	**20**	0.03	**17.5**	0.02	**15**	0.01
30	0.04	**25**	0.03	**20**	0.02		
40	0.05						

Following the reaction, all powders were attrition milled for 0.5 hour to obtain a more homogenous fine particle size ready to press into pellets. The resultant particle sizes are listed in Table 4.9.

To provide more information on the nature of the reaction, differential thermal analysis was performed on mixed raw oxides in the $Bi_{1-x}Nd_xFeO_3$ $0 \leq x \leq 0.25$ system with a heating and cooling rate of 2 °C per minute, Figure 4.13. For RE doped samples, sharp peaks were observed at ~300 °C on cooling, Figure 4.13b. The origin of these peaks is unknown. For undoped samples, there is a small but sharp endothermic and exothermic peak at ~820 °C in the heating and cooling trace, respectively, which may correspond to the ferroelectric T_C.

Table 4.9. Particle sizes of reacted compositions after 1 hour of attrition milling.

$Bi_{1-x}La_xFeO_3$		$Bi_{1-x}Nd_xFeO_3$		$Bi_{1-x}Sm_xFeO_3$		$Bi_{1-x}Gd_xFeO_3$	
x	d_{90} (μm)	x	d_{90} (μm)	x	d_{90} (μm)	x	d_{90} (μm)
0	2	**0**	2	**0**	2	**0**	2
5	4	**5**	4	**5**	4	**5**	3
10	4	**10**	2	**10**	4	**7.5**	3
15	3	**15**	3	**12.5**	3	**10**	2
20	3	**17.5**	3	**15**	3	**12.5**	3
25	2	**20**	3	**17.5**	3	**15**	3
30	2	**25**	2	**20**	2	-	-
40	3						

The weaker and broader peaks to the left of the sharp peaks may indicate the formation of $BiFeO_3$. Other peaks at higher temperatures in the $BiFeO_3$ DTA traces most probably relate to the formation of secondary phases. At about 930 °C, $BiFeO_3$ decomposes to $Bi_2Fe_4O_9$ and liquid phase while the decomposition of $Bi_2Fe_4O_9$ takes place at about 960 °C [Speranskaya *et al.*, 1965]. The heating and cooling traces of RE-doped compositions, e.g. $Bi_{0.85}Nd_{0.15}FeO_3$ in Figure 4.13a are largely featureless in comparison with that of $BiFeO_3$, exhibiting only

broad peaks barely detectable above the background (e.g. at ~700 °C). This suggests that the reaction is slower for undoped compositions and also that T_C is more diffuse, consistent with the incorporation of the more refractory RE oxide in the lattice.

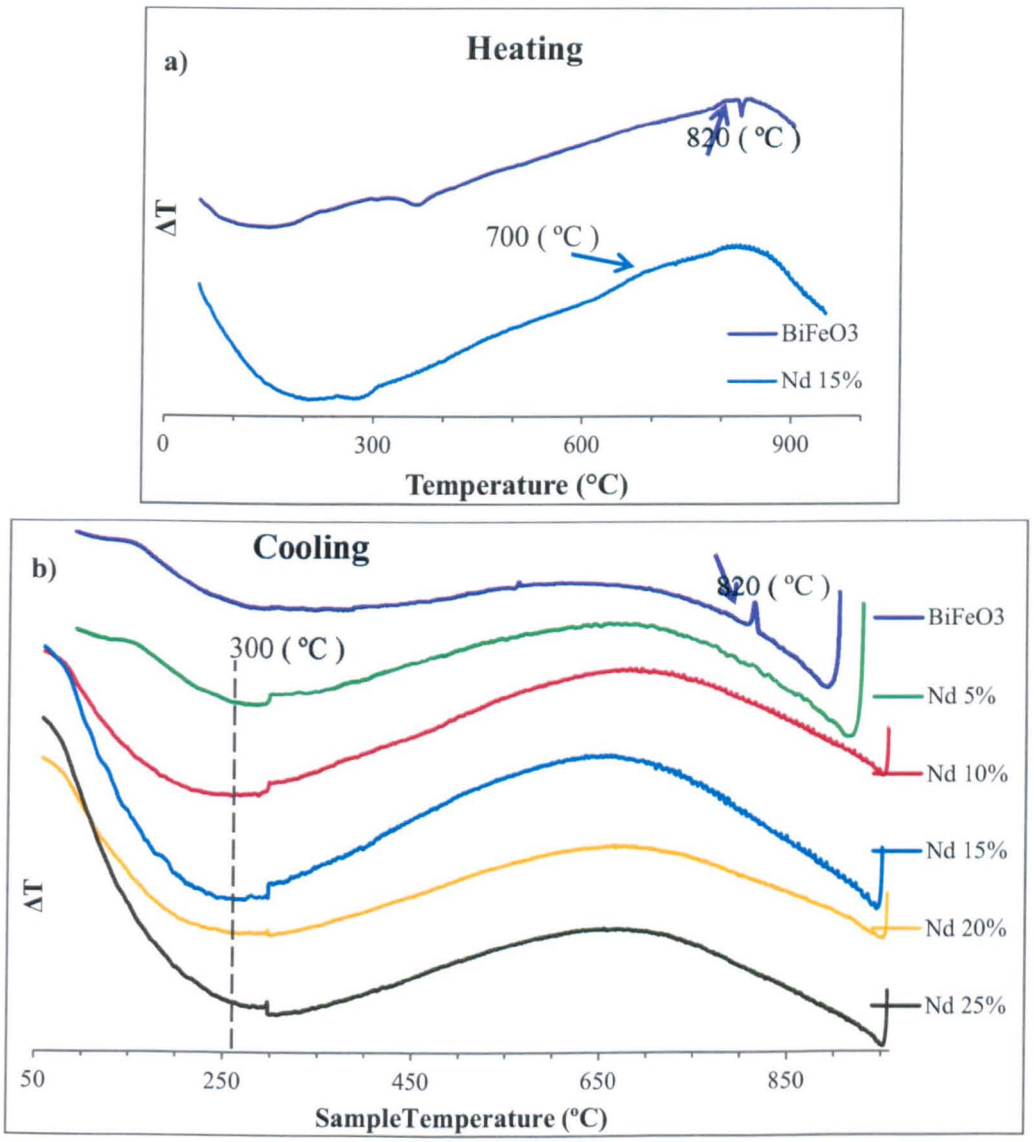

Figure 4.13. a) Heating and b) Cooling DTA traces of mixed raw oxides in the Nd-doped series.

4.2.2. Sintering of Pellets

Following the milling of reacted powders, pellets were uniaxially pressed and sintered at the temperatures listed in Table 4.10. These were determined after performing sintering experiments in the range 830-980 °C aiming for the highest density at which secondary phases were absent or minimised. The results of the sintering study for $BiFeO_3$ and $Bi_{0.85}Nd_{0.15}FeO_3$ are presented in Figure 4.14. Weight loss of the pellets after sintering was negligible (~ 0.01%). For undoped samples, the highest density was achieved at 870 °C but such high temperatures resulted in a greater fraction of secondary phases in comparison to ceramics sintered at 850 °C. For this reason, 850 °C was chosen as the sintering temperature for the fabrication of undoped $BiFeO_3$ ceramics.

Table 4.10. Optimum sintering temperatures for different dopant percentages.

Temperature (°C)	**La %**	**Nd %**	**Sm %**	**Gd %**
850	0	0	0	0
900	5	5	5	5, 7.5, 10
930	10, 15	10, 15, 17.5, 20	10, 12.5, 15, 17.5, 20	12.5, 15
960	20, 25, 30	25	-	-

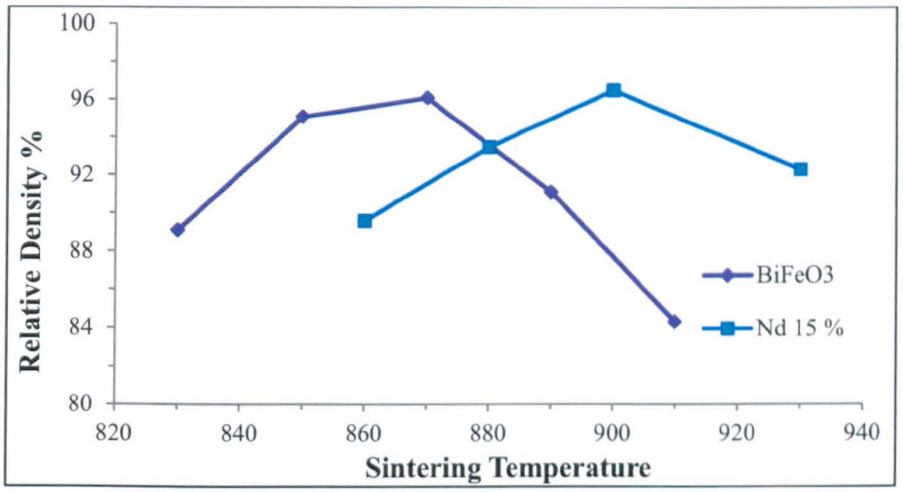

Figure 4.14. Relative density vs sintering temperature for $BiFeO_3$ without dopant and with 15% Nd.

Figure 4.15 shows the XRD traces of the crushed sintered pellets in the series $Bi_{1-x}Nd_xFeO_3$. $BiFeO_3$ could be indexed according to the required rhombohedral phase, however, second phases were invariably present despite repeated attempts to improve the processing and modify the sintering temperatures. Second phases such as $BiFe_2O_4$ and Bi-rich sillenites are commonly observed in the fabrication on $BiFeO_3$ [Sosnowska *et al.*, 1982]. As Nd concentration increases, the fraction of secondary phase decreases and all compositions with $x > 0.5$ were single phase within the detection limits of XRD. Compositions with $x<0.15$ could be indexed with a rhombohedral structure, $0.15 \leq x < 0.25$ orthorhombic and $x \geq 0.25$ orthorhombic with the $GdFeO_3$ structure [Karimi *et al.*, 2009]. These results will be discussed in greater detail in the next chapter.

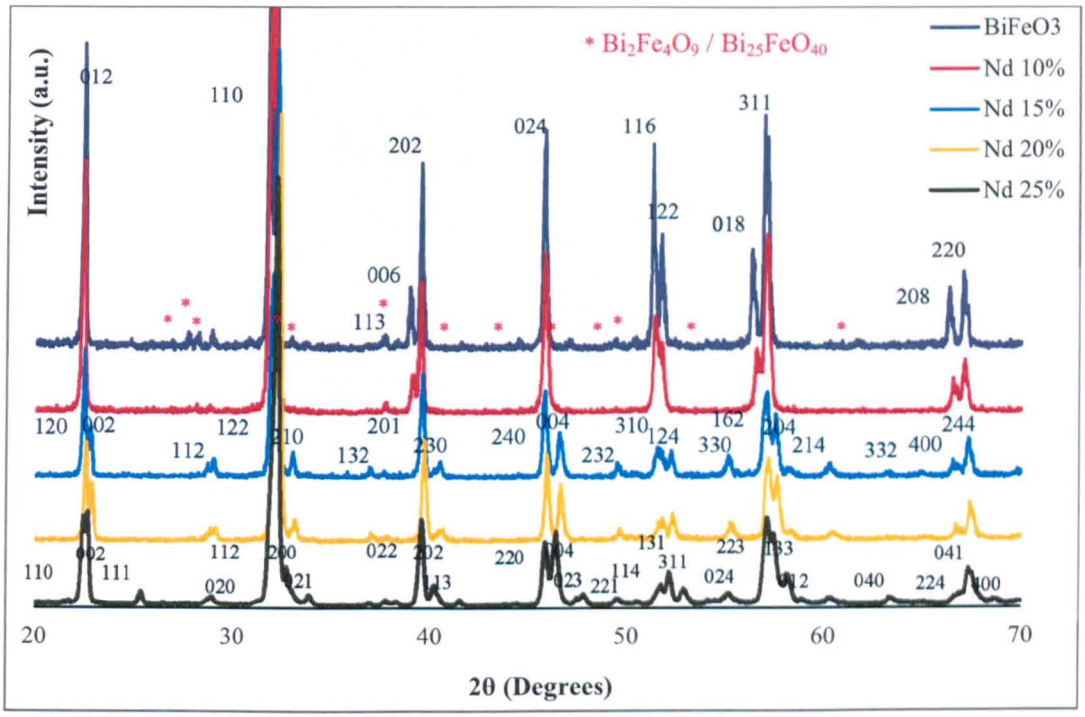

Figure 4.15. XRD traces of crushed sintered pellets for Nd-doped $BiFeO_3$ indexed based on $BiFeO_3$ Rhombohedral structure [71-2494], $PbZrO_3$-Like Orthorhombic structure [70-4844] and $NdFeO_3$ Orthorombic Structure [74-1473].

SEM images of sintered pellets of $BiFeO_3$ and $Bi_{0.85}Nd_{0.15}FeO_3$ are presented in Figures 4.16 and 4.17, respectively. The $Bi_2Fe_4O_9$ and $Bi_{25}FeO_{40}$, evident in the XRD traces for $BiFeO_3$ (Figure 4.15) are also seen in the SEM images, Figure 4.16.

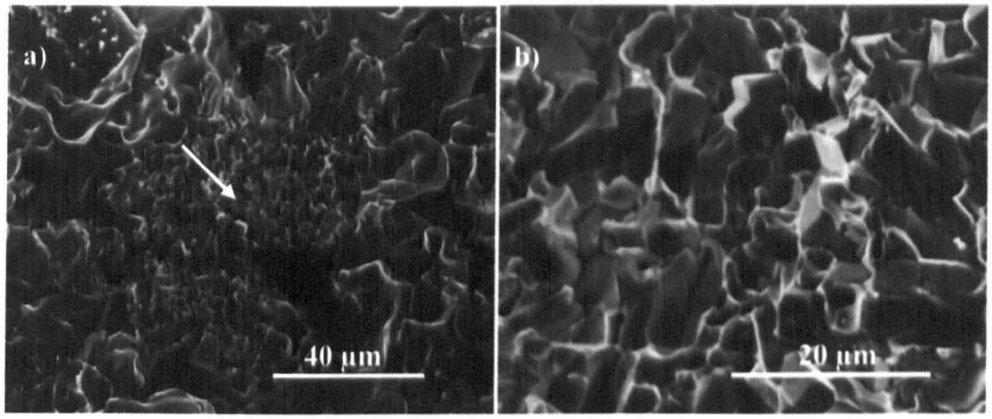

Figure 4.16. SEM images of $BiFeO_3$ showing a) the main phase and the bismuth rich secondary phase, indicated with the white arrow and b) the general compactness of the grains.

Figure 4.17a shows a back scattered image of polished surface of $Bi_{0.85}Nd_{0.15}FeO_3$. Some porosity is present but there is no evidence of secondary phases. Figure 4.17b shows the grain size within the bulk of a pellet of $Bi_{0.85}Nd_{0.15}FeO_3$. In general, RE doped ceramics showed smaller grain size.

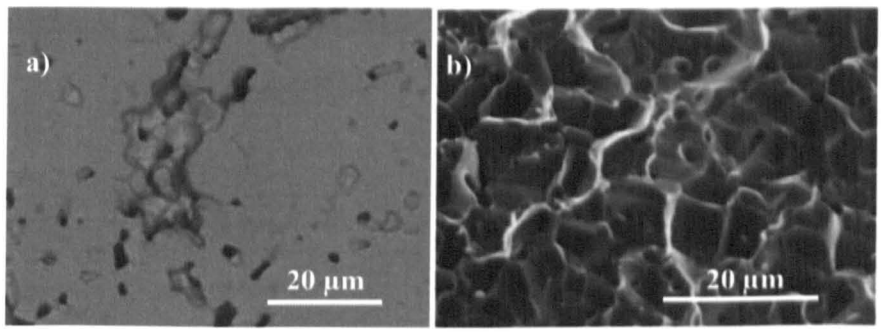

Figure 4.17. SEM images taken from a) the polished surface, and b) the bulk (fractured surface) of a pellet with composition $Bi_{0.85}Nd_{0.15}FeO_3$.

4.3. Summary

Ceramics of $BiFeO_3$ and RE-doped $BiFeO_3$ were successfully fabricated. $BiFeO_3$ contained some second phases, e.g. $BiFe_2O_4$, but for compositions with $x > 0.05$ all ceramics were single phase. All ceramics could be fabricated with > 95% theoretical density.

4. References

KARIMI, S., REANEY, I. M., LEVIN, I. & STERIANOU, I. (2009) *Nd-doped $BiFeO_3$ Ceramics with Antipolar Order.* Applied Physics Letters, **94**, 112903.

SOSNOWSKA, I., PETERLIN-NEUMAIER, T. & STEICHELE, E. (1982) *Spiral Magnetic Ordering in Bismuth Ferrite.* Journal of Physics C: Solid State Physics, **15**, 4835.

SPERANSKAYA, E. I., SKORIKOV, V. M., RODE, E. Y. & TEREKHOVA, V. A. (1965) *Phase diagram of the system of bismuth oxide-iron oxide.* Bull. Acad. Sci. USSR. Div. Chem. Sci. (English Translation) **5**, 873.

Chapter 5: Results

5.1. X-ray Diffraction

5.1.1. Undoped $BiFeO_3$

Single phase $BiFeO_3$ could not be obtained in the present study irrespective of the reaction time and temperature. Secondary phases, indexed as $Bi_2Fe_4O_9$ (ICDD card [25-90]) and sillenite, $Bi_{25}FeO_{40}$ (ICDD card [46-416]), were always visible in the XRD spectra but their volume fraction varied with reaction temperature, Figure 5.1. Although 850 °C gave the lowest volume fraction of secondary phases (Figure 5.1.1), the resulting powders were partially densified and difficult to regrind and pelletise. Consequently, a reaction temperature of 830 °C was chosen followed by sintering at a higher temperature. Figure 5.1.2 compares the XRD spectra from crushed pellets of samples reacted at 830 °C and then sintered at 850 °C and 870 °C. Consistent with the reaction study (Figure 5.1.1), samples sintered at 870 °C showed qualitatively more second phase than those sintered at 850 °C, Figure 5.1.2.

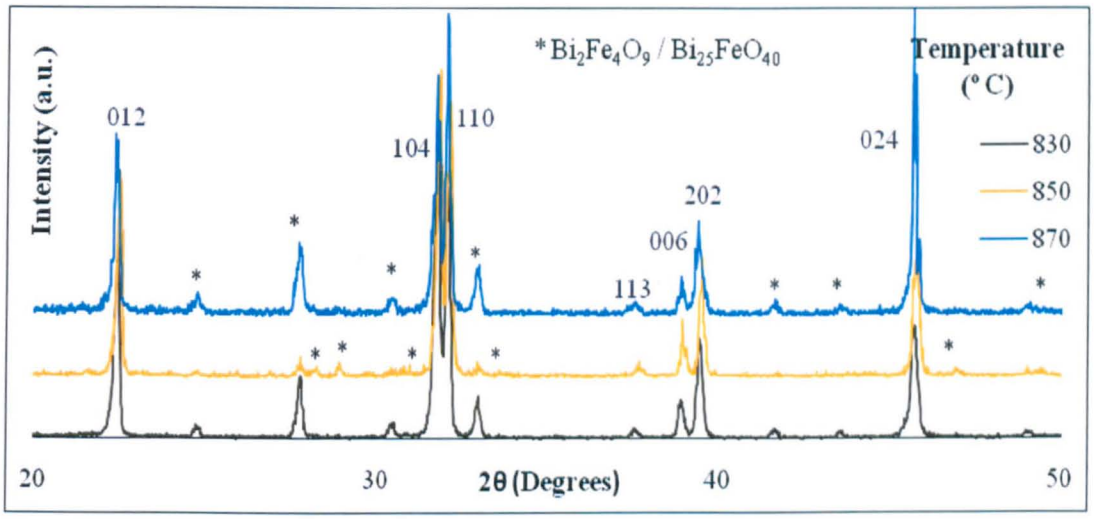

Figure 5.1.1. XRD traces of $BiFeO_3$ reacted at different temperatures.

For further study therefore, all undoped $BiFeO_3$ samples were reacted 3 hours at 830 °C and sintered 3 hours at 850 °C to form dense pellets. Second phases are commonly observed in $BiFeO_3$ ceramics [Sosnowska *et al.*, 1982]. Valant and co-workers [Valant *et al.*, 2007] have suggested that second phase may be eliminated by the use of super-pure raw materials and careful contol over reaction and sintering temperature. Other researchers have utilised different techniques including leaching to remove unwanted second phases after reaction but prior to sintering [Achenbach *et al.*, 1967, Filip'ev *et al.*, 1960]. More often however, substitutions on the A and B-sites have generally been reported to enhance the stability of the perovskite phase [Comyn *et al.*, 2004, Stevenson *et al.*, 2007, Woodward *et al.*, 2003]. Woodward et al. demonstrated that 10% $PbTiO_3$ substituted for $BiFeO_3$ eliminated second phase peaks from XRD traces [Woodward *et al.*, 2003]. Similar improvements in phase purity have been reported for the substitution of Bi by RE ions [Cheng *et al.*, 2008a, Cheng *et al.*, 2008b, Lee *et al.*, 2006, Nalwa and Garg, 2008, Nalwa *et al.*, 2008, Yuan and Or,

2006b, Yuan and Or, 2006a, Yuan *et al.*, 2006, Zalesskii *et al.*, 2003]. Since the goal of the project was to establish structure-property relations in RE-doped $BiFeO_3$, no further efforts were made to improve the phase purity of the Bi end member.

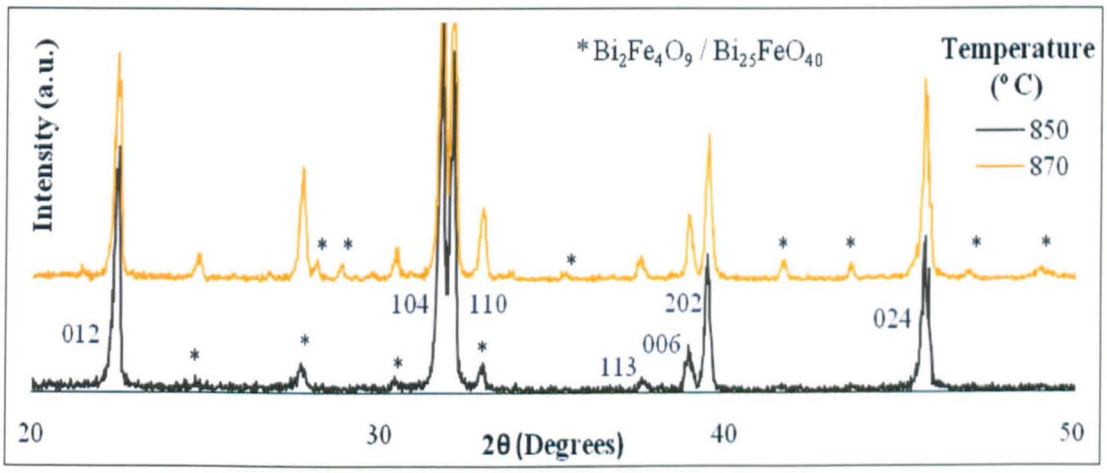

Figure 5.1.2. XRD traces of crushed pellets of $BiFeO_3$ sintered at different temperatures.

5.1.2. RE-Doped $BiFeO_3$

Figure 5.1.3 shows the XRD traces for crushed sintered pellets of compositions in the $(Bi_{1-x}RE_x)FeO_3$ where, RE = La, Nd, Sm, or Gd with $0 \leq x \leq 0.3$ series. Generally for $x \leq 0.1$ in all series, second phase peaks, attributed to Bi or Fe-rich phases, $Bi_2Fe_4O_9$ and $Bi_{25}FeO_{40}$, were routinely observed. However, for $x \geq 0.1$, all peaks in the XRD traces were attributed to perovskite-structured phases. For samples doped with 10% La, Nd or Sm all peaks were indexed according to the *R3c* cell of $BiFeO_3$ [Michel *et al.*, 1969].

For $15\% \leq La \leq 30\%$, $15\% \leq Nd \leq 20\%$ and Sm 15% a new phase appeared whose peaks could be indexed according to an orthorhombic $PbZrO_3$-like structure [Karimi *et al.*, 2009a,

Karimi *et al.*, 2009b]. For Gd-doped compositions, some peaks in ceramics with 7.5% ≤ Gd ≤ 15% may also be attributed to the new $PbZrO_3$-like structure but single phase was not observed at room temperature [Karimi *et al.*, 2009a].

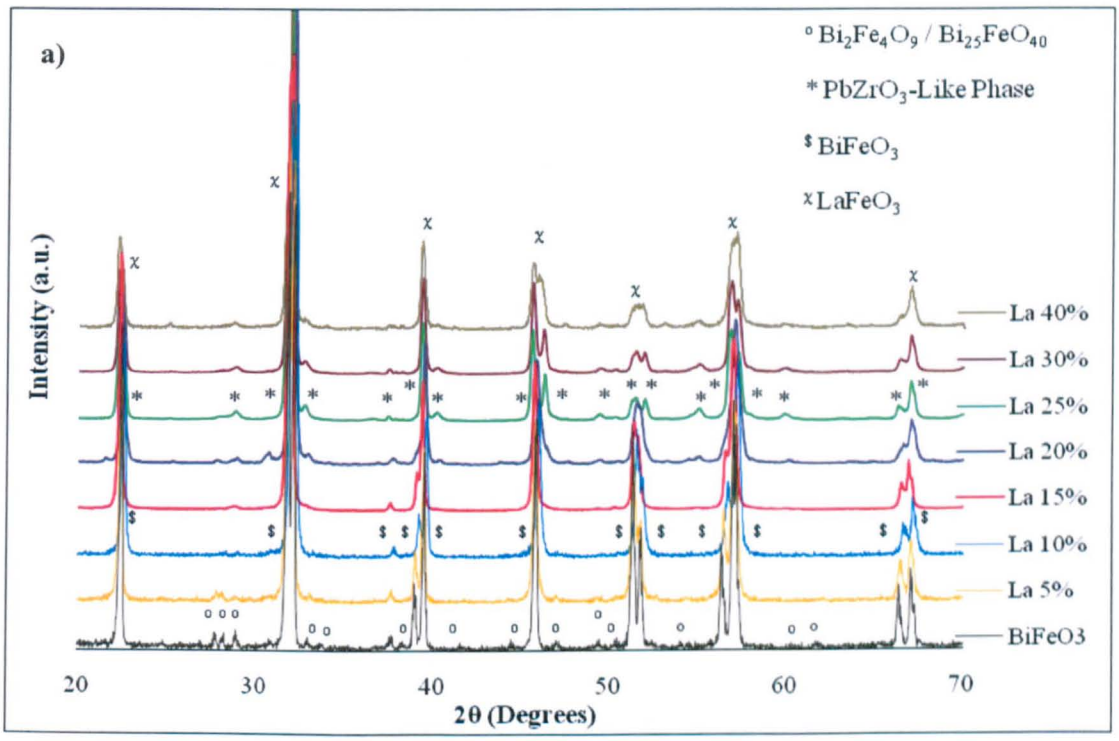

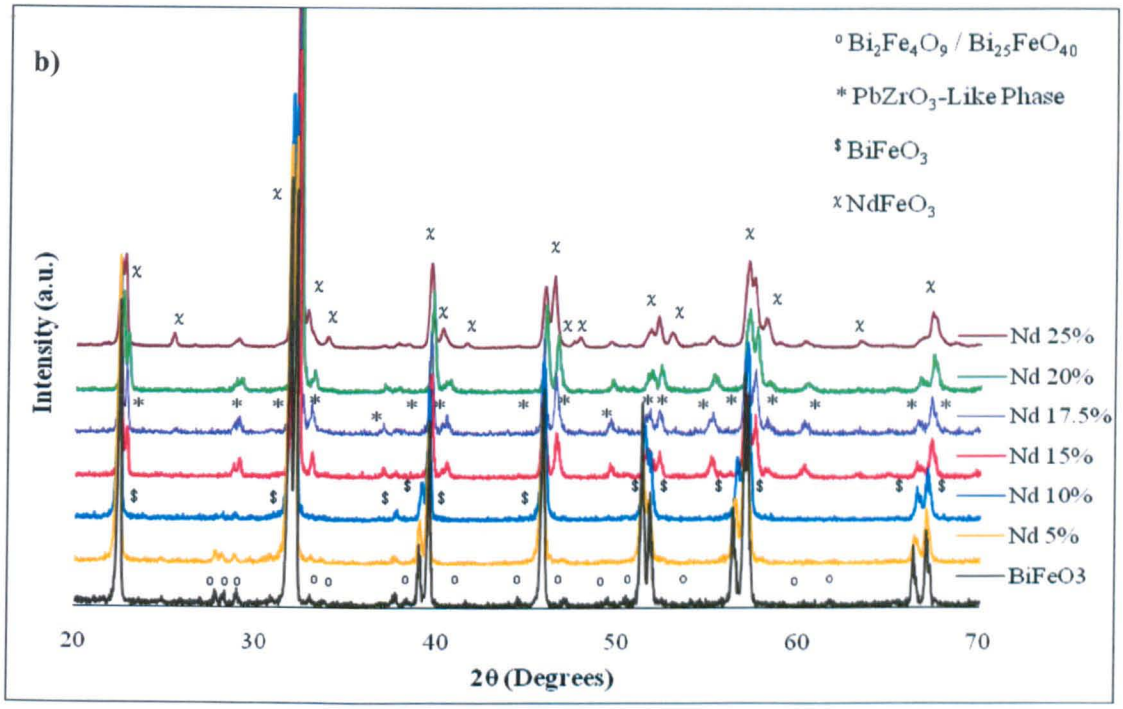
b)
° $Bi_2Fe_4O_9$ / $Bi_{25}FeO_{40}$
* $PbZrO_3$-Like Phase
$ $BiFeO_3$
x $NdFeO_3$
Intensity (a.u.)
Nd 25%
Nd 20%
Nd 17.5%
Nd 15%
Nd 10%
Nd 5%
BiFeO3
20
30
40
50
60
70
2θ (Degrees)

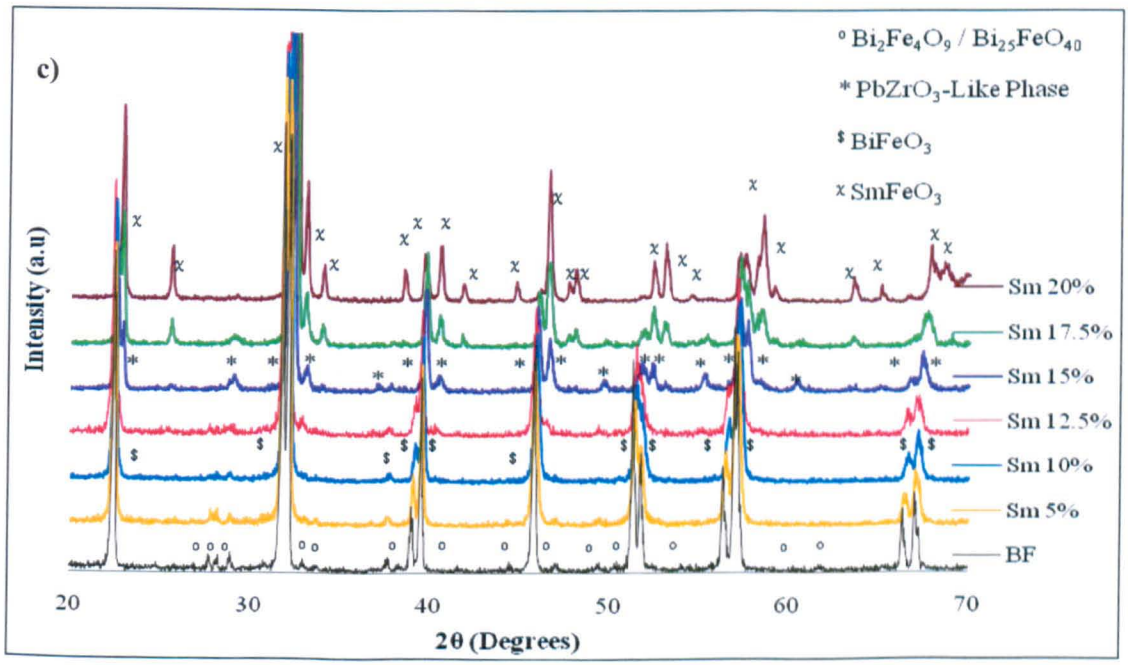
c)
° $Bi_2Fe_4O_9$ / $Bi_{25}FeO_{40}$
* $PbZrO_3$-Like Phase
$ $BiFeO_3$
x $SmFeO_3$
Intensity (a.u)
Sm 20%
Sm 17.5%
Sm 15%
Sm 12.5%
Sm 10%
Sm 5%
BF
20
30
40
50
60
70
2θ (Degrees)

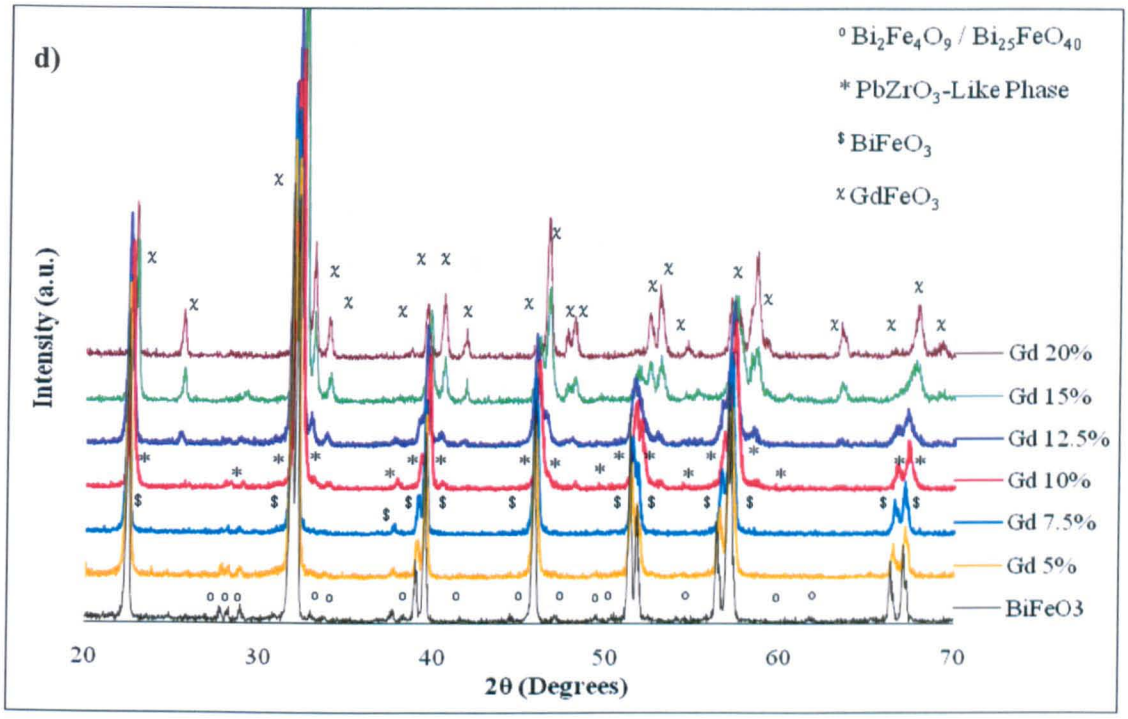

Figure 5.1.3. XRD traces of crushed pellets with compositions $(Bi_{1-x}RE_x)FeO_3$ where RE = a) La, b) Nd, c) Sm and d) Gd. First presented in [Karimi *et al.*, 2009a].

A direct comparison of the new $PbZrO_3$-like structure with the XRD trace of $PbZrO_3$ is shown in Figure 5.1.4a. The traces do not overlap since the fundamental pseudocubic lattice of $PbZrO_3$ (~ 4.1 Å) is much larger than that of $BiFeO_3$ (~ 3.9 Å) but the strong similarity of the traces indicates that the distortions away from cubic in the new phase are virtually identical to those of $PbZrO_3$. A preliminary Rietveld refinement using a $PbZrO_3$ cell adapted for 20% Nd-doped $BiFeO_3$ is shown in Figure 5.1.4b. Although there are some minor differences, the provisional *R* factor R_{wp}= 4.57, confirms that the structure is best described by *Pbam* symmetry of $PbZrO_3$ cell which has the approximate dimensions, $\sqrt{2}a_c$, $2\sqrt{2}a_c$, $2a_c$ where a_c is the pseudocubic lattice parameter [Karimi *et al.*, 2009b].

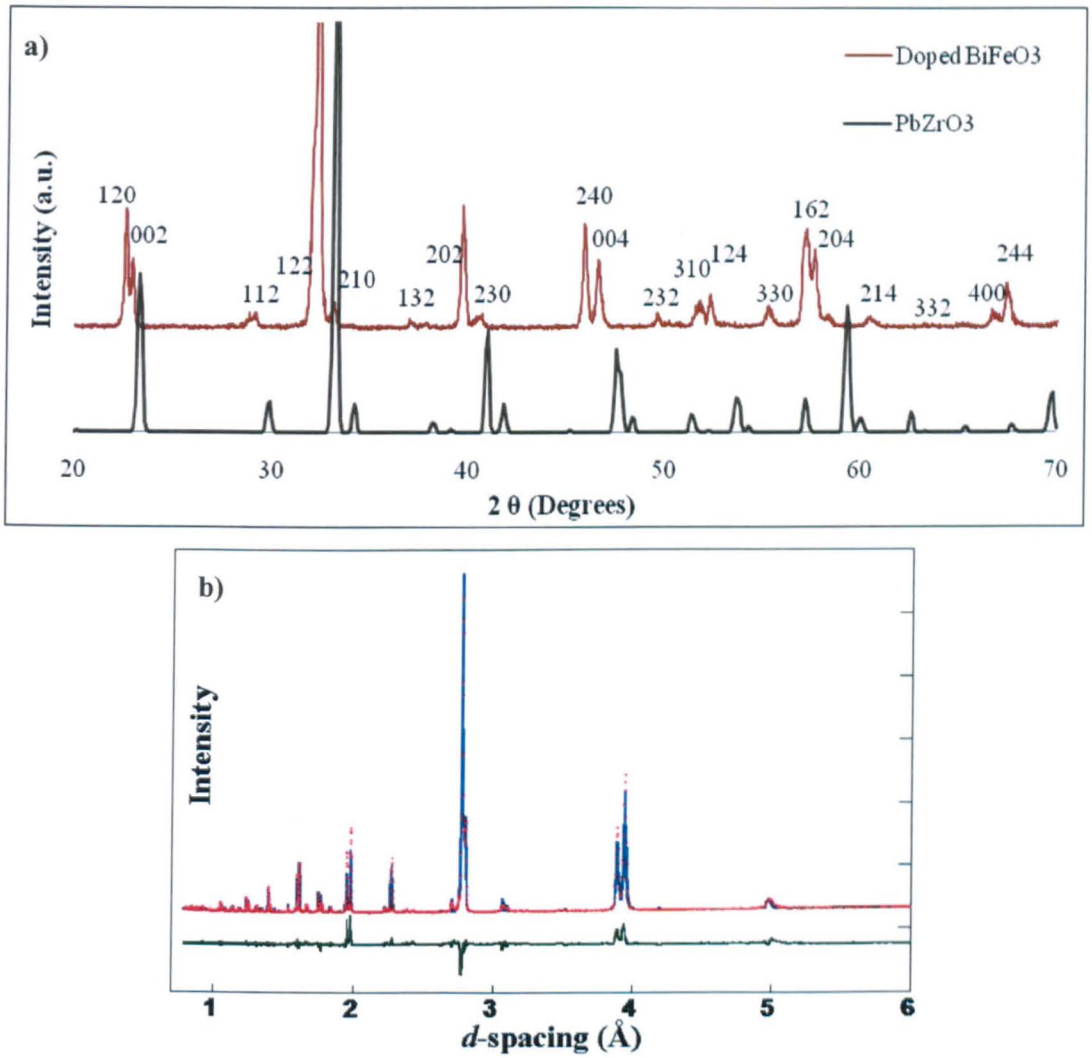

Figure 5.1.4. a) Comparison of experimental trace of 20%Nd-doped $BiFeO_3$ with $PbZrO_3$ and b) experimental and calculated XRD profiles of the same composition. The calculated profile was obtained by Rietveld refinements of a $PbZrO_3$-like structural model. First presented in [Karimi *et al.*, 2009b].

For Gd ≥ 15%, Sm ≥ 20%, Nd ≥ 25% and La ≥ 40%, major peaks were indexed according to the orthoferrite structure with *Pnma* symmetry and approximate cell dimensions of $\sqrt{2}a_c$,

$\sqrt{2}a_c$, $2a_c$. Some peaks attributed to the new $PbZrO_3$-like phase were sometimes present, particularly near the phase boundary, suggesting heterogeneity in the distribution of the RE ions.

5.1.3. Unit Cell Volume and Density

The space group symmetry, densities, relative densities and unit cell volume of all compositions are shown in Table 5.1.1.

The unit cell volume generally decreases with increasing the RE dopant concentration. For Nd (r_{Nd} = 1.27Å) doped compositions, Figure 5.1.5, the *R3c/Pbam* and *Pbam/Pnma* (orthoferrite / $PbZrO_3$-like) phase boundaries are well defined with abrupt changes in the unit cell volume. Within the *R3c* and *Pbam* phase fields, Vegard's law is obeyed and the unit cell volume decreases linearly with increasing dopant concentration [Vegard, 1921]. For larger RE ions such as La (r_{La} =*1.32 Å*), the decrease in unit cell volume is less pronounced whereas for smaller RE ions (r_{Gd} =*1.2 Å*) the volume decreases sharply with increasing dopant concentration.

All samples exhibited a relative density of $\geq$ 95% theoretical. However, some inaccuracies in the measurement of density are anticipated near the phase boundaries since the compositions are typically mixed phase.

Table 5.1.1. Unit cell volume and measured, calculated and relative density of pellets.

RE	%	Structure	Volume ($Å^3$)	Measured ($kg.cm^{-3}$)	Calculated ($kg.cm^{-3}$)	Relative %
La	0	*R3c*	62.31	7.93(20)	8.33(4)	95.1(3)
	5	*R3c*	62.17	7.92(26)	8.26(3)	95.8(6)
	10	*R3c*	61.53	7.88(48)	8.25(3)	95.5(7)
	15	*R3c*	61.24	7.86(45)	8.19(5)	96.0(4)
	20	*Pbam*	60.38	7.81(26)	8.18(4)	96.0(4)
	25	*Pbam*	60.32	7.82(56)	8.12(2)	95.9(4)
	30	*Pbam*	59.79	7.93(28)	8.10(2)	97.4(2)
	40	*Pnma*	59.29	7.80(40)	7.97(4)	97.7(6)
Nd	5	*R3c*	62.06	8.21(34)	8.28(6)	99.0(5)
	10	*R3c*	61.81	8.12(44)	8.22(3)	98.4(5)
	15	*Pbam*	61.33	8.10(28)	8.20(2)	98.7(3)
	17.5	*Pbam*	61.25	7.93(41)	8.17(2)	96.6(7)
	20	*Pbam*	61.05	8.00(22)	8.15(2)	98.0(3)
	25	*Pnma*	60.57	7.89(26)	8.13(5)	97.1(3)
Sm	5	*R3c*	62.05	7.86(26)	8.29(4)	94.9(6)
	10	*R3c*	61.70	7.96(48)	8.25(4)	96.3(6)
	12.5	*R3c*	62.03	8.13(38)	8.17(4)	99.4(2)
	15	*Pbam*	61.00	7.98(32)	8.27(3)	96.4(1)
	17.5	*Pnma*	59.42	8.20(48)	8.45(1)	97.0(3)
	20	*Pnma*	59.07	8.09(28)	8.46(3)	95.6(1)
Gd	5	*R3c*	61.97	7.90(44)	8.31(2)	95.0(4)
	7.5	*R3c*	61.05	8.15(35)	8.40(5)	97.0(4)
	10	*Pbam*	60.91	7.98(44)	8.38(5)	95.1(4)
	12.5	*Pbam*	61.17	8.09(20)	8.31(3)	97.2(7)
	15	*Pnma*	60.93	8.21(26)	831(2)	98.7(2)
	20	*Pnma*	60.82	8.00(26)	8.25(2)	96.8(5)

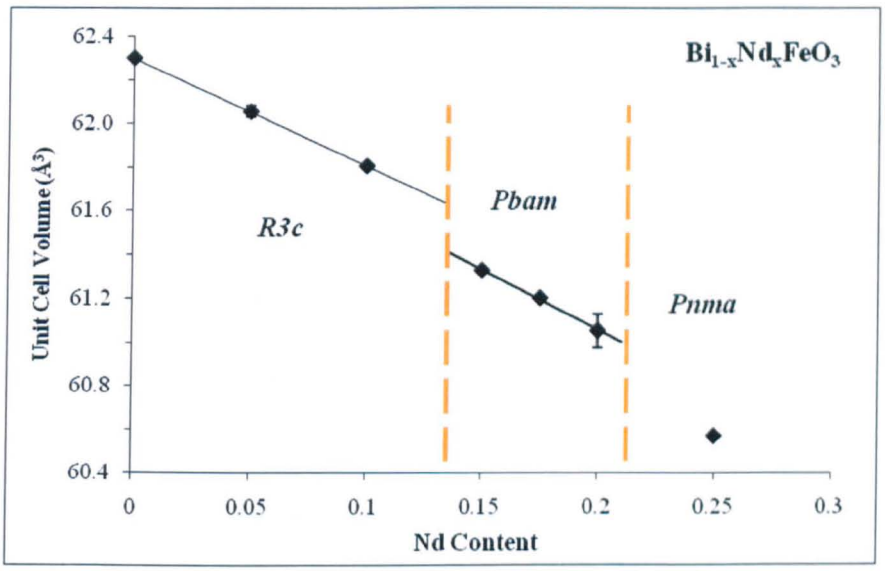

Figure 5.1.5. Unit cell volume of Nd-doped $BiFeO_3$ as the structure transforms from rhombohedral *R3c* to orthorhombic $PbZrO_3$-like *Pbam* to orthorhombic orthoferrite *Pnma*.

5.2. SEM

5.2.1. Undoped $BiFeO_3$

SEM images from polished and fractured surfaces of pellets revealed that the matrix grain size was ~20 μm for undoped $BiFeO_3$, Figure 5.2.1, with smaller grains of a Bi-rich phase whose greater density and composition are illustrated by back scattered imaging and EDS analysis, respectively, Figure 5.2.2. In back scattered images, Figure 5.2.1, the brightness is directly related to the electron density, hence Fe- and Bi-rich phases appear qualitatively brighter and darker with respect to the matrix perovskite. Compositional differences between regions of different contrast is confirmed by the EDS data, Figure 5.2.2. In all samples, the observed porosity was consistent with > 95% theoretical density.

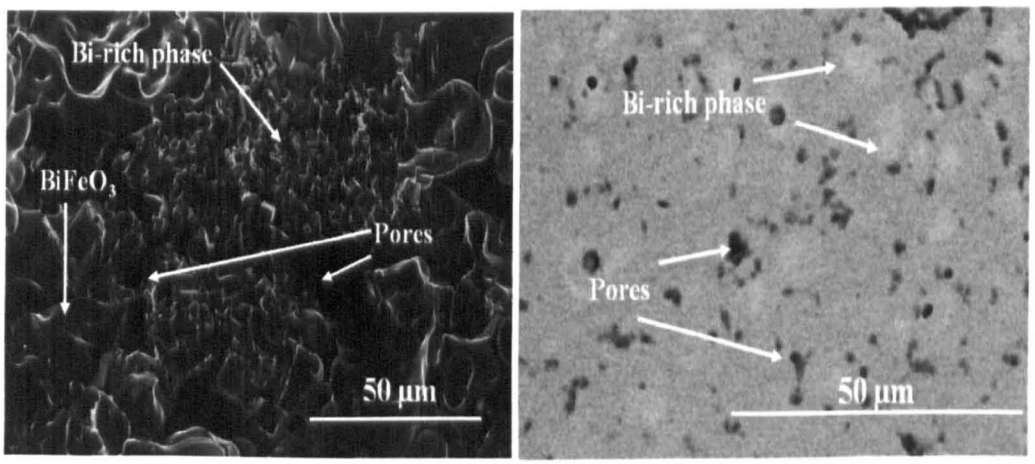

Figure 5.2.1. SEM images of $BiFeO_3$ showing the main perovskite phase and a Bi-rich second phase. Some pores are arrowed in the images.

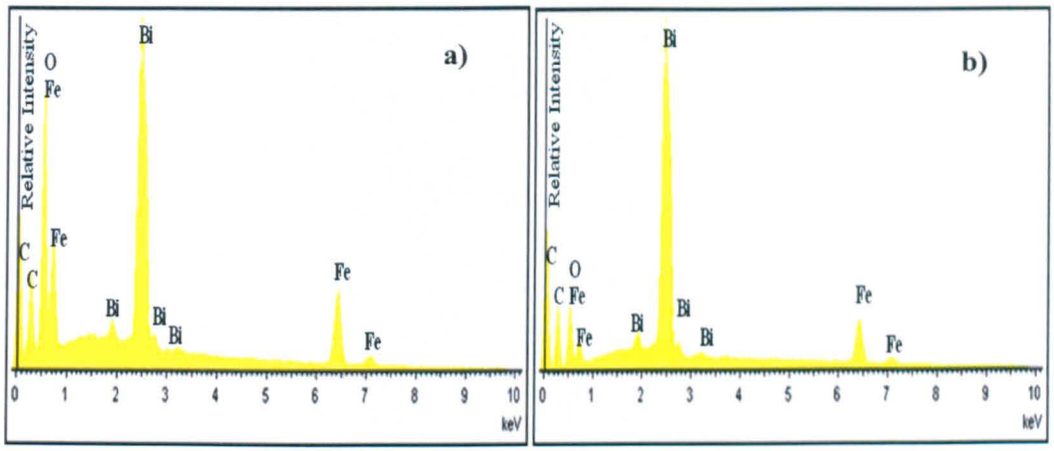

Figure 5.2.2. EDS traces from a) $BiFeO_3$ and b) Bi-rich phases in undoped samples.

5.2.2. La-doped $BiFeO_3$

For 5% La doped $BiFeO_3$, Bi-rich secondary phases gathered mainly at the grain boundaries, often decorating the fracture surface. Consistent with the XRD results, the second phase largely disappeared in samples with ≥ 10% La, Figure 5.2.3. However, there was considerable evidence of inhomogeneity in the distribution of La with La-rich and La-deficient (Bi-rich) regions observed in all samples with ≥ 10% La, Figure 5.2.4. The heterogeneous distribution of La is reflected in the XRD traces from these compositions which do not index readily as a single phase, *R3c*, $PbZrO_3$-like or orthoferrite, as composition increases across the nominal phase boundaries.

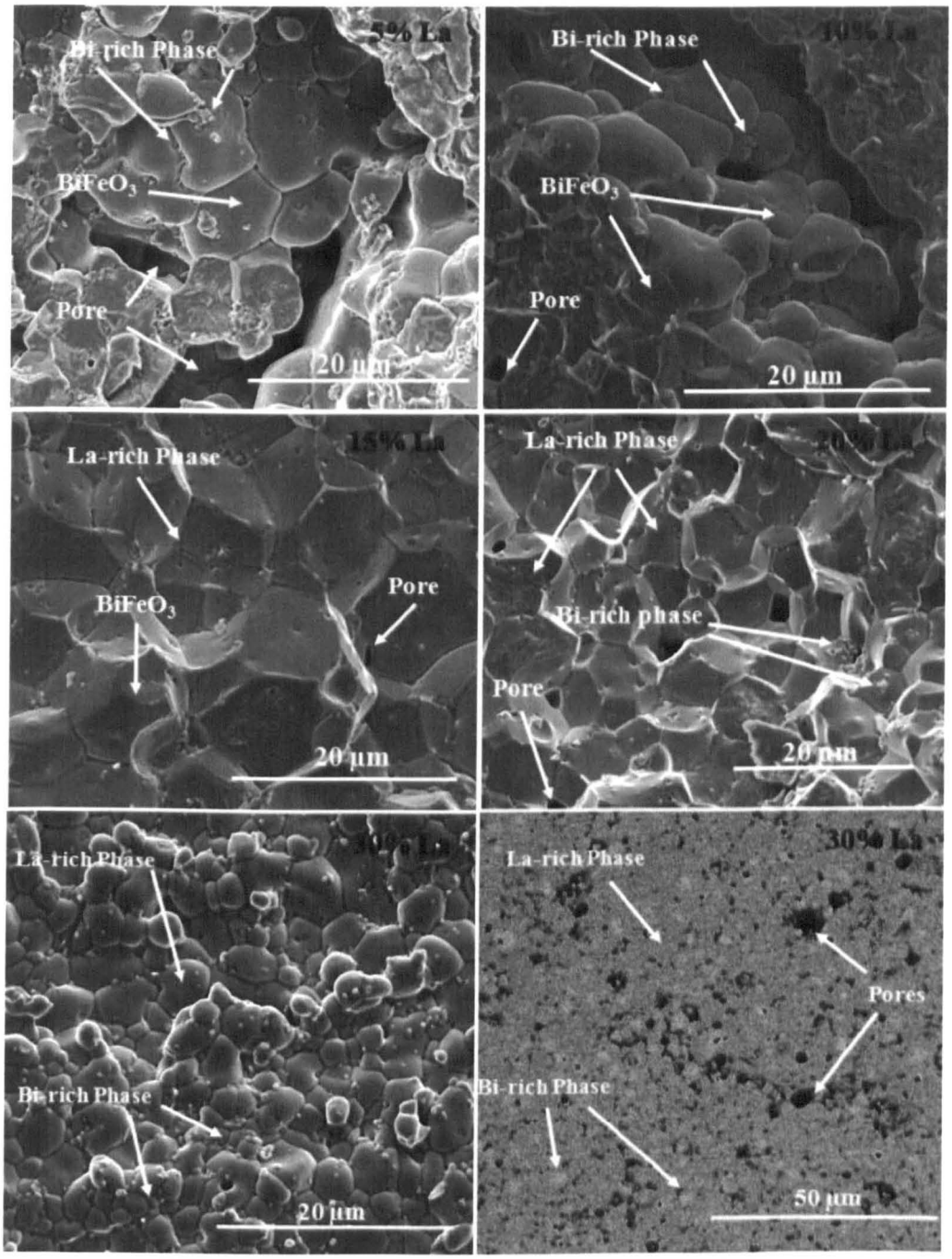

Figure 5.2.3. SEM images of samples of $BiFeO_3$ doped with 5-30% La with different phases present.

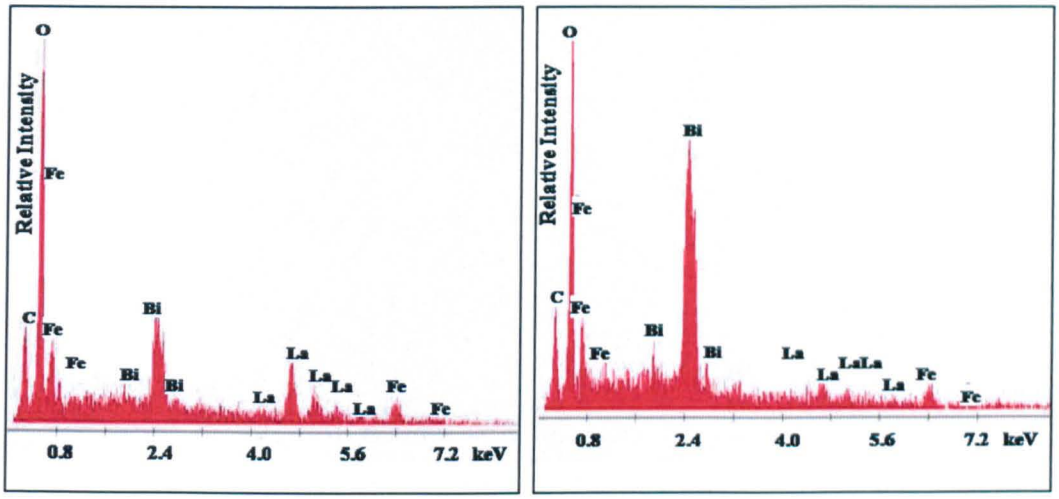

Figure 5.2.4. EDS traces from different regions on the surface of 20% La doped $BiFeO_3$ showing La-rich and Bi-rich (La-deficient) regions.

5.2.3. Nd-doped $BiFeO_3$

Similar to La-doped $BiFeO_3$, Nd-doped compositions exhibited single phase traces by XRD only for $\geq$ 10% Nd. The images for 5 and 10 % Nd are similar to those of equivalent composition in the La-doped series and the reader is referred to Figure 5.2.3. For compositions doped with 15% Nd, small crystals of a Bi-rich phase was observed between the grains of the main phase, Figure 5.2.5. The volume fraction of this phase however, was presumed to be below the detection limit of in-house XRD and corresponding peaks were not observed in traces from this sample.

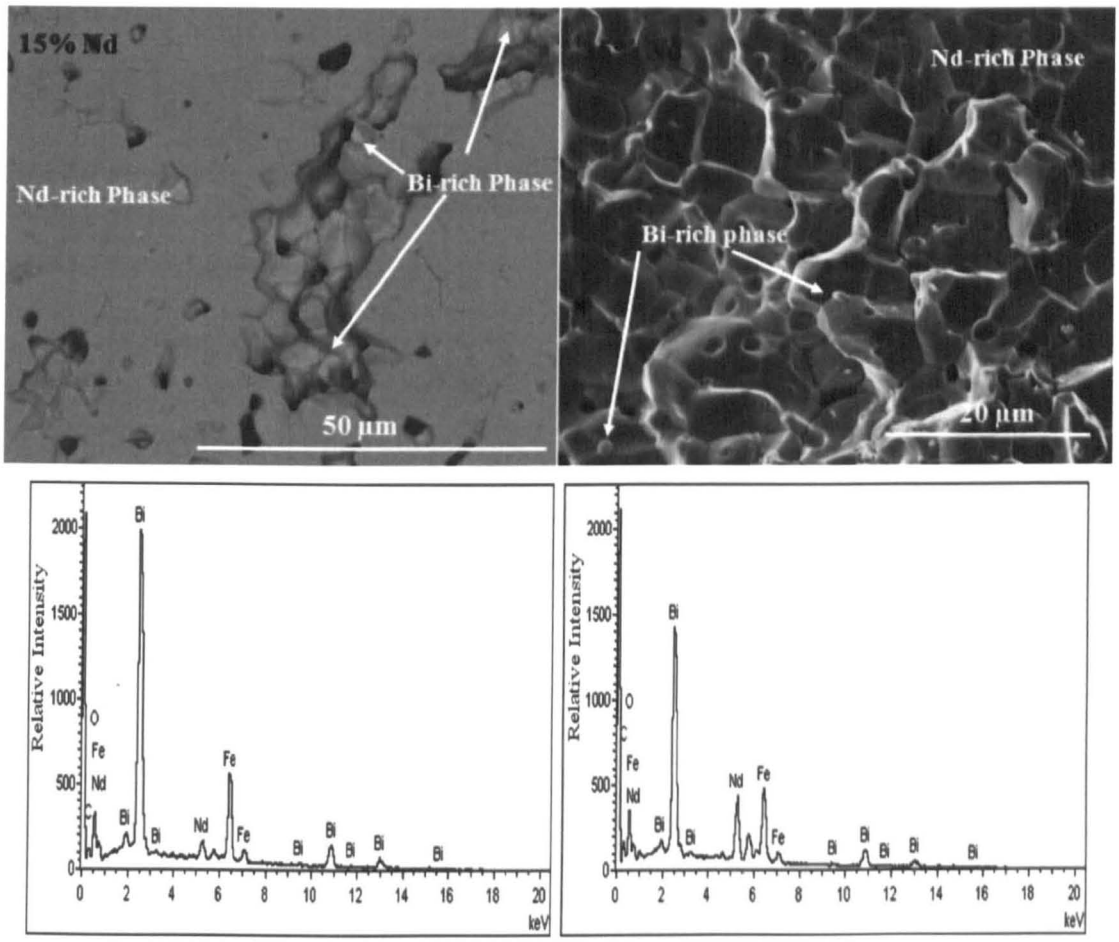

Figure 5.2.5. SEM images and EDS traces of 15% Nd-doped $BiFeO_3$ showing the main phase and a Bi-rich secondary phase.

For compositions doped with 20% Nd, Bi-rich secondary phases are absent but Nd-rich phases are observed, Figure 5.2.6. The arrowed regions are presumably small particles of unreacted Nd_2O_3 which decorate the grain boundaries of the main perovskite phase. The volume fraction of this phase is low and presumed to be below the detection limit of in-house XRD.

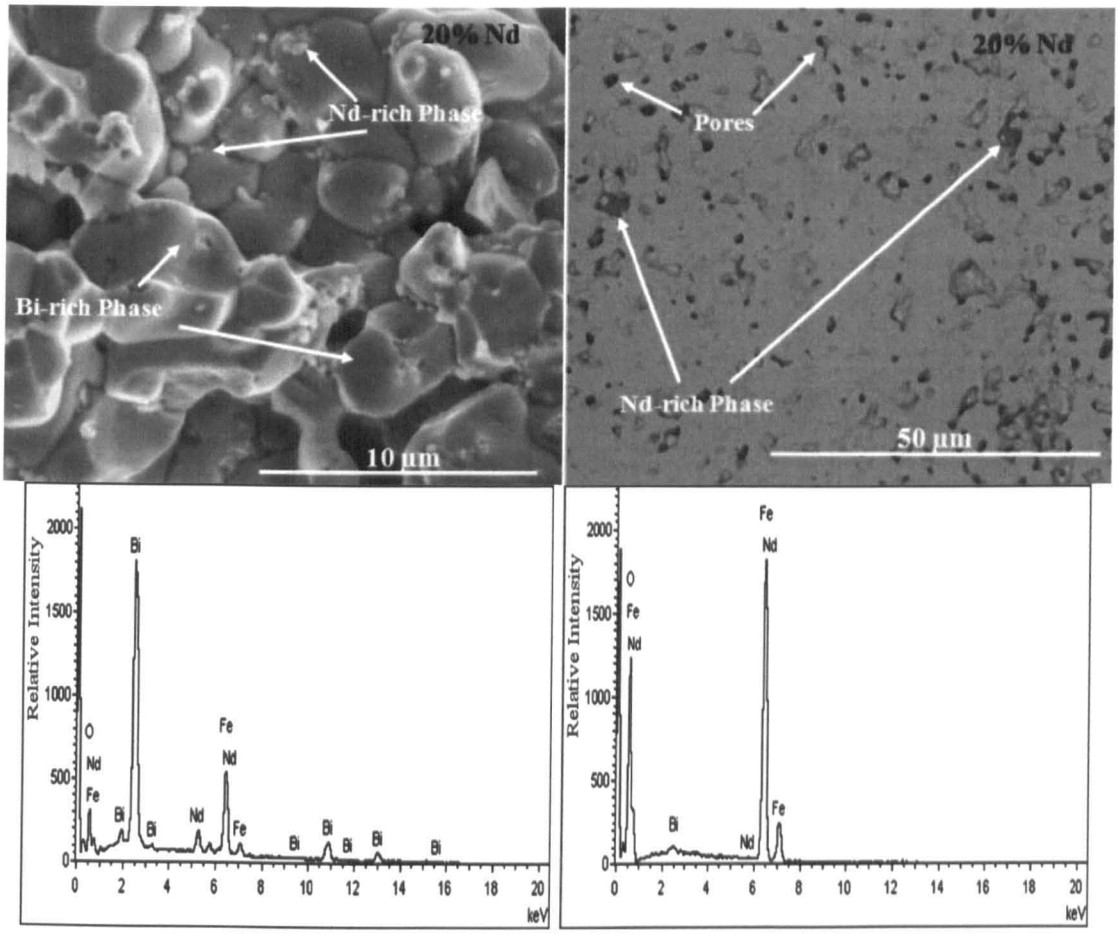

Figure 5.2.6. SEM images and EDS traces of 20% Nd-doped $BiFeO_3$ showing the main phase and a Nd-rich secondary phase.

5.2.4. Sm-doped $BiFeO_3$

For compositions with 5% Sm, a Bi-rich second phase is readily observed which dramaticaly decreases in volume as Sm concentration increases to 10%, Figure 5.2.7. For higher concentrations only small isolated grains of second phases typically at the grain boundaries of the matrix phase were observed. The volume fraction of such phases is small and well below the detection limit of in-house XRD. Figure 5.2.8 shows the EDS traces of the main phase in the 12.5% Sm sample and the Sm-rich secondary phase.

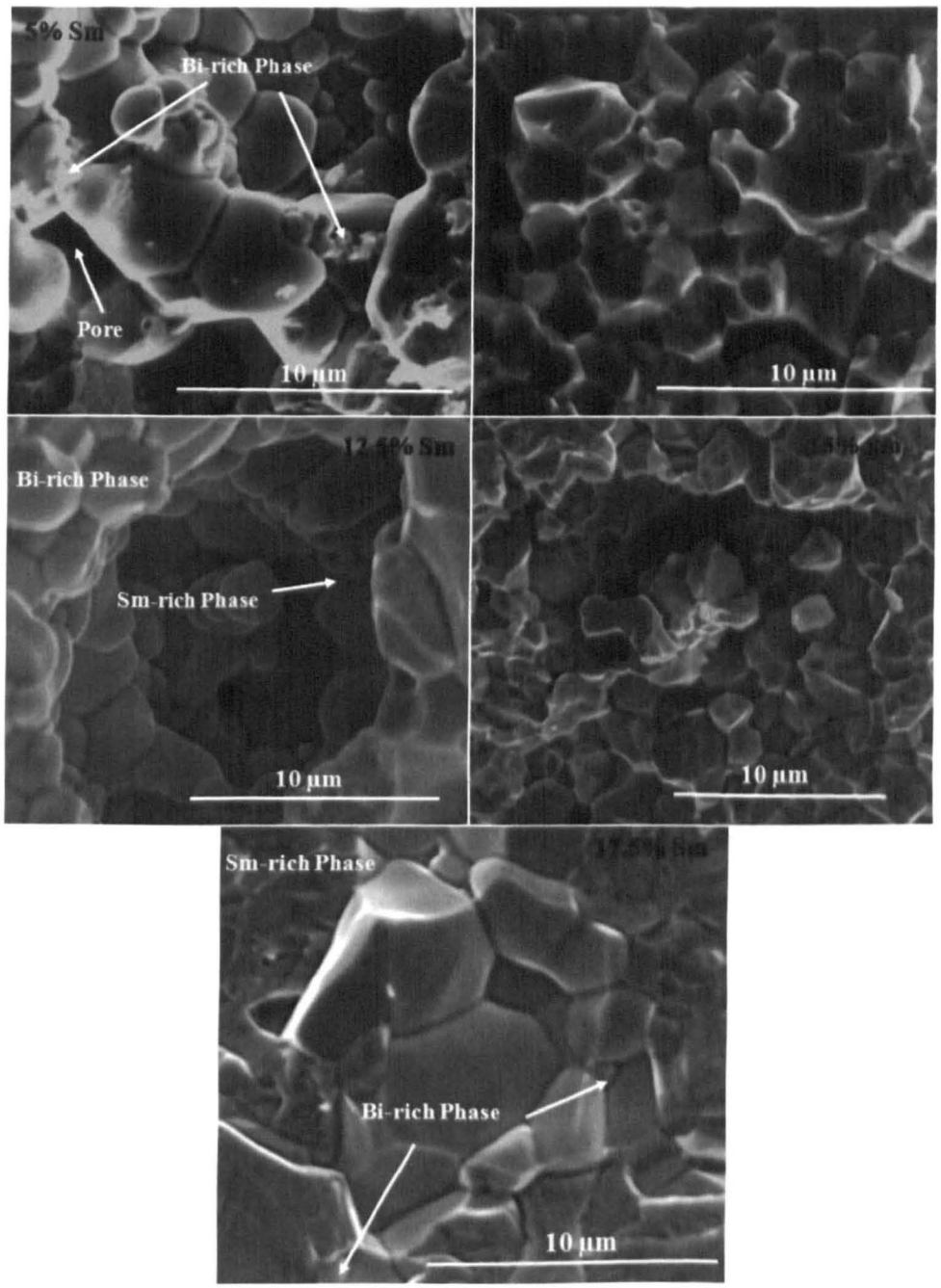

Figure 5.2.7. SEM images of Sm-doped $BiFeO_3$ with the main features arrowed in the images.

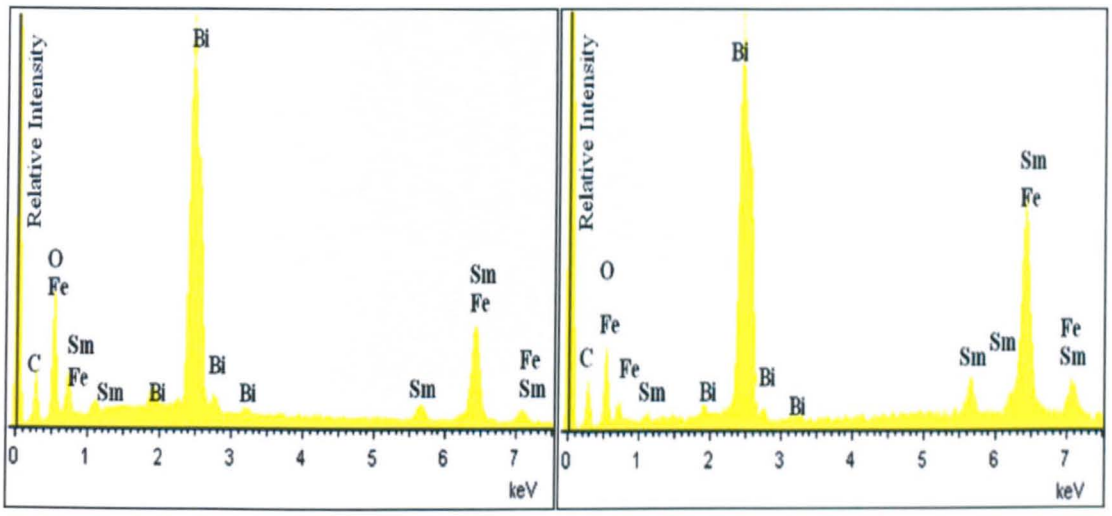

Figure 5.2.8. EDS traces of 12.5% Sm-doped $BiFeO_3$ from the matrix phase and Sm-rich phase.

5.2.5. Gd-doped $BiFeO_3$

For Gd-doped compositions, phase assemblage and homogeneity were difficult to optimise and XRD indicates that unlike, e.g. the Nd and Sm doped, at no point were single phase ceramics obtained, Figure 5.2.9 and 5.2.10. For compositions with 5% Gd, Figure 5.2.9, Bi-rich and Fe-rich grains were observed which presumably correspond to $Bi_{25}FeO_{40}$ and $Bi_2Fe_4O_9$, respectively. Moreover, unlike e.g. Nd and Sm doped compositions, second phases were were routinely observed for higher concentration, Figure 5.2.10.

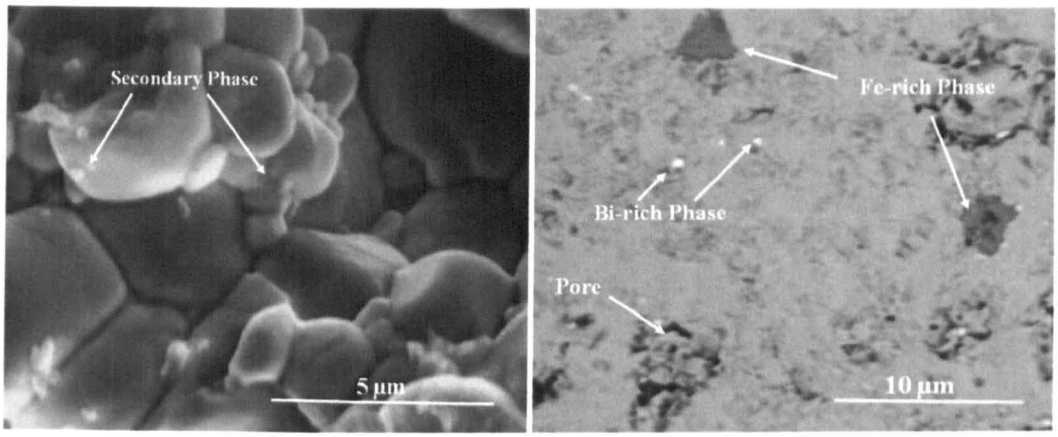

Figure 5.2.9. SEM images of 5% Gd-doped $BiFeO_3$ with the main features arrowed in the images.

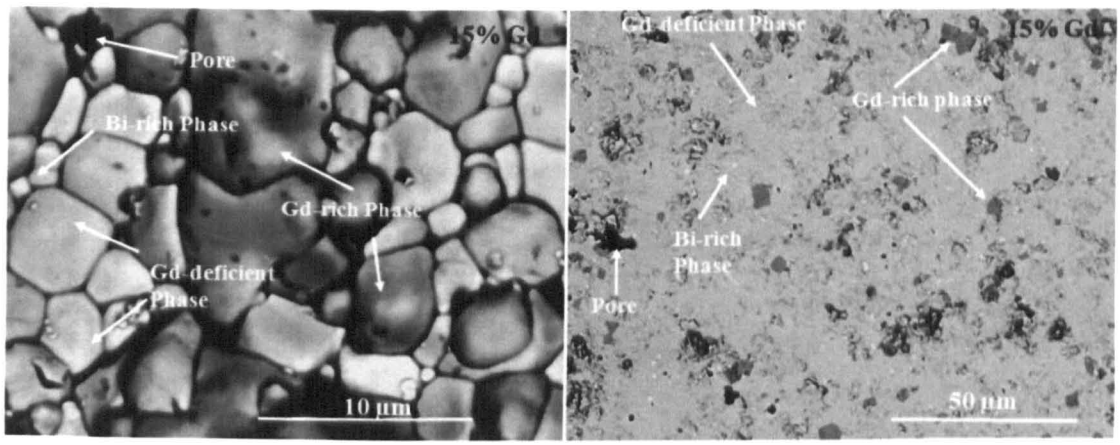

Figure 5.2.10. Back Scattered SEM images of 15% Gd-doped $BiFeO_3$ with the main features arrowed in the images.

5.3. Differential Scaning Calorimetry (DSC)

To further investigate phase transformationsin RE-doped $BiFeO_3$, DSC was performed, Figure 5.3.1. For undoped $BiFeO_3$ a strong peak is observed at 828 °C consistent with the reported ferroelectric T_C. However, a weak anomally is also observed at ~750 °C. The origin of this peak is unknown and it may indicate a further structural phase transition in undoped $BiFeO_3$ or it may be related to a second phase. For samples with 5, 10 and 15% La and Nd, peaks attributed to a ferroelectric T_C were observed at 754 °C, 677 °C, 570 °C and 696 °C, 518 °C, 325 °C respectively, while for compositions with >15% dopant, there are no further sharp anomalies. Changes in the gradient of the DSC curves were, however, apparent at lower temperatures suggesting transitions which occur over a broad temperature interval.

Similar trends are observed in Sm-doped compositions where strong anomalies corresponding to T_C are identified for $\leq$ 10% Sm with only deviations in the gradient of the DSC curve apparent for higher concentrations. This effect is attributed to the heterogeneous distribution of RE cations. The DSC traces of Gd series are markedly different from other series as a result of the heterogeneous distribution of Gd ion and the multiphase assemblage identified in XRD and SEM studies and discussed in section 5.2.5.

Significantly, a broad anomaly is observed in all compositions at ~370 °C, which has been reported as T_N for $BiFeO_3$ [Fischer *et al.*, 1980, Kubel and Schmid, 1990, Sosnowska *et al.*, 1996].

Figure 5.3.2 shows a plot of T_C versus percentage of RE dopant for all compositions. T_C decreases linearly with increasing dopant concentration with the gradient of T_C/composition steeper as the RE ion radius decreases, Table 2.3.

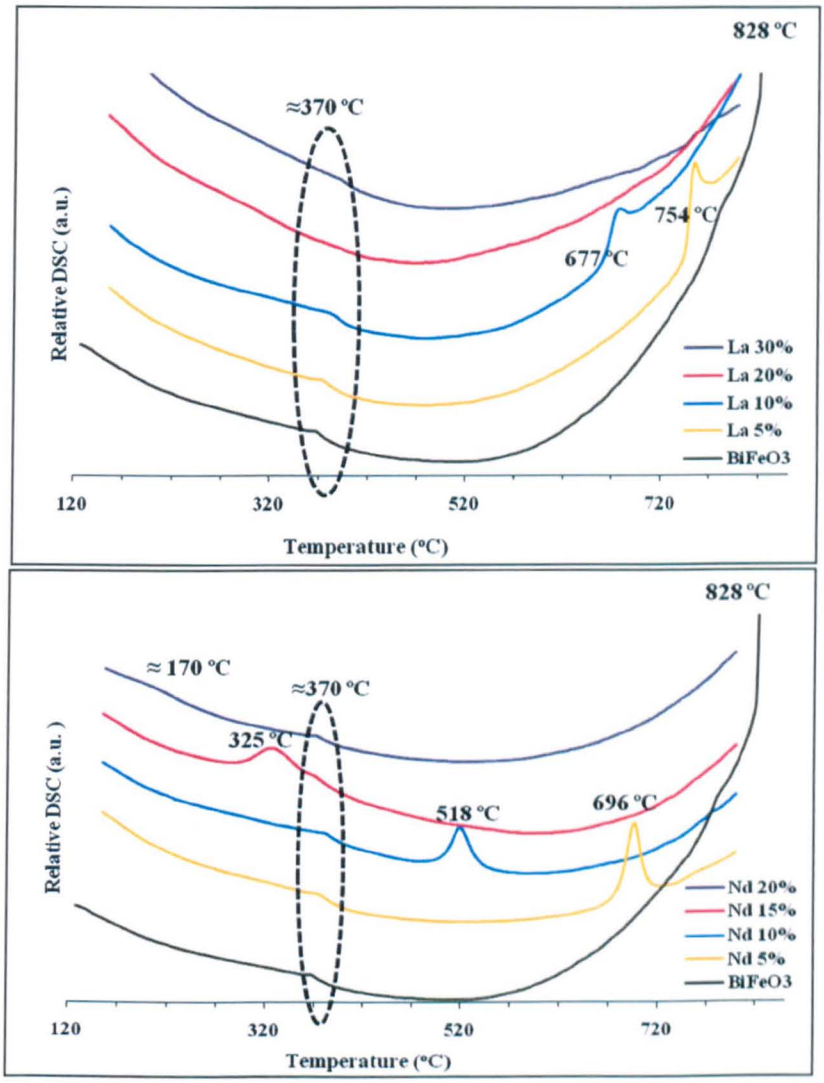
828 °C
≈370 °C
754 °C
677 °C
Relative DSC (a.u.)
La 30%
La 20%
La 10%
La 5%
BiFeO3
120
320
520
720
Temperature (°C)
828 °C
≈ 170 °C
≈370 °C
325 °C
518 °C
696 °C
Relative DSC (a.u.)
Nd 20%
Nd 15%
Nd 10%
Nd 5%
BiFeO3
120
320
520
720
Temperature (°C)

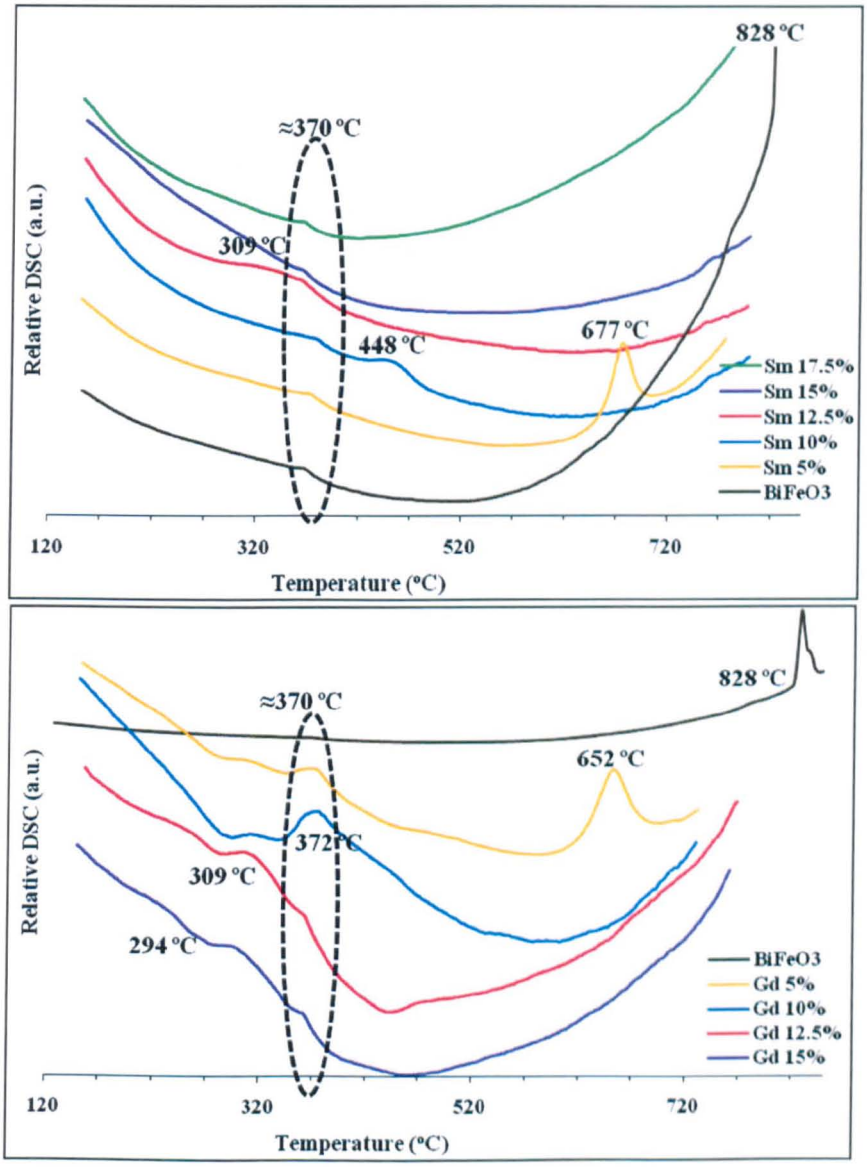

Figure 5.3.1. DSC traces of all compositional series showing T_C and T_N.

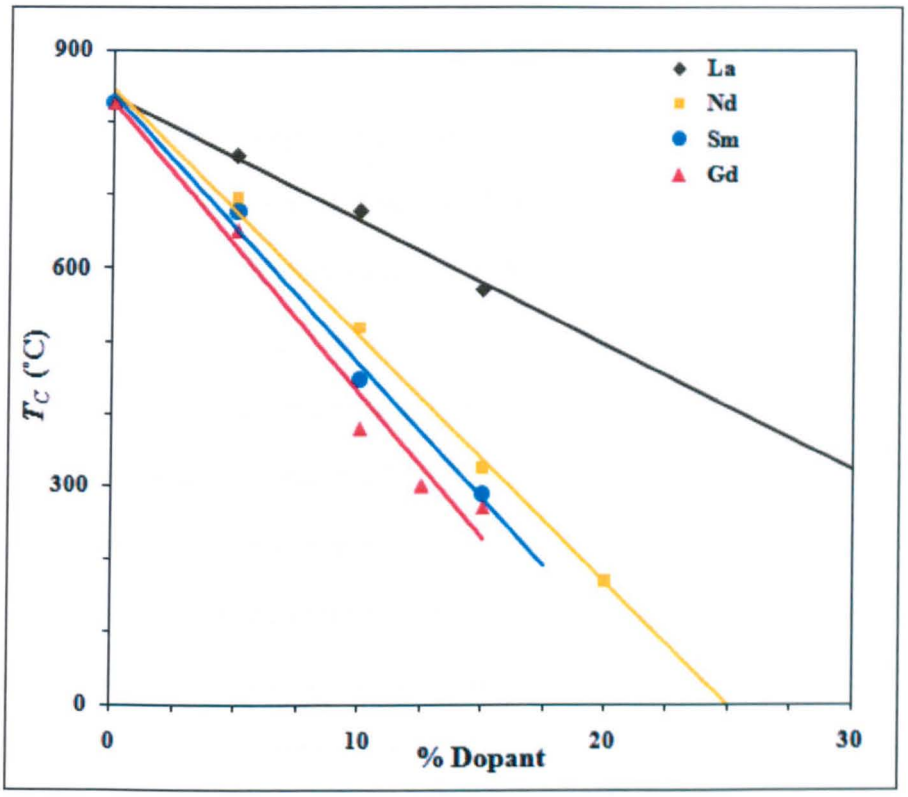

Figure 5.3.2. T_C as a function of the percentage of RE dopant.

5.4. TEM

Transmission electron microscopy was performed on $BiFeO_3$ and RE-doped compositions to characterise the structural and microstructural changes as a function of concentration. The pseudo-cubic zone axes diffraction patterns $<100>_p$, $<110>_p$ and $<111>_p$ were routinely obtained together with bright and dark field images of the domain structures. These zone axes are often used to illustrate structural distortions from the simple cubic cell in perovskites [Reaney, 1996, Woodward and Reaney, 2005].

Superstructure reflections along major zone axes for several well known tilt systems are listed in Table 5.4.1. According to the rules for electron diffraction described by Woodward and Reaney [Woodward and Reaney, 2005] based on the original Glazer paper [Glazer, 1972], $½\{ooo\}_p$ superstructure reflections are expected to appear for $BiFeO_3$ with *R3c* space group and $a^-a^-a^-$ tilt system in 6 out of 12 $<110>_p$ zone axes whereas for $PbZrO_3$ with (a^0b^-b) and orthoferrite-structured $(a^-a^-c^+)$ ceramics, $½\{ooo\}_p$ reflections are present in 10 of the 12 $<110>_p$ zone axes. Additionally, for the orthoferrite phase, the remaining 2 out of 12 $<110>_p$ zones contain $½\{eeo\}_p$ reflections. For the $<001>_p$ zone axes of the orthoferrite phase, 4 of the 6 contain $½\{ooe\}_p$ and 2 out of 6 $½\{eeo\}_p$ reflections while all 8 $<111>_p$ zone axes contain reflections at $½\{ooe\}_p$ positions. Based on these precepts electron diffraction patterns where used to study further the tilt systems of phases within RE-doped $BiFeO_3$ ceramics.

Table 5.4.1. Superstructure reflections along major zone axes for several tilt systems.

Zone Axis	$a^0a^0c^-$	$a^0b^-b^-$	$a^-a^-a^-$	$a^-b^-b^-$	$a^0b^-c^-$	$a^-b^-c^-$	$a^0b^-c^+$ *	$a^-a^-c^+$ *	$a^-b^-c^+$ *
<001> (6)							**½{oee} in 4/6 ½{ooe} in 2/6**	**½{oee} in 4/6 ½{ooe} in 2/6**	**½{oee} in 4/6 ½{ooe} in 2/6**
<110> (12)	**½{ooo} in 8/12 (I≈)**	**½{ooo} in 10/12 (I≈)**	**½{ooo} in 6/12 (I≈)**	**½{ooo} in 10/12 (I≠)**	**½{ooo} in 12/12 (I≠)**	**½{ooo} in 12/12 (I≠)**	**½{ooo} in 8/12 (I≈) ½{oee} in 2/12**	**½{ooo} in 10/12 (I≈) ½{oee} in 2/12**	**½{ooo} in 12/12 (I≠) ½{oee} in 2/12**
<111> (8)							**½{ooe} in 8/8**	**½{ooe} in 8/8**	**½{ooe} in 8/8**

* indicates systems in which anti-parallel A-site displacements are expected.

I≈ indicates that the intensity of the superlattice reflections are constrained to be equal in all zones.

I≠ indicates when the intensities are not constrained to be equal by symmetry.

A more comprehensive list can be found in the reference by [Woodward and Reaney, 2005].

5.4.1. The rhombohedral, $BiFeO_3$ Structure

Figure 5.4.1a illustrates a typical non-180° domain wall arising from the ferroelectric/ferroelastic distortion of the lattice. Figure 4.1b shows a triple points between the grain boundaries of undoped $BiFeO_3$. Figures 4.1c is a dark field image of a grain in a sample of $BiFeO_3$ doped with 10% Nd obtained under two beam conditions utilising a $½\{ooo\}_p$ reflection. The planar defects are anti-phase boundaries which arise where regions of antiphase tilt impinge out of phase. Dark field imaging using a superlattice reflection reveals the antiphase boundary because the structure intensity factors that give rise to contrast in the ordered regions are absent where domains impinge. Thus, antiphase boundaries appear distinctly black against the bright ordered matrix in two beam dark field superlattice images [Williams and Carter, 2009].

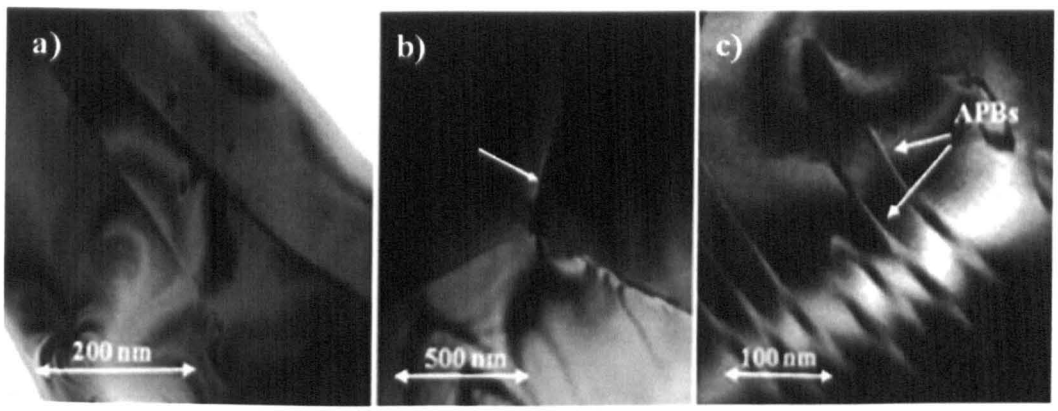

Figure 5.4.1. a) Bright field images of $BiFeO_3$ samples showing featureless grains and b) a junction of three grain boundaries and c) dark field image obtained with the electron beam approximately parallel with $<110>_p$, utilising a $½\{ooo\}_p$ superstrlattice reflection under two beam conditions. First presented in [Karimi *et al.*, 2009a].

Figures 5.4.2 shows zone axis electron diffraction patterns for $BiFeO_3$. $½\{ooo\}_p$ superstructure reflections, that arise from antiphase rotation of the octahedra around the $[111]_p$ axis (Table 5.4.1), are present in some but not all $<110>_p$ zone axes. No other superstructure reflections were observed which is consistent with an $a^-a^-a^-$ tilts system [Woodward, 2004]. Similar electron diffraction patterns could be obtained from all compositions with $x \leq 0.1$ as illustrated in Figure 5.4.3 for La doped $BiFeO_3$ and Figure 5.4.4 for Sm doped $BiFeO_3$. Figure 5.4.4 additionally shows the domain structure and domain variance of the *R3c* phase in the $<110>_p$ directions.

When the high temperature phase transforms to the low temperature structure the allowed domains state are given by the number and type of lost symmetry elements. The domain state is a group theoretical concept which indicates the allowed symmetry operators and combinations thereof which can be applied on any given domain so that it may be made coincident with the one adjacent [Woodward and Reaney, 2005]. In real ceramics, the domain state is only partially manifested as a domain structure in which only the lowest energy domain configurations are likely to be observed. In a cell doubling transition such as that associated with the onset of octahedral tilting, one key aspect of the domain structure is the presence of variance between domains in the appearance of the allowed superstructure reflections. The reflections conditions for *R3c* are such that only 6 out of 12 possible $<110>_p$ zones contain superstructure reflections. Therefore statistically only 50% of the domains on average in any given $<110>_p$ zone axes will exhibit superstructure [Woodward and Reaney, 2005]. This variance is illustrated in Figure 5.4.4.

Figure 5.4.5 shows schematic structure of $BiFeO_3$ with the antiphase rotations of FeO_6 octahedra that give rise to the superstructure observed in the electron diffraction patterns shown in Figure 5.4.2 to 5.4.4.

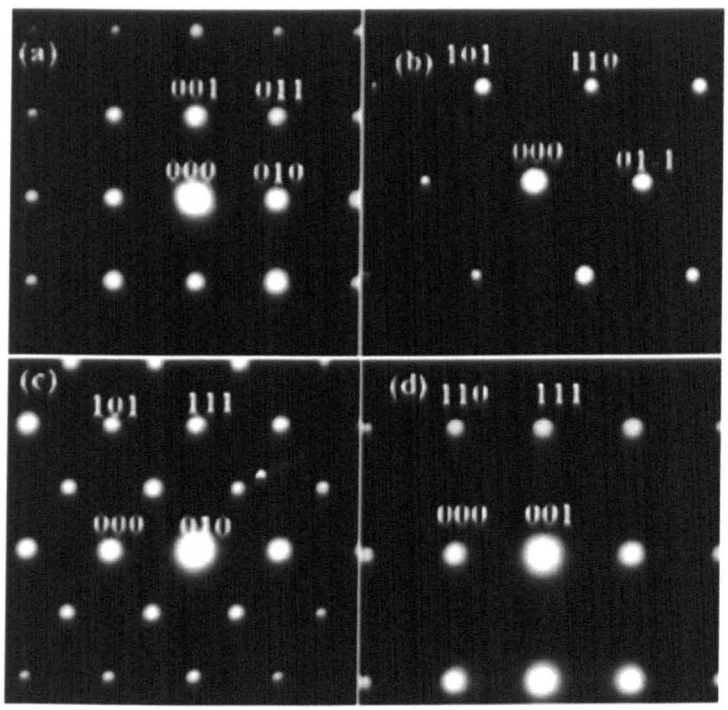

Figure 5.4.2. Electron diffraction patterns from $BiFeO_3$ from a) $<001>_p$, b) $<111>_p$, c) and d) two variants of the $<110>_p$ zone axes. Superstructure reflections at ½{ooo} positions associated with antiphase rotations of the O octahedra are arrowed in (c). First presented in [Karimi *et al.*, 2009b]

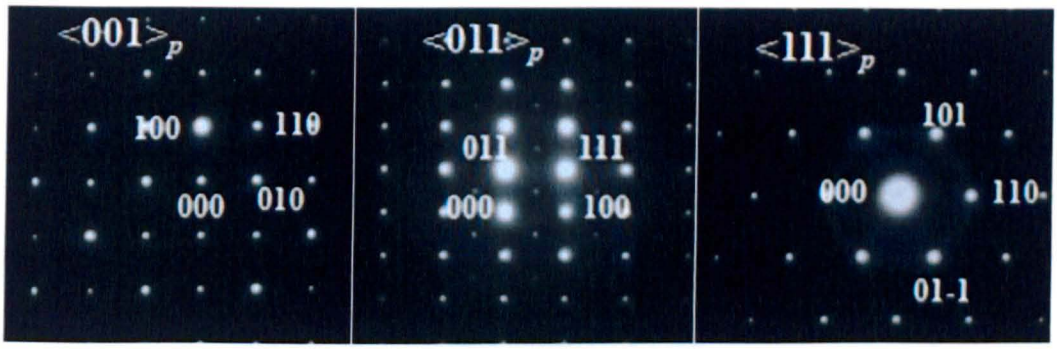

Figure 5.4.3. Electron diffraction patterns from 10% La-doped $BiFeO_3$ from $<001>_p$, $<011>_p$ and $<111>_p$ zone axes. Only superstructure of the type $½\{ooo\}_p$ is observed , consistent with *R3c* symmetry.

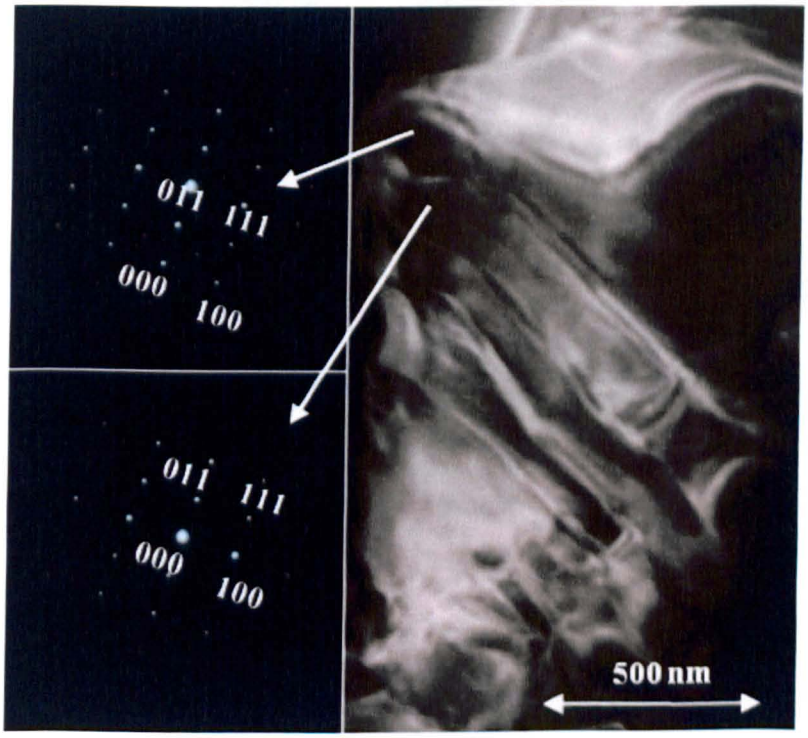

Figure 5.4.4. Electron diffraction patterns of 10% Sm-doped samples showing two variants of $<110>_p$ zone axes taken from two neighbouring grains marked on the image.

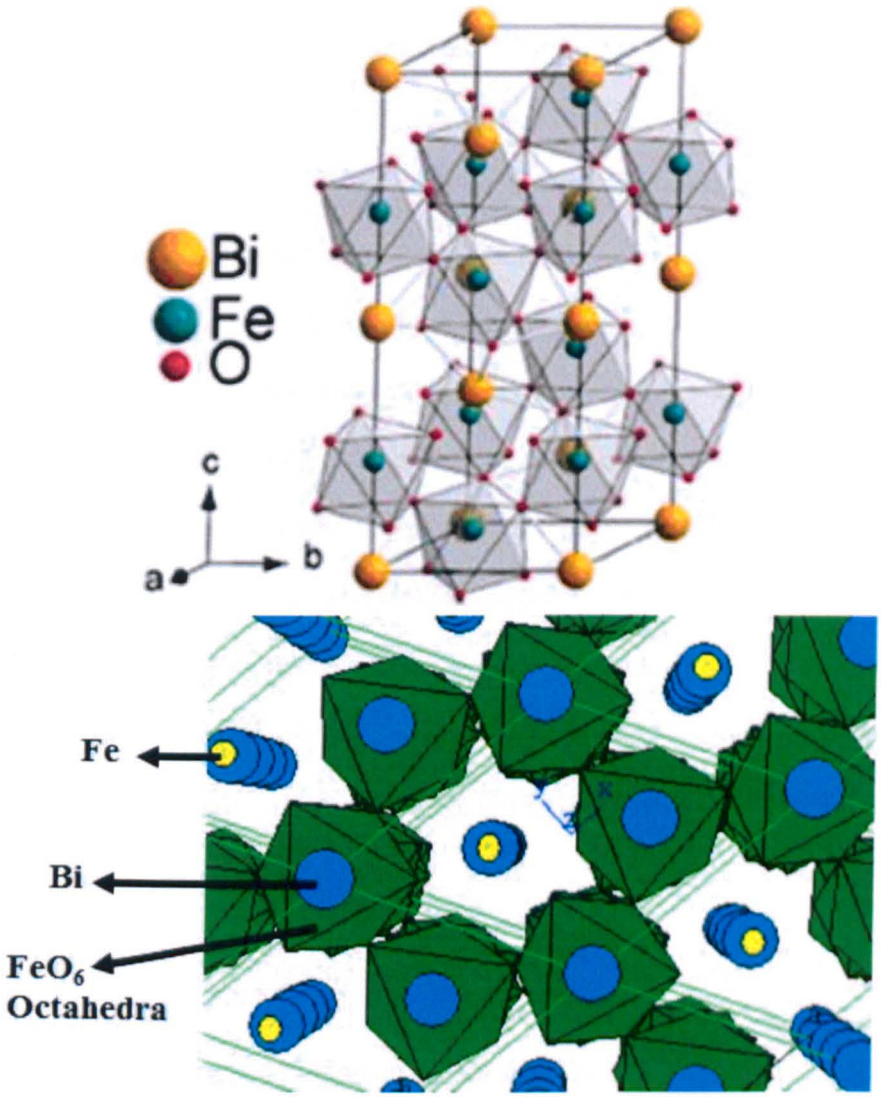

Figure 5.4.5. schematic models of $BiFeO_3$ rhombohedral *R3c* structure.

5.4.2. $PbZrO_3$-like Structure

$PbZrO_3$ is the archetype antiferroelectric perovskite in which the orthorhombic unit cell may be described on a $\sqrt{2}a_c \times 2\sqrt{2}a_c \times 2a_c$ matrix with the c axis coincidental with the fundamental perovskite lattice but with a and b rotated through 45° [Sawaguchi *et al.*, 1951]. The structural distortions within the cell may be envisaged as antipolar displacements of the Pb ions along $[110]/[-1-10]_p$ direction and antiphase rotations of the FeO_6 octahedra described by an $a^-a^-c^0$ tilt system, Figure 5.4.6. The key signature superstructure reflections for $PbZrO_3$ are therefore $\frac{1}{2}\{ooo\}_p$ reflections which appear in e.g. 10 out of 12 $\langle 110\rangle_p$ zone axes and more critically $\frac{1}{4}\{hk0\}_p$ reflections. Note that the reflection condition $h \neq k$ applies to $\frac{1}{4}\{hk0\}_p$, so they are forbidden, e.g. in the $\langle 110\rangle_p$ zone axes where h is constrained to equal k. However, in other zones such as $\langle 111\rangle_p$ and $\langle 001\rangle_p$, the $\frac{1}{4}\{hk0\}_p$ may appear because of double diffraction routes allowed in that direction of the crystal, e.g.

$$(-\tfrac{3}{4}\ \tfrac{1}{4}\ 0) + (100) = (\tfrac{1}{4}\ \tfrac{1}{4}\ 0)$$

The rings of intensity observed in Figure 5.4.6 are artefacts of TEM sample preparations as they arise from the ZrO_2 crystals formed on the surface of the $PbZrO_3$ sample during ion milling [Knudsen, 2002].

Although XRD data are strikingly similar and preliminary refinements give a high 'goodness' of fit to *Pbam* symmetry, electron diffraction patterns indicate some weak structural features that suggest the symmetry and cell dimensions of the $PbZrO_3$-like phase in RE-doped $BiFeO_3$ are different to $PbZrO_3$. Figure 5.4.7 shows a sequence of zone axis

diffraction patterns along major zones obtained from 20% Nd-doped $BiFeO_3$. Identical patterns were obtained for all samples which exhibit the $PbZrO_3$-like structure, according to XRD.

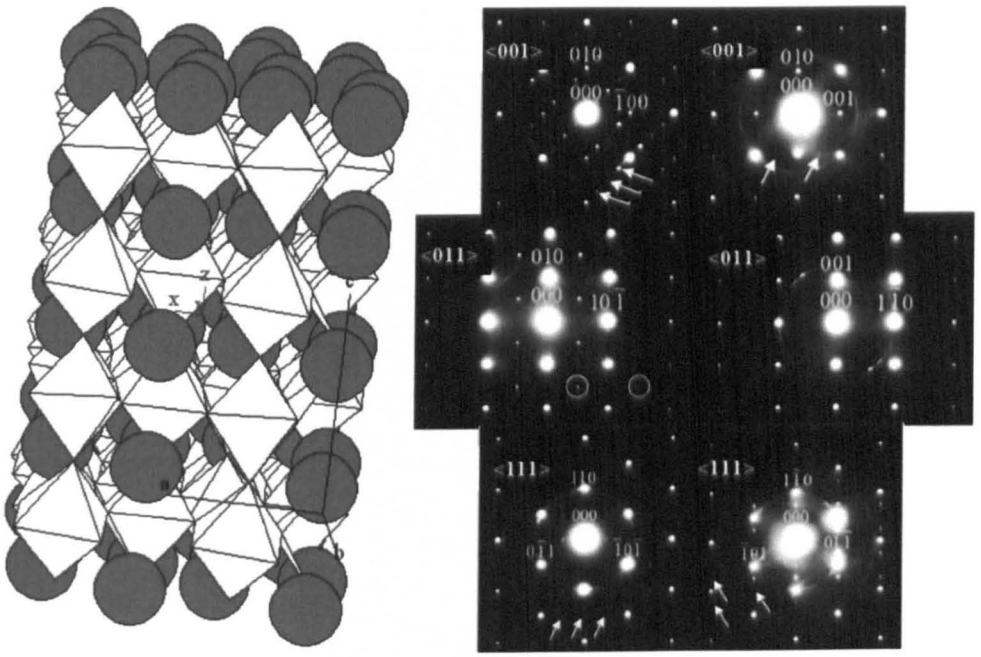

Figure 5.4.6. Structure of $PbZrO_3$ showing Pb ions in antiparallel quadrupling the unit cell and some electron diffraction patterns of PZ showing two variants of $<001>_p$, $<011>_p$ and $<111>_p$ zone axes. Note the presence of $½\{ooo\}_p$ reflections in some $<110>_p$ zones and $1/4\{hk0\}_p$ in some $<111>_p$ and $<001>_p$ [Knudsen, 2002, Reaney *et al.*, 1997].

The ED patterns illustrate that the $PbZrO_3$-like phase is not only quadrupled along one of the $<110>_p$ directions (i.e. a periodicity of $2\sqrt{2}a_c$ as in $PbZrO_3$) giving rise to $¼\{hk0\}_p$ reflections but also along the $<001>_p$, manifested as the appearance of $¼\{00l\}_p$ reflections. Superstructure reflections at $½\{ooo\}_p$ positions associated with anti-phase rotations of the

FeO_6 octahedra were also present as anticipated in some but not all $<110>_p$ zones consistent with a tilt system in which at least two orthogonal axes are tilted with equal magnitude [Woodward and Reaney, 2005].

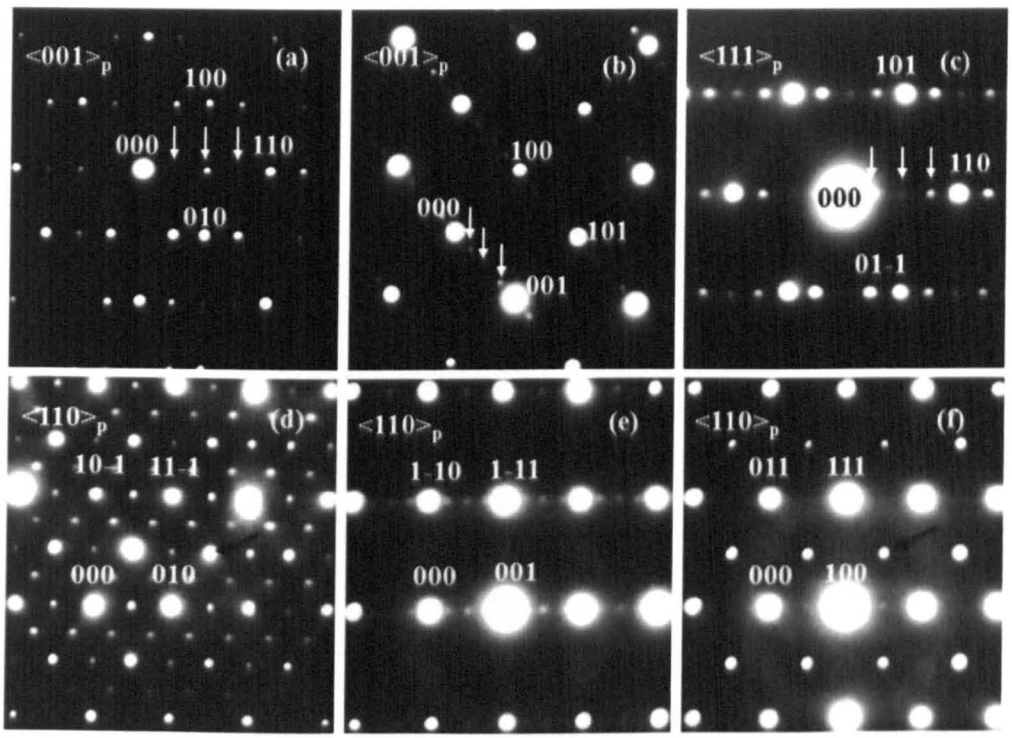

Figure 5.4.7. Electron diffraction patterns from grains of 20% Nd-doped sample where a) and b) are two variants of the $<001>_p$ zone axes, c) is one variant of the $<111>_p$ zone axes and d), e) and f) are three variants of the $<110>_p$ zone axes. *¼(00l)* and *¼(hk0)* are arrowed in a), b) and c) and $½\{hkl\}_p$ reflections are arrowed in d) and f). First presented in [Karimi *et al.*, 2009b].

Figure 5.4.8. is a dark field image of a 20% Nd-doped sample illustrating the ferroelastic domain structure in a grain with the electron beam parallel with $<110>_p$. The image was

obtained using a $\frac{1}{2}\{ooo\}_p$ reflection (ringed). Adjacent to the image are the three domain variants of the pseudocubic $<110>_p$ obtained from each highlighted domain. Figure 5.4.9 is a dark field image of a 15% Nd-doped sample obtained using a $\frac{1}{4}\{hkl\}$ reflection and with the electron beam approximately parallel with a $<110>_p$ zone axis. The image reveals antiphase boundaries that have formed because of the impingement of regions of antipolar order that have nucleated out of phase.

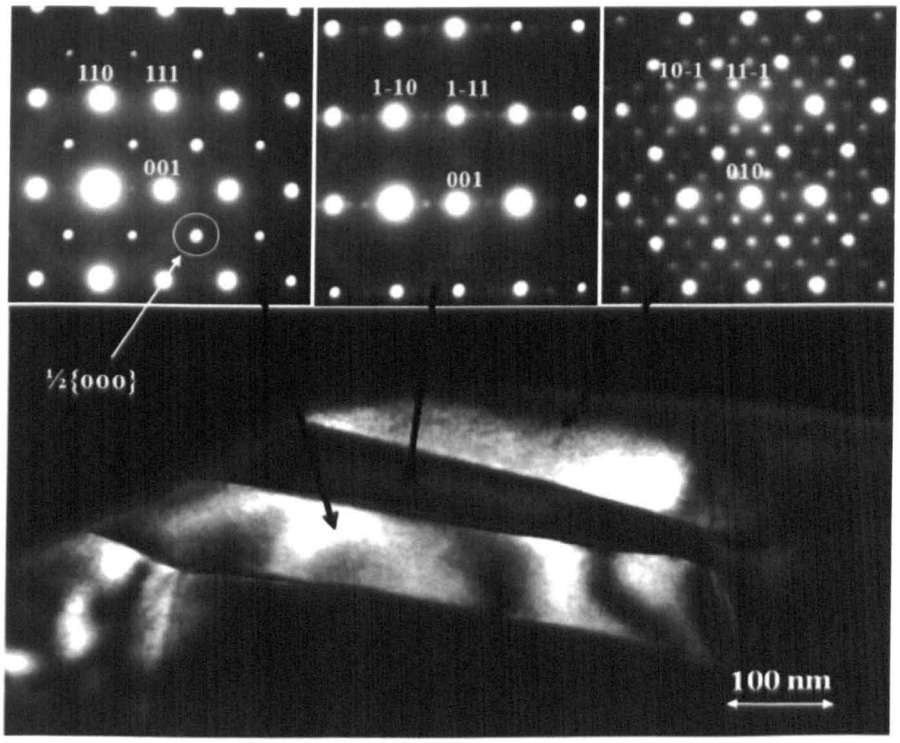

Figure 5.4.8. Domain variance of the pseudocubic $<110>_p$ direction in 20% Nd-doped sample using a $\frac{1}{2}\{ooo\}_p$ superstructure reflection. First presented in [Karimi *et al.*, 2009a].

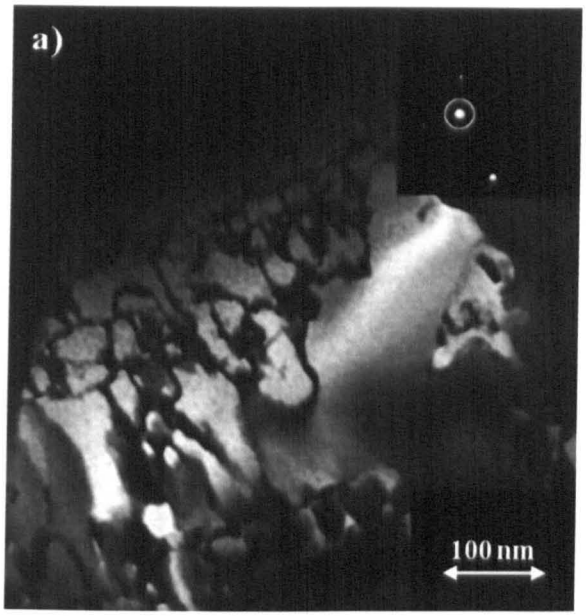

Figure 5.4.9. Dark field image of 15% Nd-doped sample obtained using a $¼\{hkl\}_p$ reflection with electron beam approxiamtely along a $<110>_p$. The image reveals antiphase boundaries associated with regions of antipolar Bi displacements that have nucleated out of phase. Image courtesy of Dr. S. Miao.

Identical electron diffraction patterns for the $PbZrO_3$-like phase in Nd-doped compositions were recorded for La and Sm-doped ceramics. Figures 5.4.10 and 5.4.11 show $<100>_p$ and $<111>_p$ zone axes for the 30% La- and $<100>_p$, $<110>_p$ and $<111>_p$ zone axes for the 15% Sm-doped compositions. However, some grains of the 15% Sm doped composition also revealed superstructure reflections of the type $½\{eeo\}_p$, Figure 5.4.12, which arise from antiparallel cation displacements of the A-sites within systems with mixed in-phase and anti-phase tilting [Glazer, 1972, Woodward and Reaney, 2005]. The most likely explanation is that the superstructure reflections arise from regions of the 15% Sm-doped sample which are orthoferrite structured. Such regions are present due to an inhomogeneous distribution of the

Sm within the sample. The orthoferrite phase has *Pnma* symmetry with an $a^-a^-c^+$ tilt system and thus give rise to the $\frac{1}{2}\{eeo\}_p$ reflections [Woodward and Reaney, 2005].

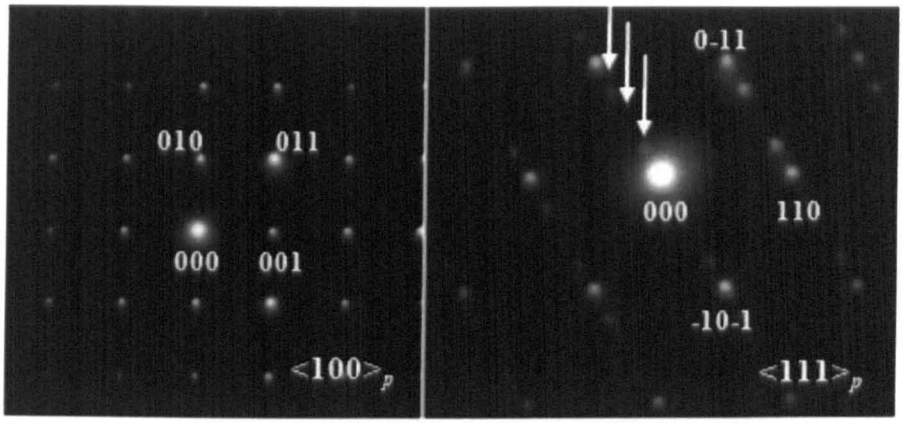

Figure 5.4.10. $<100>_p$ and $<111>_p$ zone axis diffraction pattern from grains in 30% La-doped compositions.

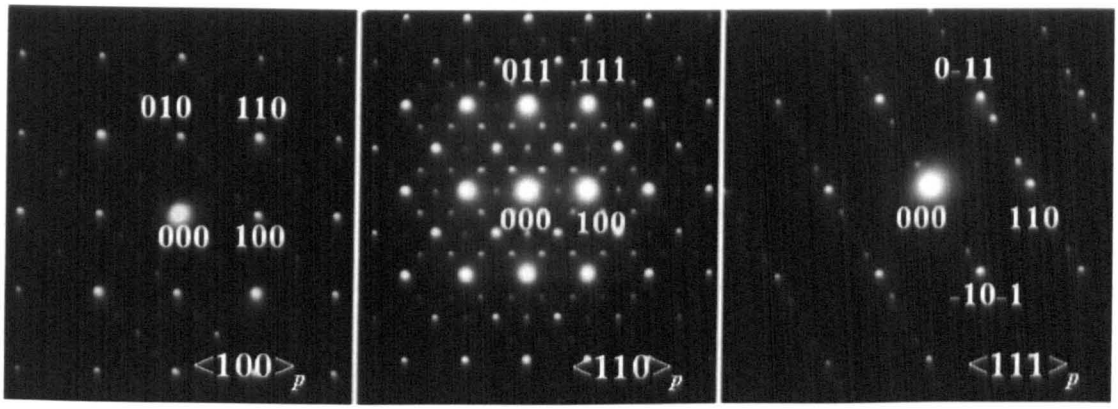

Figure 5.4.11. $<100>_p$, $<110>_p$ and $<111>_p$ zone axes obtained from grains within 15% Sm-doped compositions

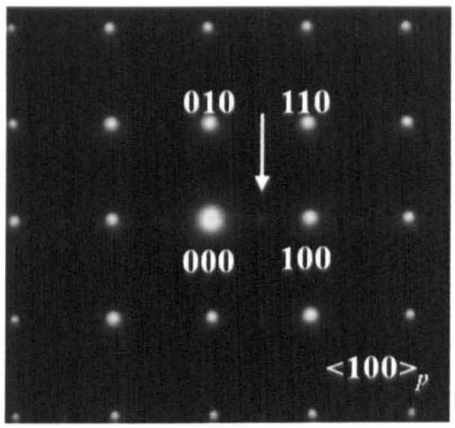

Figure 5.4.12. $<100>_p$ zone axis in 15% Sm-doped compositions showing $½\{eeo\}_p$ superlattice reflections characteristic of the orthoferrite phase.

Figure 5.4.13 shows a bright field image of a region in a 15% Gd-doped sample recorded at room temperature. The grain contains a mixture of $PbZrO_3$-like and orthoferrite phase, consistent with XRD data shown in Figure 5.1.3d. This gives rise to a highly complex domain structure. Inset are $<001>_p$ zones axes from each phase. The quadrupled reflections of the $PbZrO_3$-like phase are arrowed and $½\{eeo\}_p$ reflections of the orthoferrite phase are ringed.

If the electron diffraction patterns are utilised to determine the symmetry of the $PbZrO_3$-like phase, the *0kl: k+l=2n* and *h0l: h=2n* reflection conditions limit the choice of posible space groups. Moreover, the unit cell for $PbZrO_3$ contains 8 formula units (Z=8) with approximate dimensions, $\sqrt{2}a_c, 2\sqrt{2}a_c, 2a_c$ whereas the unit cell dimensions of the $PbZrO_3$-like phase observed in RE-doped $BiFeO_3$ compositions has 16 formula units (Z=16) with approximate dimensions, $\sqrt{2}a_c, 2\sqrt{2}a_c, 4a_c$. The overall symmetry is therefore best described by the *Pnma* space group (No. 62). However, it should be emphasised that the structure is not that of orthoferrite despite possessing the same symmetry. The transition from orthoferrite to

$PbZrO_3$ structure doubles the unit cell along $[001]_p$ and $[110]_p$ directions effectively creating an isomorphic subgroup. Figure 5.4.14 shows a schematic rendering of the $PbZrO_3$-like phase in RE-doped $BiFeO_3$ compositions.

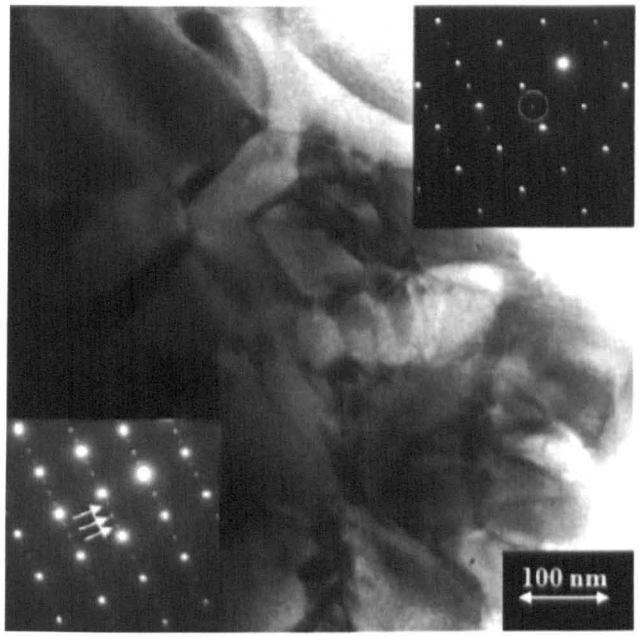

Figure 5.4.13. A bright field image of a region in a 15% Gd-doped sample with the electron diffraction pattern insets of $<001>_p$ zones axes from each phase. The quadrupled reflections of the $PbZrO_3$-like phase are arrowed and $½\{eeo\}_p$ reflections of the orthoferrite phase are ringed. Frist presented by [Karimi *et al.*, 2009a]

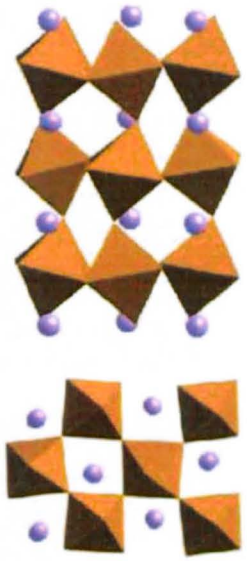

Figure 5.4.14. Schematic rendering of the orthorhombic $PbZrO_3$-like structure with an aproximate unit cell of $\sqrt{2}a_c, 2\sqrt{2}a_c, 4a_c$., reproduced from [Levin, Karimi and co-workers, 2010].

5.4.3. In-situ Electron Diffraction

In-situ electron diffraction was performed on compositions doped with 15 and 20% Nd. Figure 5.4.15 shows two domain variants of the $<001>_p$ zone axis from a single grain obtained at room temperature which reveal superstructure reflections at $¼\{hk0\}_p$ and $¼\{00l\}_p$, respectively. As temperature increases to above 300 °C, $¼\{hk0\}_p$ reflections are replaced by $½\{ooe\}_p$ and the $¼\{00l\}_p$ reflections replaced by $½\{eeo\}_p$ in the $<001>_p$ zone axes. The transition temperature is broadly consistent with the wide peak in the DSC trace of this composition. The appearance of $½\{ooe\}_p$ and $½\{eeo\}_p$ superstructure reflections in the high temperature phase indicates the presence of in-phase tilting in perovskite structured compounds [Glazer, 1972].

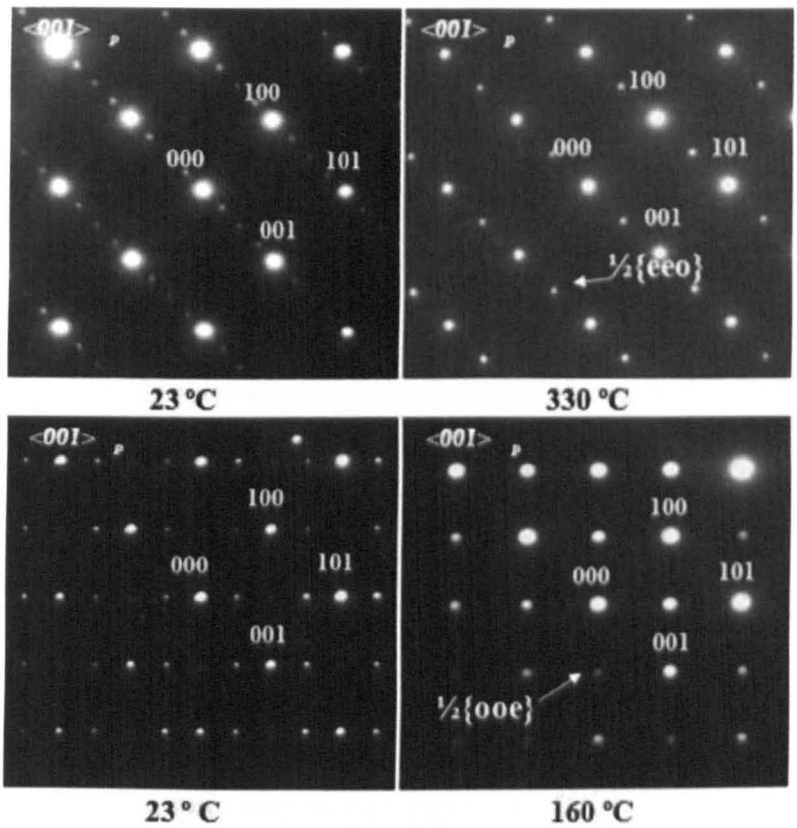

Figure 5.4.15. In-situ electron diffraction performed on the sample with 20% Nd exhibited a reversible transition from the $PbZrO_3$-like quadrupled cell to an $a^-a^-c^+$ tilt system. First presented in [Karimi *et al.*, 2009a].

Similar in-situ studies were also performed on the 15% Nd doped samples, Figure 5.4.16 utilising $<310>_p$ zone axes which enabled simultaneous observation of the $¼\{hk0\}_p$ and $¼\{00l\}_p$ superlattice reflections as a function of increasing temperature. $¼\{hk0\}_p$ reflections disappear at the $PbZrO_3$-like to orthoferrite transition, whereas the $¼\{00l\}_p$-type reflections disappeared at a lower temperature. It may be that these two sets of superlattice reflections arise from different phase transition but further work is required to prove this conclusively.

Further zone axis electron diffraction patterns from the high temperature phase were all consistent with the $a^-a^-c^+$ tilt system of the orthoferrite structure.

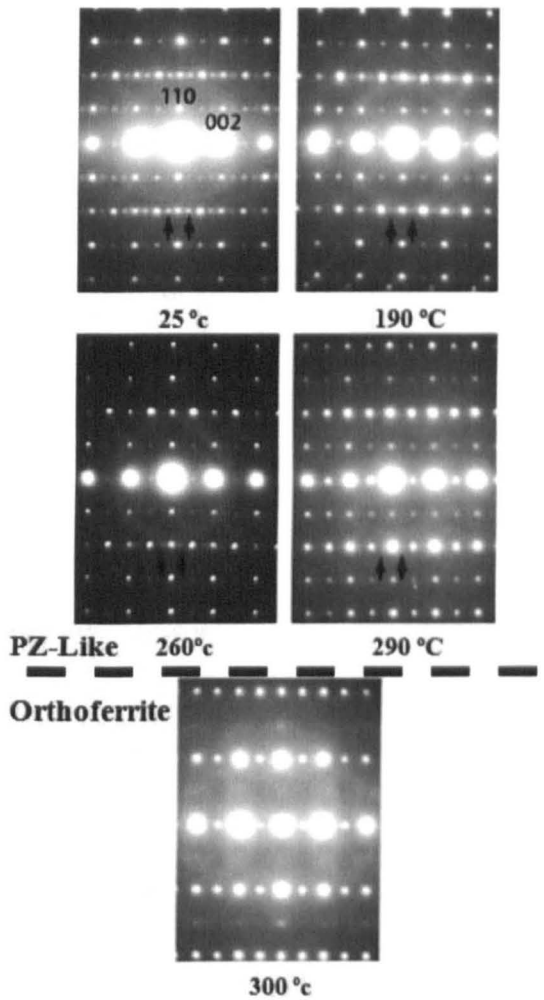

Figure 5.4.16. In-situ electron diffraction patterns for the 15% Nd sample recorded from a single grain containing both $¼\{hh0\}_p$ and $¼\{00l\}_p$ reflections suggesting that $¼\{00l\}_p$ reflections evolve/disppear at temperatures lower than the temperature of $PbZrO_3$-like to orthoferrite phase transition. First presented by [Levin, Karimi and co-workers, 2011].

5.5. Raman Spectroscopy

Raman spectroscopy was performed as a function of composition for all RE-doped $BiFeO_3$ samples fabricated in this study, Figures 5.5.1. No attempt was made to assign vibrational modes to the observed bands and the spectra achieved were used primarily in a comparative manner as a means of assessing the onset of structural phase transitions. All room temperature spectra broadly followed the same trends as observed in XRD, Figure 5.1.3. For 10% RE-doped compositions, all spectra exhibited modes consistent with the rhombohedral, *R3c* structure of $BiFeO_3$. However, samples with 12.5% Gd, 12.5% ≤ Sm ≤ 15%, 15% ≤ Nd ≤ 20% and 20% ≤ La ≤ 25% exhibited similar spectra to each other but markedly different to that of compositions with ≤ 10% RE.

The XRD traces for 12.5% Gd, 12.5% ≤ Sm ≤ 15%, 15% ≤ Nd ≤ 20% and 20% ≤ La ≤ 25% exhibited the $PbZrO_3$-like structure, Figure 5.1.3, and therefore their Raman spectra were considered as characteristic of the new quadrupled cell. Samples with 17.5% Sm and 25% Nd have a mixed phase of $PbZrO_3$-like and orthoferrite and therefore spectra characteristic of the quadrupled cell may be observed alongside spectra from the doubled orthoferrite phase. The 12.5% Gd sample is on the boundary of transformation from the *R3c* to orthoferrite phase at which the quadrupled phase is known to exist in the other RE doped systems. The appearance of some spectra consistent with the $PbZrO_3$-like phase as well as some electron diffraction patterns, Figure 5.4.13, suggests that it may be possible by use of multiple calcinations to homogeneously distribute the Gd^{3+} to stabilise the sample as single phase $PbZrO_3$-like structure within a narrow compositional interval.

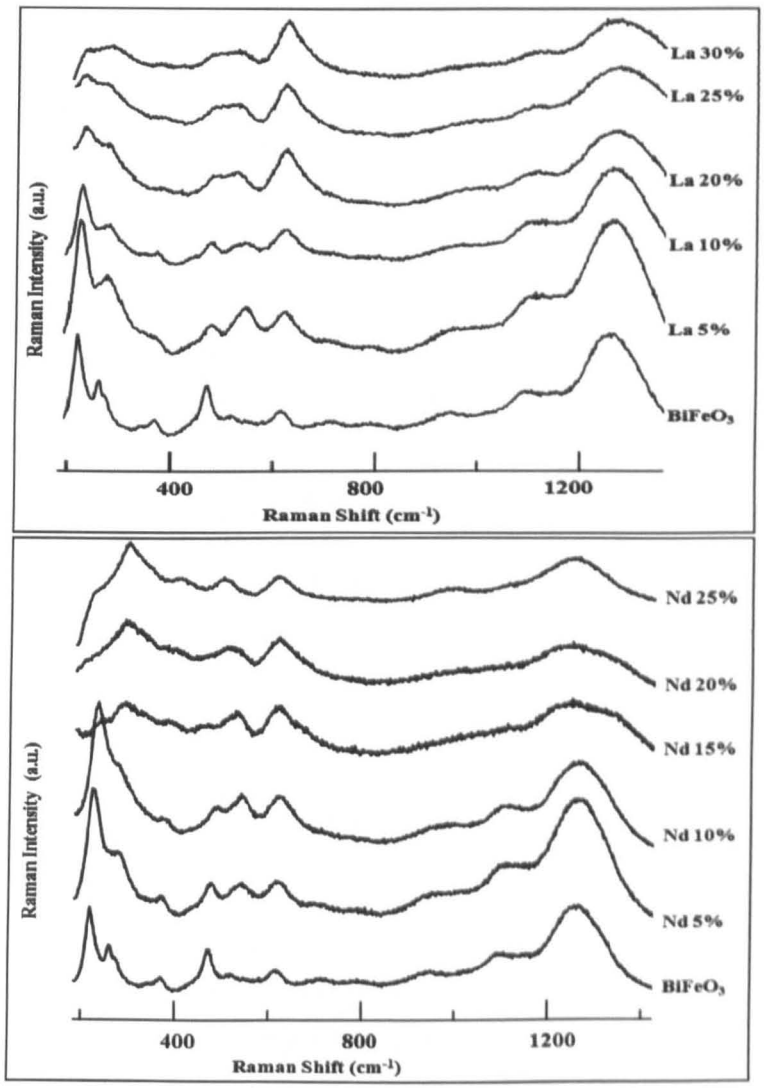
La 30%
La 25%
La 20%
La 10%
La 5%
BiFeO3
Raman Intensity (a.u.)
400
800
1200
Raman Shift (cm-1)
Nd 25%
Nd 20%
Nd 15%
Nd 10%
Nd 5%
BiFeO3
Raman Intensity (a.u.)
400
800
1200
Raman Shift (cm-1)

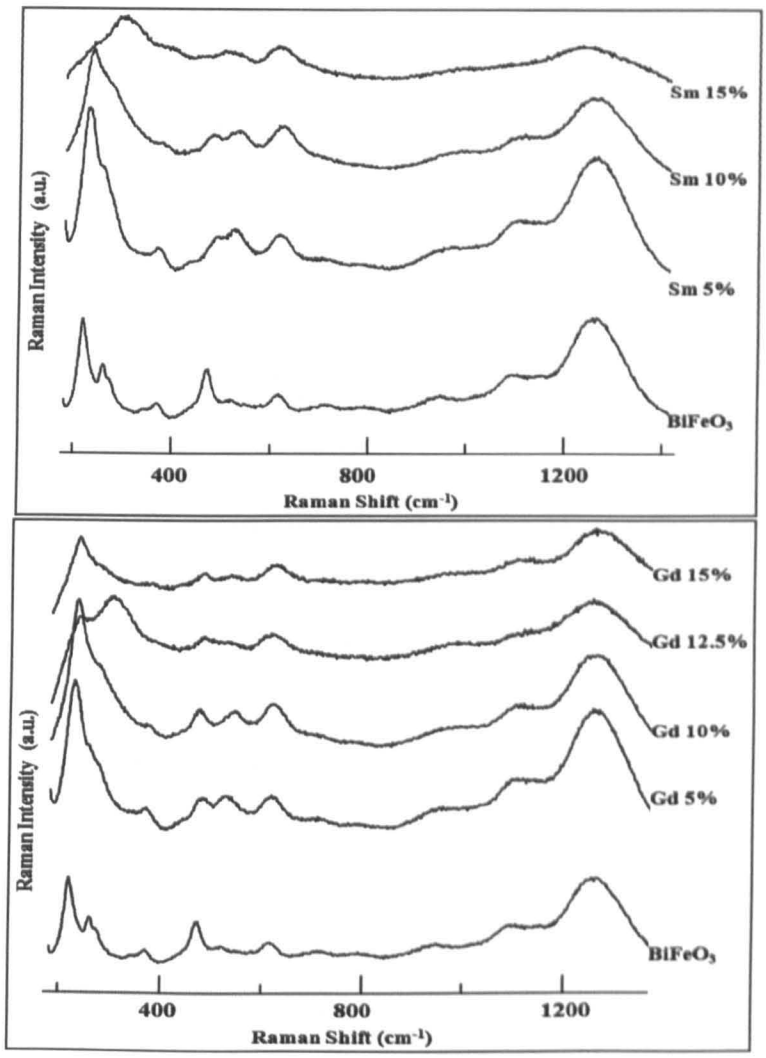

Figure 5.5.1. Raman traces of all compositional series.

Figure 5.5.2 shows the Raman spectra for 10% Nd-doped $BiFeO_3$ obtained from 30 °C to -190 °C. No significant changes in the spectra are observed suggesting that there are no further phase transitions on cooling. However, the modes do reveal characteristic sharpening as a function of decreasing temperature, typical of Raman spectra.

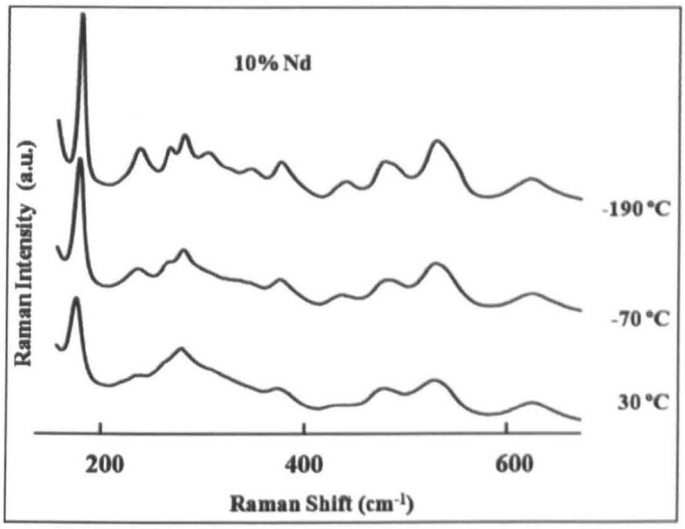

Figure 5.5.2. Raman spectra as a function of temperature for 10% Nd-doped $BiFeO_3$ from 30 °C to 190 °C. First presented in [Karimi *et al.*, 2009a].

Figure 5.5.3 shows the Raman spectra for 20% Nd $BiFeO_3$ from 30 °C to 300 °C. The sharp band at ~180 cm^{-1} disappears at ~200 °C, consistent with the in-situ TEM data shown in Figure 4.15 where a structural phase transition is observed over a broad temperature range from the quadrupled $PbZrO_3$-like to the *Pbam*, orthoferrite structure.

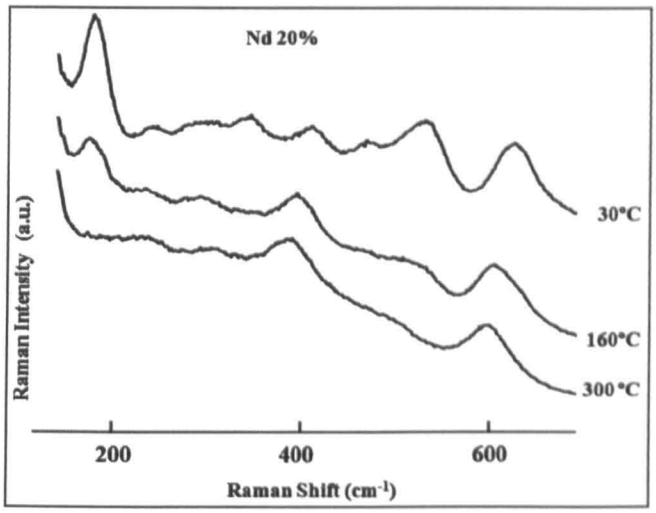

Figure 5.5.3. Raman spectra as a function of temperature for the 20% Nd sample from 30 °C to 300 °C. First presented in [Karimi *et al.*, 2009a].

Raman spectroscopy was also performed on samples with 10 and 15% Nd-doped $BiFeO_3$ which had been sintered in air, argon and oxygen to illustrate the effect of annealing atmosphere on phase formations, Figure 5.5.4. In general, there is no difference in the traces irrespective of the annealing atmosphers, suggesting that O-stoichiometry is not a significant factor in the phase equilibria of RE-doped $BiFeO_3$ compositions.

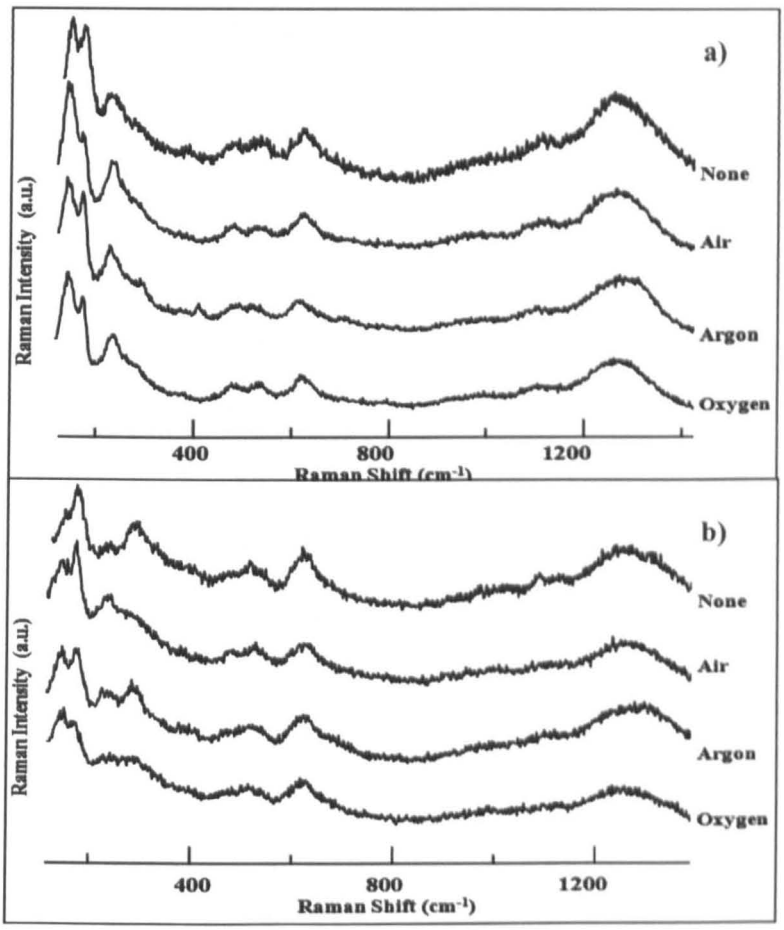

Figure 5.5.4. Raman spectra for a) 10% and b)15% Nd samples annealed in different atmospheres.

5.6. Neutron Diffraction Studies

Neutron diffraction measurements were performed partly on POLARIS located on beamline N7 at the ISIS, Didcot, UK as a part of a joint project with Dr. T. Comyn, The University of Leeds and partly in collaboration with Dr. I. Levin at the Rutherford Appleton Laboratories. In-situ neutron powder diffraction data were collected for samples of the Nd series as examples of the *R3c*, $PbZrO_3$-like and orthoferrite structures, to investigate the structural and magnetic phase transitions. Figures 5.6.1 and 5.6.2 show the time of flight (*t.o.f*) graphs of the neutron diffraction data as a function of temperature for 17.5% and 25% indicating the structural and magnetic transitions as temperature changes.

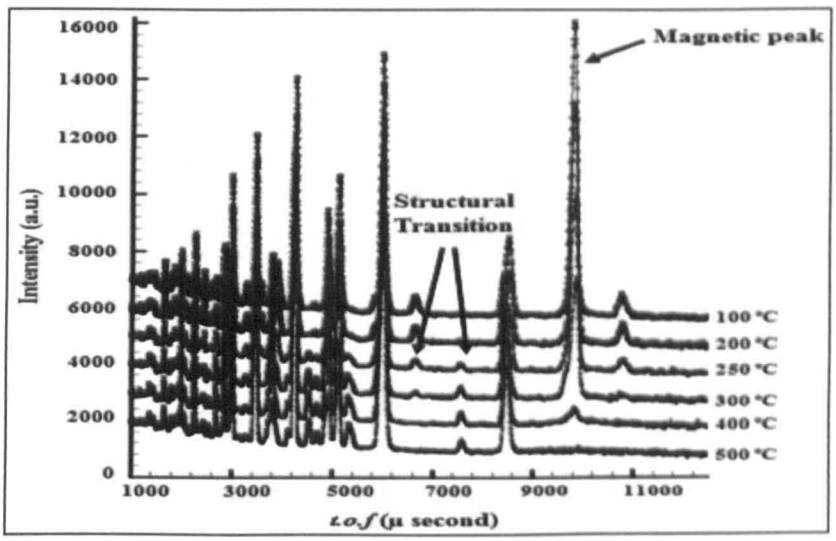

Figure 5.6.1. Neutron diffraction as a function of temperature for a 17.5% Nd sample where T_C and T_N can be observed. A structural change to the orthoferrite phase starts at ≈ 250 °C (T_C) while the strong magnetic peak at 100 °C weakens as the temperature increases to about T_N and disappears completely at 500 °C.

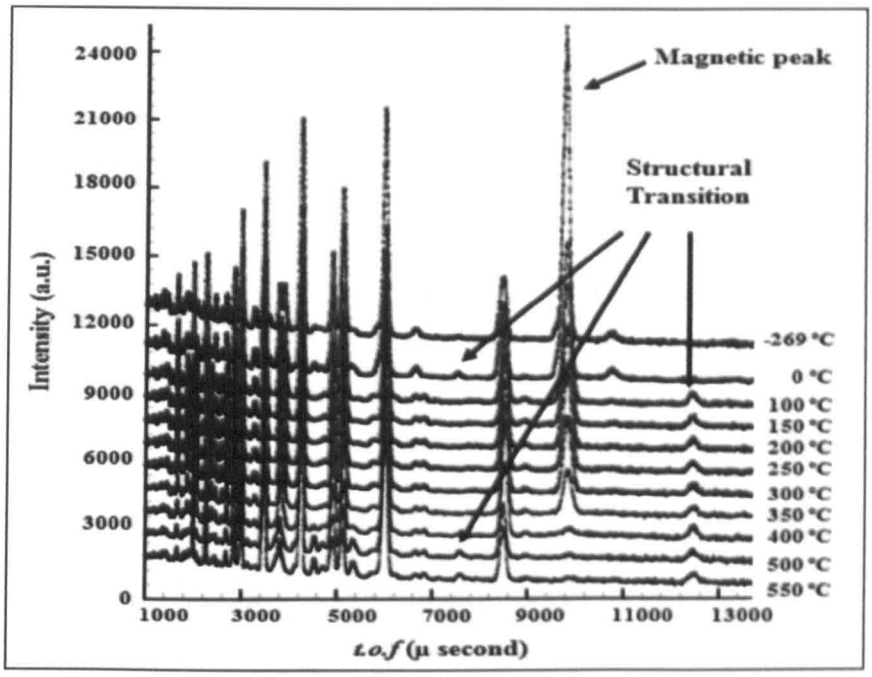

Figure 5.6.2. Neutron diffraction as a function of temperature for a 25% Nd sample with several structural transitions between -269 °C and 550 °C while the very strong magnetic peak at very low temperatures starts disappearing at about 400 °C. The structural change below the room temperature can be related to T_C as predicted by DSC results. This also confirmed the T_N measured by DSC to be about 400 °C.

5.6.1. Transition from Rhombohedral *R3c* to Orthoferrite *Pnma*

The neutron diffraction patterns for compositions doped with 10% Nd can be fitted satisfactorily assuming a rhombohedral structure with *R3c* symmetry below and an orthorhombic structure with *Pnma* symmetry above T_C. Figure 5.6.3, first presented by [Levin, Karimi and co-workers, 2010 and 2011], shows the experimental and calculated neutron powder diffraction profiles of compositions doped with 10% Nd for the

rhombohedral *R3c* phase at room temperature and the orthoferrite phase above 600 °C. The nuclear parameter for the *R3c* and *Pbnm* phases are listed in Table 5.6.1. The goodness of fit R_{wp} values were 3.69 % and 3.33 % for the data at 25 °C and 600 °C, respectively.

No ordering of Bi and Nd ions was refined and a random occupying of the 6*a* and 4*c* sites, respectively has been utilised. Similar to pure $BiFeO_3$ [Arnold *et al.*, 2009] the rhombohedral to orthoferrite transition is accompanied by an abrupt expansion of the unit cell volume in the rhombohedral phase by about ≈1.8 %, Figure 5.6.4.

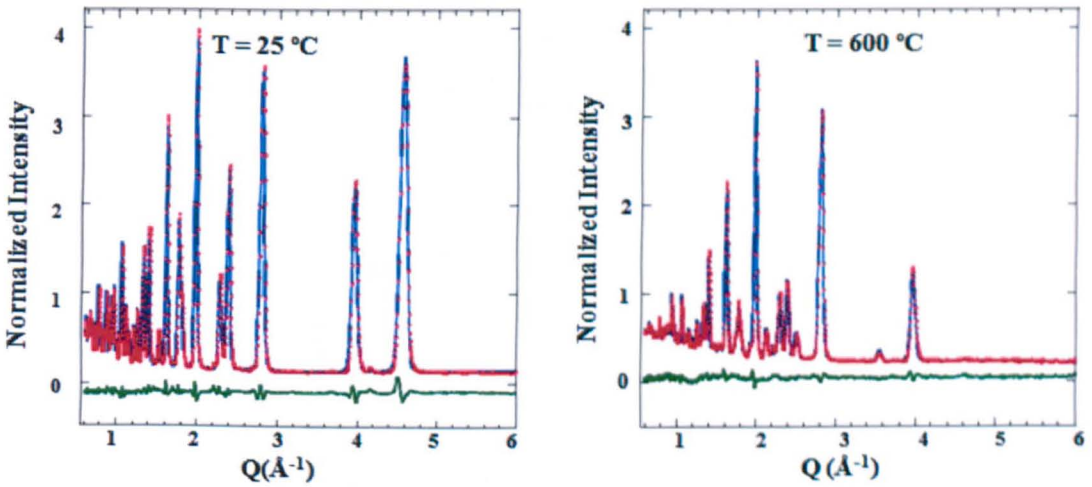

Figure 5.6.3. Experimental and calculated neutron powder diffraction profiles for rhombohedral *R3c* phase of the 10% Nd at room temperature and the orthoferrite phase above 600 °C.

Table. 5.6.1. Structural (nuclear) parameters for the *R3c* and *Pbnm* phases of 10% Nd doped sample obtained by Rietveld refinements using powder neutron diffraction data collected at 25 °C and 600 °C, respectively.

Atom	Site	*x*	*y*	*z*	$U_{iso} \times 100$ (Å^2)
R3c space group (#161), $a = 5.56819(3)$ Å, $c = 13.7856(1)$ Å					
$Bi_{0.9}Nd_{0.1}$	6*a*	0	0	0.04393	0.92(2)
Fe	6*a*	0	0	0.26752	0.45(1)
O	18*b*	0.4434	0.0177	0	0.83(2)
Pbnm space group (#62), $a = 5.4387(7)$, $b = 5.63331(8)$, $c = 7.9101(1)$					
$Bi_{0.9}Nd_{0.1}$	4*c*	-0.0044	0.03634	¼	3.64(1)
Fe	4*b*	0	½	0	1.31(6)
O1	4*c*	0.0779	0.4792	¼	2.85(2)
O2	8*d*	0.7045	0.2926	0.0389	3.23(1)

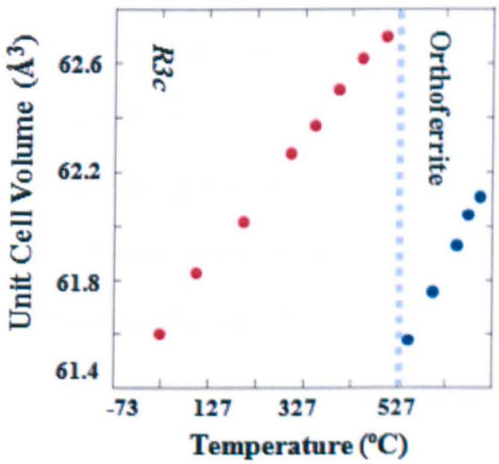

Figure 5.6.4. Temperature dependence of the unit cell volume for compositions doped with 10% Nd obtained from the refinements using powder neutron diffraction data.

5.6.2. Transition from the $PbZrO_3$-Like to the Orthoferrite Structure

The detailed analysis of the transition from the $PbZrO_3$-like to orthoferrite phase was performed on ceramics doped with 17.5% Nd. The XRD (Figure 5.1.3b) and neutron diffraction (Figure 5.6.1) data confirmed that below T_C a $PbZrO_3$-like structure was present that could be fitted to *Pbam* symmetry whereas above T_C the structure was orthoferrite as discussed in section 5.6.1. The *Pbam* cell satisfactorily fitted all room temperature neutron powder diffraction data collected for all samples with $15 \leq Nd\% \leq 20$ and accounted for all observed reflections, Figures 5.6.6.

Table 5.6.2 shows the refined nuclear parameters for the $PbZrO_3$-like and the orthoferrite Pbnm phase for the sample with 17.5% Nd. No Bi / Nd order was detected and the R_{wp} and χ^2 values for the $PbZrO_3$-like phase were 44.18% and 2.44, respectively. Large and anisotropic atomic displacement parameters for oxygen and Bi/Nd positions, Table 5.6.2, indicate that the actual structure, perhaps locally, deviates from *Pbam* symmetry. Deviations from the *Pbam*, $\sqrt{2}a_c$, $2\sqrt{2}a_c$, $2a_c$ model, highlighted by the large anisotropic atomic displacement parameters, are consistent with the electron diffraction data presented in section 5.4, which revealed a series of $\frac{1}{4}\{00l\}_p$-type superlattice reflections. These reflections demonstrate that the cell is doubled with respect to that of $PbZrO_3$ to give the approximate cell dimensions, $\sqrt{2}a_c$, $2\sqrt{2}a_c$, $4a_c$.

A large discontinuous volume change similar to that encountered in $BiFeO_3$ [Arnold *et al.*, 2009] and in the 10% Nd sample is observed during the transition from $PbZrO_3$-like to orthoferrite structure as exemplified in Figure 5.6.7 for compositions doped with 15% Nd.

In addition to the unit cell volume, changes in the lattice parameters across the structural transition in 15% Nd doped sample are also ilustrated in Figure 5.6.7. The change in volume

is largely determined by changes in the b^* dimension (horizontal in Figure 5.4.13). The transition from $PbZrO_3$-like to orthoferrite phase is similar to the transition from *R3c* to orthoferrite, in as much as there is an abrupt expansion of the unit cell volume and each is accompanied by the disappearance of the in-phase tilt axis.

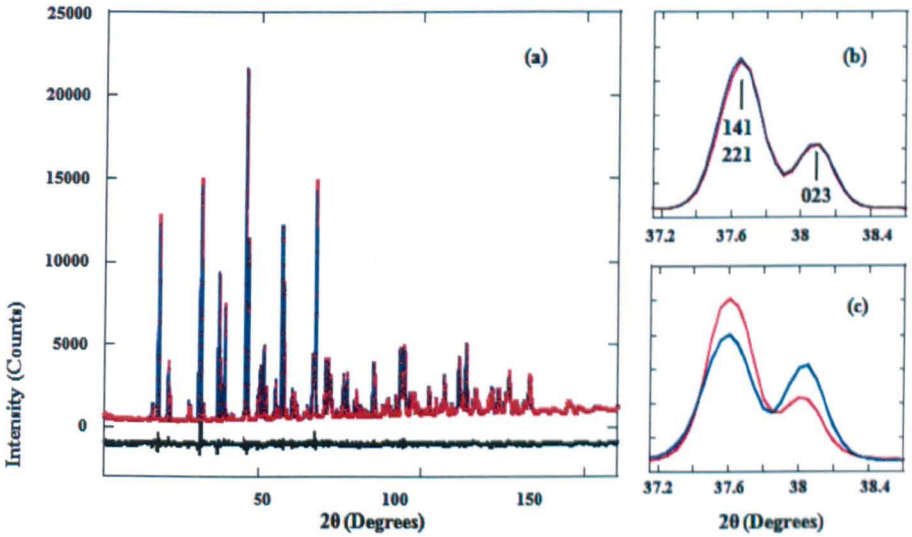

Figure 5.6.6. a) Experimental and calculated constant-wavelength neutron diffraction profile for $PbZrO_3$-like structure of the 17.5% Nd sample at room temperature, R_{wp}= 4.18%, and b) and c) fit for a pair of reflections (*141 / 221* and *023*) for the models with *c*-axis and *a*-axis orientation of the magnetic moments, respectively. First presented at [Levin, Karimi and co-workers, 2010].

The temperature dependence of the refined Bi displacements relative to the ideal fixed coordinate positions is displayed in Figure 5.6.8. Bi displacements in both structures occur along the 2-fold symmetry axes parallel to the rotation axes of the octahedra (a^-a^- tilt); however, the displacement patterns in the two structures are different. The magnitude of Bi

displacements in the orthoferrite structure exhibits an apparent anomaly at the temperature of the magnetic transition which suggests strong coupling of Bi displacements and octahedral tilting to the magnetic ordering. This transition is accompanied by the abrupt *c*-to *a*-axis reorientation of magnetic dipoles. The intensity distribution among the *141/221* and *023* magnetic reflections, Figure 5.6.6b, is very sensitive to orientations of magnetic moments and enables reliable identification of the moment directions [Sosnowska *et al.*, 1982].

Table 5.6.2. Structural(nuclear) parameters for the PZ-like and orthoferrite phases of 17.5 % Nd doped sample obtained by Rietveld refinements using powder neutron diffraction data collected at 25 °C and 375 °C, respectively.

Atom	Site	*x*	*y*	*z*	$U_{iso} \times 100$ (Å^2)
Pbam space group (#55), $a = 5.58663(6)$, $b = 11.2235(1)$, $c = 7.79956(6)$					
$Bi_{0.825}Nd_{0.175}$	4	0.7970	0.1320	0	1.22(1)
$Bi_{0.825}Nd_{0.175}$	4	0.7934	0.1266	0.2517	2.14(2)
Fe	8	0.2582	0.1215	0.2517	0.34(1)
O1	4	0.1964	0.0883	0	1.05(1)
O2	4	0.7215	0.3379	½	2.25(1)
O3	8	-0.0409	0.2381	0.2128	1.84(1)
O4	4	0	½	0.2779	3.88(3)
O5	4	0	0	0.3055	1.66(2)
Pbnm space group (#62), $a = 5.4387(7)$, $b = 5.63331(8)$, $c = 7.9101(1)$					
$Bi_{0.825}Nd_{0.175}$	4*c*	-0.0058	0.0428	¼	2.19(2)
Fe	4*b*	0	½	0	0.78(1)
O1	4*c*	0.0835	0.4765	¼	1.63(1)
O2	8*d*	0.7013	0.2957	0.0417	2.06(1)

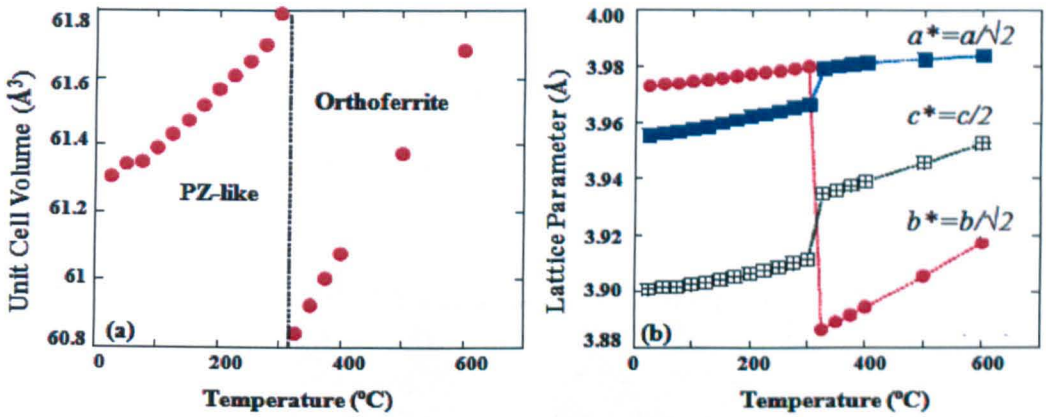

Figure 5.6.7. Temperature dependence of a) the unit-cell volume and b) lattice parameters for the 15% Nd. In Figure 5.4.13 the *a* axis is parallel to the viewing and the *b* axis is horizontal. First reported by [Levin, Karimi and co-workers, 2010].

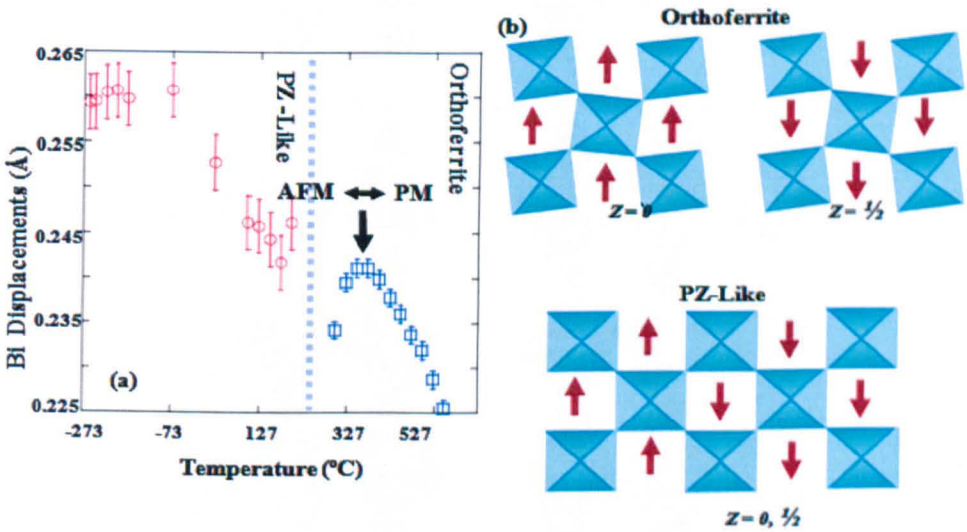

Figure 5.6.8. a) Temperature dependence of the magnitude of Bi displacements off the ideal fixed coordinate positions and b) schematic illustration of Bi displacement pattern in the orthoferrite and $PbZrO_3$-like structures, indicated with arrows. First presented by [Levin, Karimi and co-workers, 2011].

Below -220 °C, a reverse *c*-to *a*-axis reorientation of the magnetic moments is observed, Figure 5.6.9, however, in this case, the reorientation transition is gradual without any detectable changes in the nuclear structure.

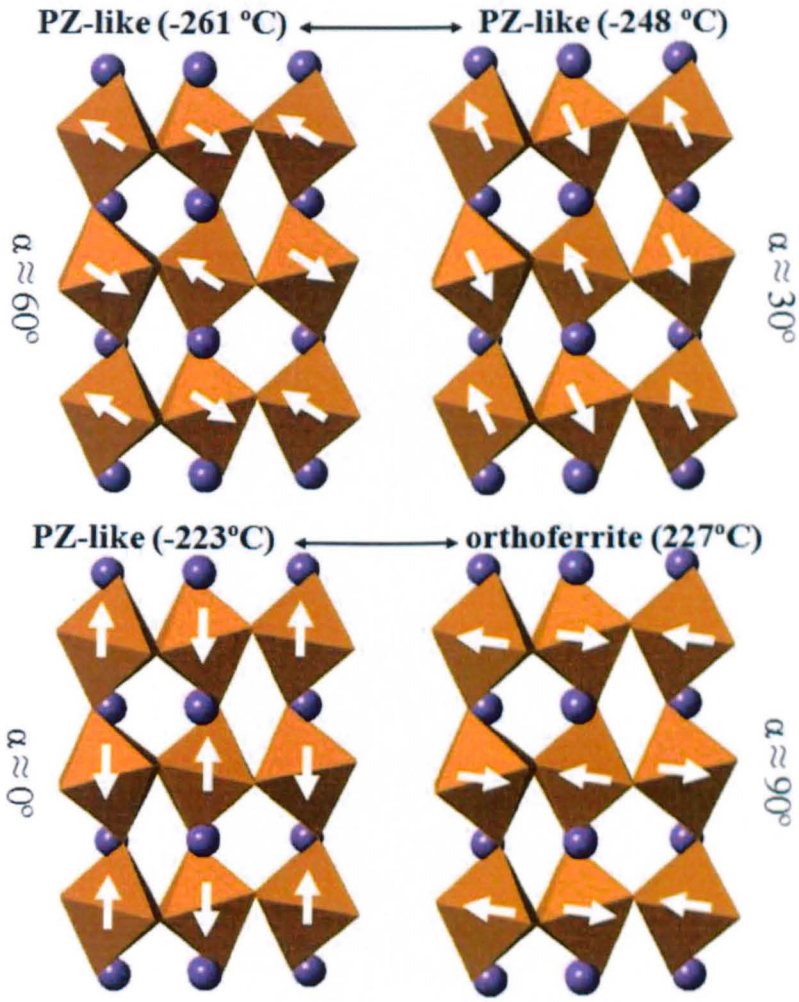

Figure 5.6.9. Schematic rendering of the orientations of magnetic dipoles in the 17.5% Nd sample as a function of temperature. Note that there is a second reorientation transition below -223 °C. First presented in [Levin, Karimi and co-workers, 2011].

5.7. Dielectric measurements as a function of temperature

Relative permittivity, ε_r, and the tanδ dielectric loss were measured as a function of temperature for all the compositions, Figures 5.7.1 to 5.7.4. Some compositions (typically with $x < 0.1$) exhibited weak anomalies in the permittivity below the nominal T_C, observed as broad peaks between 200 °C and 400 °C. These typically disappeared at higher frequencies and for higher dopant concentrations ($x > 0.1$). At ~370 °C according to DSC data, Figure 5.3.1, all compositions undergo a transition from paramagnetic to antiferromagnetic (T_N). If this phase transition is responsible for these broad peaks in ε_r, it is not clear why the peak temperature should be frequency dependent or why changes in the magnetic moment should induce peaks in the dielectric data. Dielectric loss for all samples is typically low (< 0.05) at room temperature for higher dopant concentrations (≥ 10%) but at temperatures above ~ 150 °C, loss values rise sharply presumably as a result of enhanced conductivity. The onset temperature for the steep rise in dielectric loss is dependent on the RE dopant type and the frequency. Generally, Nd and Gd doped compositions have the lowest losses but currently there is no explanation for this behaviour. It is evident that RE dopants improve dielectric loss in $BiFeO_3$ based compositions, however, the conductivity appears too high at elevated temperature to reveal the anomalies associated with the phase transitions, readily observed by DSC.

Microstructural factors such as secondary phases, porosity and lattice defects all contribute to dielectric losses [Ferreira and Baptista, 1994] and $BiFeO_3$-based ceramics are notoriously difficult to study dielectrically and ferroelectrically for numerous reasons. The most likely explantion for the improvement in dielectric loss as the RE dopant concentration increases

relates to the elimination of the highly conducting sillenite phases at typically $x \geq 0.1$. It is clear however, that further work is required to a) determine the nature of the conductivity in RE-doped $BiFeO_3$ (i.e. p/n type semiconduction) and b) determine the requisite dopant strategy to eliminate charge carriers.

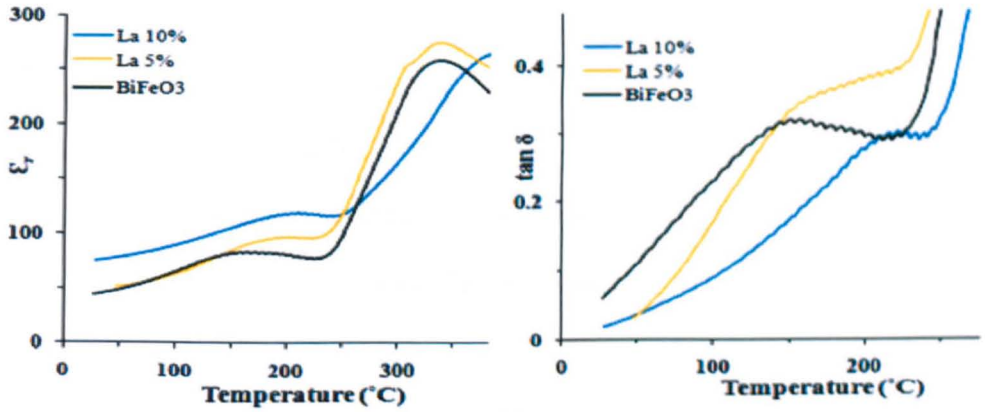

Figure 5.7.1. Permittivity and dielectric loss as functions of temperature measured for the La doped $BiFeO_3$ samples.

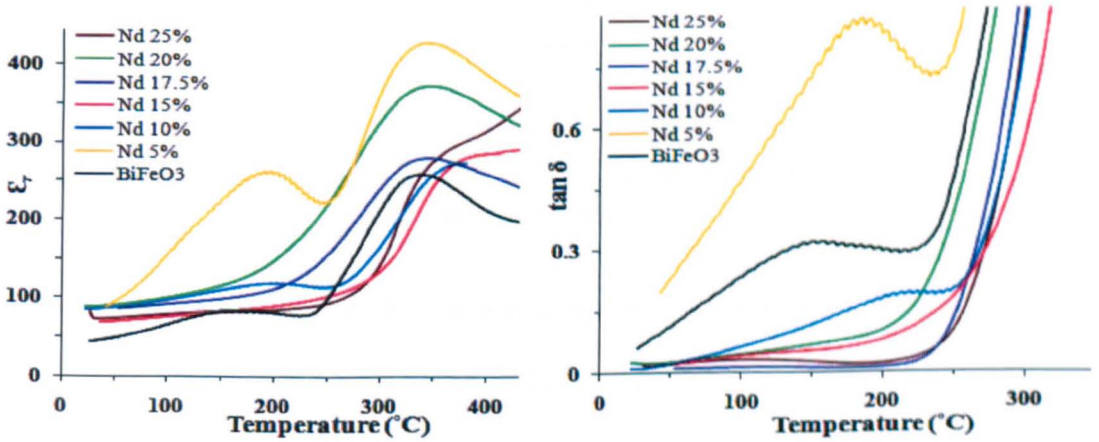

Figure 5.7.2. Permittivity and dielectric loss as functions of temperature measured for the Nd doped $BiFeO_3$ samples.

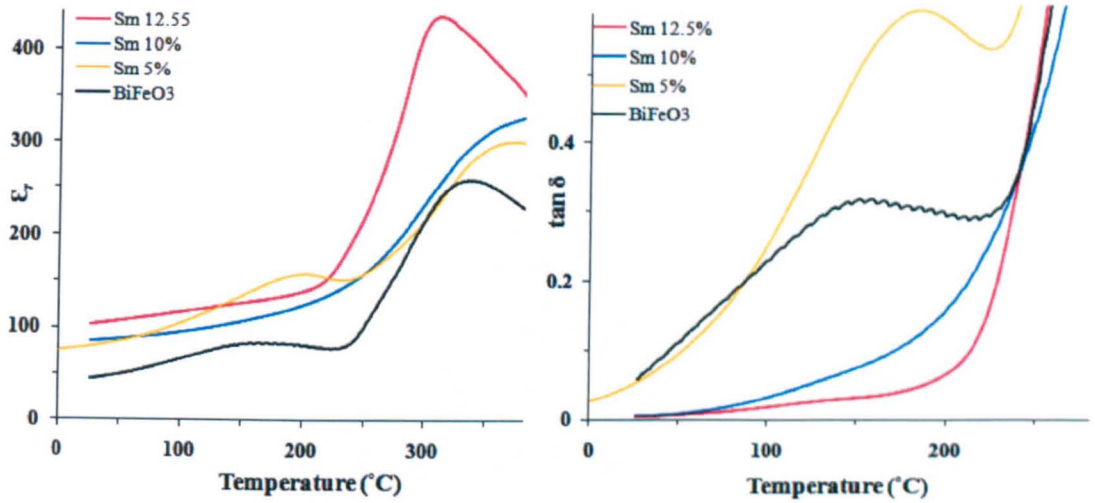

Figure 5.7.3. Permittivity and dielectric loss as functions of temperature measured for the Sm doped $BiFeO_3$ samples.

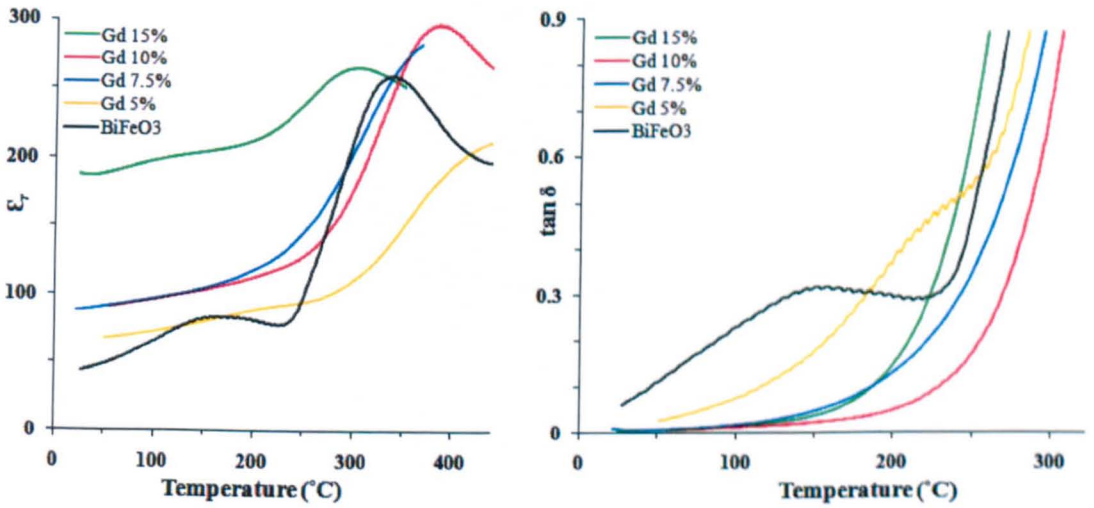

Figure 5.7.4. Permittivity and dielectric loss as functions of temperature measured for the Gd doped $BiFeO_3$ samples.

5.8. Polarization vs. Electric Field

Polarization was measured as a function of applied electric field for 20% Nd-doped sample. The obtained loops are shown in Figure 5.8.1. The hysteresis measurements are a decisive method for determining ferroelectricity of a sample as ferroelectric materials will switch at fields higher than their coercive field to a saturation polarisation. This should be reversible and give rise to a remnant polarisation on removal of the field. The poor quality loops shown are not untypical of $BiFeO_3$-based ceramics and many authors have represented such data as arising from reversible polarisation similar to that shown for conventional ferroelectrics such as $BaTiO_3$. Here, it is proposed that the loops are present due to space charge regions reversible in the electric field. It should be noted the 20% Nd-doped compositions have the $PbZrO_3$-like rather than rhombohedral ferroelectric structure. The appearance of ferroelectric loops in this composition is therefore highly unlikely based on its structure. The poor hysteresis associated with these samples once again demonstrates the need to control the defect chemistry in $BiFeO_3$-based compositions by using a suitable dopant strategy so that large fields may be applied with dielectric breakdown and space charge effects can be eliminated.

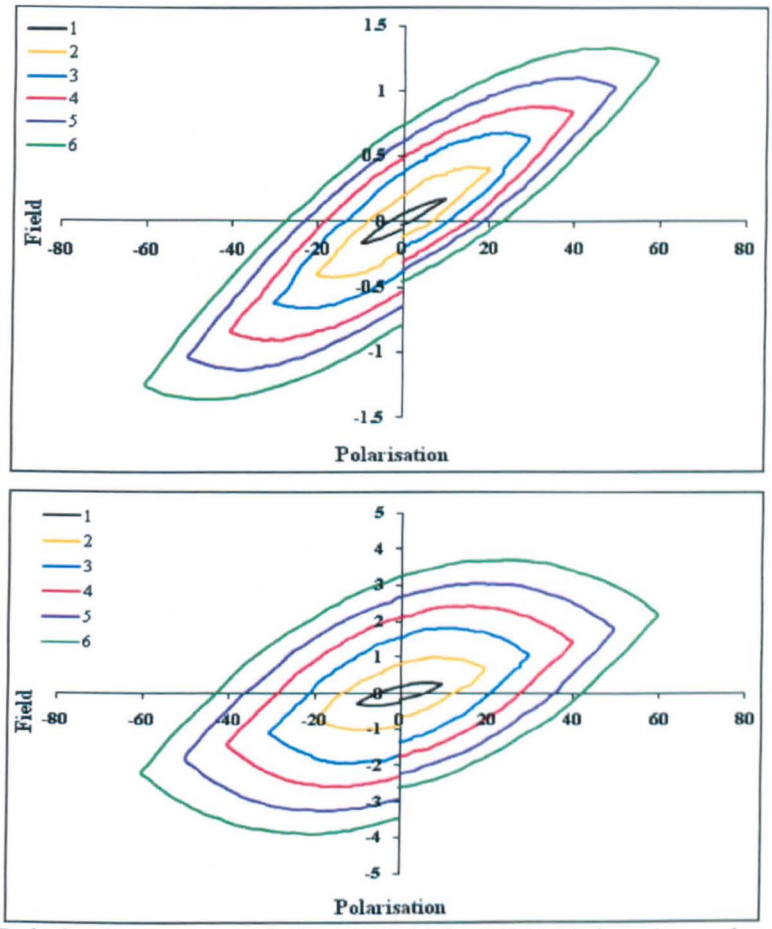

Figure 5.8.1. Polarization vs. applied electric field for 20% Nd-doped sample with a a) fully coated and b) partially coated electrode.

5.9. Magnetic Measurement

Magnetic measurements were first presented by [Levin, Karimi and co-workers, 2010 and 2011] and were performed at the National Institute of Science and Technology, MD, USA. The *R3c* phase of the 10% Nd develops very slim magnetic hysteresis loops, whereas for higher concentrations of Nd, a robust ferromagnetic response, $H_C \approx 4170$ Oe and $H_C \approx 1950$ Oe for 15 and 20% Nd respectively, were obtained below the magnetic transition. In all cases, the response was characteristic of a paramagnetic state at high temperatures. Figure 5.9.1 illustrates the magnetic hysteresis loops, *M-H*, and graphs of the temperature dependence of magnetization, *M-T*, between room temperature and 700 °C for three compositions. The magnetic transitions are clearly manifested in the large increase of magnetization. Importantly a pronounced peak of magnetization was also observed around temperatures of structural phase transitions.

For compositions doped with 10% Nd where the structural transition is in the paramagnetic state, the peak in magnetisation is weak and most prominent for larger fields. In contrast, for compositions doped with 15% Nd, the peak in magnetisation becomes pronounced for weak fields since for strong fields the effect is masked by an increase in magnetization upon crossing the magnetic transition temperature. The results are in complete agreement with the interpretation of the Neutron diffraction data in which magnetic dipoles were shown to reoreient upon at the onset of the FE-PE and AFE-PE structural transition, as described in section 5.6. Conceivably, even in the paramagnetic state, the magnetic moments are preferentially aligned with one of the crystallographic axes and the weak peak of

magnetization for ceramics doped with 10% Nd is caused by reorientation of the moments which is further facilitated by applied magnetic field.

For compositions doped with 20% Nd, where the structural transition occurs well below T_N, the peak of magnetization was evident even at large fields, e.g. 2000 Oe. For compositions doped with, 15 and 20% Nd, in addition to a steep rise in the magnetization at the magnetic transition, a second anomaly was observed which presumably arises due to the $PbZrO_3$-like to orthoferrite phase transition. The temperature of this magnetic anomaly was field dependent and decreased systematically with increasing Nd content in accordance with the AFE-PE and FE-PE transitions

The second dipole-reorientation transition below -220 °C, which occurs without any detectable structural transition is also manifested in the magnetization anomaly, however, this change in magnetization is not abrupt, consistent with the results inferred from neutron diffraction data. Interestingly, the coercive field exhibits well-defined anomalies both at the $PbZrO_3$-like to orthoferrite transition and the low-temperature magnetic dipole-reorientation transition. These results indicated a very intimate coupling between the displacive (tilting, cation displacements) and magnetic order parameters which is manifested in the displacement and magnetization anomalies at the temperatures of the magnetic and structural phase transitions.

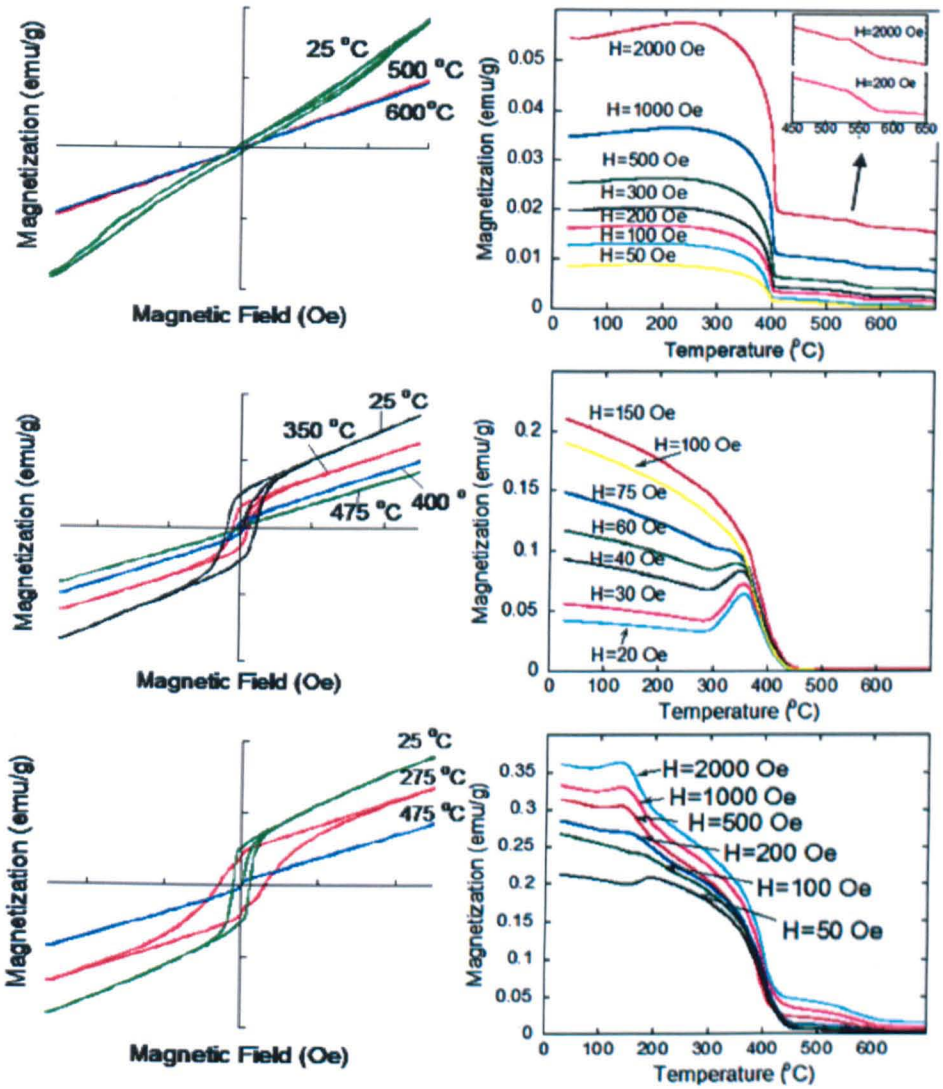

Figure 5.9.1. Field (H) dependence of magnetization (M) for a) 10% b) 15% and c) 20% Nd samples at selected temperatures and temperature dependence of magnetization under different external fields for d) 10%, e) 15% and f) 20% Nd. Before each variable temperature scan the samples were first subjected to a magnetic field of 70,000 Oe and the the field was reduced to a selected value. First presented in [Levin, Karimi and co-workers, 2010 and 2011]

5.10. Summary

High density pellets of $Bi_{1-x}RE_xFeO_3$ RE = La, Nd, Sm, Gd and $0 \leq x \leq 0.4$ were successfully made. XRD and SEM showed that for $x < 0.1$ in La, Nd and Sm and $x < 0.075$ in Gd series secondary phases of $Bi_2Fe_4O_9$ and $Bi_{25}FeO_{40}$ existed. According to X-ray, electron and neutron diffraction data collected for La, Nd and Sm with $x \leq 0.1$ and Gd with $x \leq 0.075$ the perovskite phase could be indexed according to the rhombohedral, *R3c* cell of $BiFeO_3$.

The $REFeO_3$ orthoferrite *Pnma* structure was present for $x > 0.1$, $x > 0.15$, $x > 0.2$ and $x>0.4$ in Gd, Sm, Nd and La doped $BiFeO_3$, respectively. The orthoferrite phase appeared at lower values of x as the RE ion radius decreased.

For La, Nd and Sm with $0.1 < x \leq 0.3$, $0.1 < x \leq 0.2$ and $0.1 < x \leq 0.175$, respectively, a new phase was stabilised with peak splitting and superlattice reflections similar to that of the orthorhombic, antiferroelectric $PbZrO_3$. In-situ Raman spectroscopy and electron and neutron diffraction data demonstrated that on heating, the $PbZrO_3$-like phase transforms to the orthoferrite, *Pnma* structure of the $REFeO_3$ end member. DSC showed that T_C for all compositions decreased with the increasing RE concentration but the rate of decrease per % increased with decreasing RE-ion radius.

In TEM images and electron diffraction data for compositions with *R3c* symmetry, superstructure and orientational and translational (anti-phase) domains were observed in a manner typical of an anti-phase tilted, ferroelectric perovskite. For the new $PbZrO_3$-like phase, orientational domains from the ferroelastic transition and additional anti-phase boundaries associated with regions of antipolar order were observed. Electron diffraction

patterns from the new $PbZrO_3$-like phase that it is doubled with respect to $PbZrO_3$ ($\sqrt{2}a_c$, $2\sqrt{2}a_c$, $2a_c$) with an approximate unit cell, $\sqrt{2}a_c$, $2\sqrt{2}a_c$, $4a_c$.

Neutron powder diffraction was used to determine changes in the nuclear and magnetic structures in the Nd series across the phase transitions. A large volume change encountered during the high temperature phase transition in $BiFeO_3$ was maintained upon RE substitution and was particularly evident for the antiferroelectric to paralectric transition between the $PbZrO_3$-like and orthoferrite structures. Both transitions from orthoferrite structure to *R3c* and $PbZrO_3$-like are accompanied by large discontinuous expansion of the lattice volume in the low-temperature structures. The orthoferrite to *R3c* transition occurs in the paramagnetic state and generates no detectable changes in the magnetic structure. In contrast, the orthoferrite to $PbZrO_3$-like transition, which occurs in the magnetic state, is accompanied by abrupt $\approx$ 90 ° reorientation of the magnetic dipoles. The magnetic moments retain their overall G-type antiferromagnetic arrangement upon this structural change. This coupling between the nuclear and magnetic structures is manifested in the significant magnetization anomaly.

Dielectric measurements of the RE-doped compositions revealed that the conductivity was reduced, particularly for samples with $x > 0.1$, above which non perovskite second phases are eliminated. However, the dielectric loss was still too high to observe dielectric anomalies associated with the phase transitions readily observed in DSC. Ferroelectric hysteresis curves exhibited clear evidence of space charge reorientation rather than classic ferroelectric behaviour.

5.11. References

ACHENBACH, G. D., JAMES, W. J. & GERSON, R. (1967) *Preparation of Single-Phase Polycrystalline $BiFeO_3$.* Journal of the American Ceramic Society, **50,** 437.

ARNOLD, D. C., KNIGHT, K. S., MORRISON, F. D. & LIGHTFOOT, P. (2009) *Ferroelectric-Paraelectric Transition in $BiFeO_3$: Crystal Structure of the Orthorhombic beta Phase.* Physical Review Letters, **102,** 027602.

CHENG, Z. X., LI, A. H., WANG, X. L., DOU, S. X., OZAWA, K., KIMURA, H., ZHANG, S. J. & SHROUT, T. R. (2008a) *Structure, ferroelectric properties, and magnetic properties of the La-doped bismuth ferrite.* Journal of Applied Physics, **103,** 07E507.

CHENG, Z. X., WANG, X. L., DOU, S. X., KIMURA, H. & OZAWA, K. (2008b) *Enhancement of Ferroelectricity and Ferromagnetism in RareEarth Element Doped $BiFeO_3$.* Journal of Applied Physics, **104,** 116109.

COMYN, T. P., MCBRIDE, S. P. & BELL, A. J. (2004) *Processing and electrical properties of $BiFeO_3$-$PbTiO_3$ ceramics.* Materials Letters, **58,** 3844.

FERREIRA, V. M. & BAPTISTA, J. L. (1994) *PREPARATION AND MICROWAVE DIELECTRIC-PROPERTIES OF PURE AND DOPED MAGNESIUM TITANATE CERAMICS.* Materials Research Bulletin, **29,** 1017.

FILIP'EV, V. S., SMOL'YANINOV, I. P., FESENKO, E. G. & BELYAEY, I. I. (1960) *Synthesis of $BiFeO_3$ and Determination of the Unit Cell.* Soviet Physics - Crystallography, **5,** 913.

FISCHER, P., POLOMSKA, M., SOSNOWSKA, I. & SZYMANSKI, M. (1980) *Temperature-Dependence of the Crystal and Magnetic-Structures of $BiFeO_3$.* Journal of Physics C-Solid State Physics, **13,** 1931.

GLAZER, A. M. (1972) *The Classification of Tilted Octahedra in Perovskites.* Acta Crystallographica, **B28,** 3384.

KARIMI, S., REANEY, I. M., HAN, Y., POKORNY, J. & STERIANOU, I. (2009a) *Crystal chemistry and domain structure of rare-earth doped $BiFeO_3$ ceramics.* Journal of Materials Science, **44,** 5102.

KARIMI, S., REANEY, I. M., LEVIN, I. & STERIANOU, I. (2009b) *Nd-doped $BiFeO_3$ ceramics with antipolar order.* Applied Physics Letters, **94,** 3.

KNUDSEN, J. (2002) Structure-Property Relations ar the Antiferroelectric/Ferroelectric Phase Boundary in Undoped and La Doped $Pb(Zr,Ti)O_3$. *Engineering Materials.* Sheffield, The University of Sheffield.

KUBEL, F. & SCHMID, H. (1990) *Structure of a Ferroelectric and Ferroelastic Monodomain Crystal of the Perovskite $BiFeO_3$.* Acta Crystallographica Section B-Structural Science, **46,** 698.

LEE, Y. H., WU, J. M. & LAI, C. H. (2006) *Influence of La doping in multiferroic properties of $BiFeO_3$ thin films.* Applied Physics Letters, **88,** 042903.

LEVIN, I., KARIMI, S., PROVENZANO, V., DENNIS, C. L., WU, H., COMYN, T. P., STEVENSON, T. J., SMITH, R. I. & REANEY, I. M. (2010) *Reorientation of*

magnetic dipoles at the antiferroelectric-paraelectric phase transition of $Bi_{1-x}Nd_xFeO_3$ (0.15 <= x <= 0.25). Physical Review B, **81**, 020103.

LEVIN, I., KARIMI, S., TUCKER, M. G., WU, H., PROVENZANO, V., DENNIS, C. L., T.COMYN & REANEY, I. M. (2011) *Displacive Phase Transitions and Magnetic Structure in Nd-Substituted $BiFeO_3$.* Chemistry of Materials, **Submitted for publication**.

MICHEL, C., MOREAU, J.-M., ACHENBACH, G. D., GERSON, R. & JAMES, W. J. (1969) *Atomic Structure of Two Rhombohedral Ferroelectric Phases in the $Pb(Zr,Ti)O_3$ Solid Solution Series.* Solid State Communications, **7**, 865.

NALWA, K. S. & GARG, A. (2008) *Phase Evolution, Magnetic and Electrical Properties in Sm-Doped Bismuth Ferrite.* Journal of Applied Physics, **103**, 044101.

NALWA, K. S., GARG, A. & UPADHYAYA, A. (2008) *Effect of samarium doping on the properties of solid-state synthesized multiferroic bismuth ferrite.* Materials Letters, **62**, 878.

REANEY, I. M. (1996) Superlattices in Perovskites and Related Materials *Electroceramics V.* Portugal.

REANEY, I. M., GLAZOUNOV, A., CHU, F., BELL, A. & SETTER, N. (1997) *TEM of antiferroelectric-ferroelectric phase boundary in $(Pb_{1-x}Ba_x)(Zr_{1-x}Ti_x)O_3$ solid solution.* British Ceramic Transactions, **96**, 217.

SAWAGUCHI, E., MANIWA, H. & HOSHINO, S. (1951) *Antiferroelectric Structure of Lead Zirconate.* Physical Review, **83**, 1078.

SOSNOWSKA, I., PETERLINNEUMAIER, T. & STEICHELE, E. (1982) *Spiral Magnetic-Ordering in Bismuth Ferrite.* Journal of Physics C-Solid State Physics, **15,** 4835.

SOSNOWSKA, I., PRZENIOSLO, R., FISCHER, P. & MURASHOV, V. A. (1996) *Neutron diffraction studies of the crystal and magnetic structures of $BiFeO_3$ and $Bi_{0.93}La_{0.07}FeO_3$.* Journal of Magnetism and Magnetic Materials, **160,** 384.

STEVENSON, T., COMYN, T. P., BELL, A. J. & CYWINSKI, R. (2007) *Multiferroic (ferroelectro-magnetic) properties of bismuth ferrite lead titanate (x)($BiFeO_3$)-(1-x)($PbTiO_3$).* 2007 Sixteenth Ieee International Symposium on the Applications of Ferroelectrics, Vols 1 and 2, 421.

VALANT, M., AXELSSON, A. K. & ALFORD, N. (2007) *Peculiarities of a solid-state synthesis of multiferroic polycrystalline $BiFeO_3$.* Chemistry of Materials, **19,** 5431.

VEGARD, L. (1921) *The constitution of the mixed crystals and the filling of space of the atoms.* Zeitschrift Fur Physik, **5,** 17.

WILLIAMS, D. B. & CARTER, C. B. (2009) *Transmission Electron Microscopy,* New York, USA, Springer

WOODWARD, D. I. (2004) The Crystal Chemistry of Bismuth-Based Perovskite Solid Solutions. *Engineering Materials.* Sheffield, The University of Sheffield.

WOODWARD, D. I. & REANEY, I. M. (2005) *Electron diffraction of tilted perovskites.* Acta Crystallographica Section B-Structural Science, **61,** 387.

WOODWARD, D. I., REANEY, I. M., EITEL, R. E. & RANDALL, C. A. (2003) *Crystal and domain structure of the $BiFeO_3$-$PbTiO_3$ solid solution.* Journal of Applied Physics, **94**, 3313.

YUAN, G. L. & OR, S. W. (2006a) *Enhanced piezoelectric and pyroelectric effects in single-phase multiferroic $Bi_{1-x}Nd_xFeO_3$ (x=0-0.15) ceramics.* Applied Physics Letters, **88**, 062905.

YUAN, G. L. & OR, S. W. (2006b) *Multiferroicity in polarized single-phase $Bi_{0.875}Sm_{0.125}FeO_3$ ceramics.* Journal of Applied Physics, **100**, 024109.

YUAN, G. L., OR, S. W., LIU, J. M. & LIU, Z. G. (2006) *Structural transformation and ferroelectromagnetic behavior in single-phase $Bi_{1-x}Nd_xFeO_3$ multiferroic ceramics.* Applied Physics Letters, **89**, 052905.

ZALESSKII, A. V., FROLOV, A. A., KHIMICH, T. A. & BUSH, A. A. (2003) *Composition-induced transition of spin-modulated structure into a uniform antiferromagnetic state in a $Bi_{1-x}La_xFeO_3$ system studied using Fe-57 NMR.* Physics of the Solid State, **45**, 141.

Chapter 6: General Discussion

To understand the behaviour of $BiFeO_3$ as a function of increasing RE concentration, comparisons with other systems, such as $Pb(Zr,Ti)O_3$, are potentially useful, Figure 6.1. In $Pb(Zr,Ti)O_3$, when the larger, less polarisable Zr^{4+} substitutes for Ti^{4+} ions the tolerance factor *t*, [Goldschmidt, 1926] decreases and the average polarisability of the ions within the structure decreases. A direct consequence of the decrease in polarisability is a decrease in ferroelectric T_C. However, *t* simultaneously decreases resulting in an increase in the driving force for octahedral rotation [Jaffe *et al.*, 1971, Michel *et al.*, 1969, Woodward, 2004, Woodward *et al.*, 2005]. The decrease in polarisability and tolerance factor as Z_r concentration increases drives the system towards an antiferroelectric rather than ferroelectrtic structure and the symmetry changes from *R3m/R3c* in which the Pb displacements are essentially parallel along the $[111]_p$ direction to *Pbam* in which the A-site ions are displaced in antiparallel along $[110]_p/[-1-10]_p$.

At room temperature $BiFeO_3$ has a rhomobohedral structure described by a corner-shared network of FeO_6 octahedra in which the cubooctahedral cage is filled with Bi ions. The FeO_6 octhedra are distorted with an $a^-a^-a^-$ tilt system which is commensurate with parallel Bi displacements along the $[111]_p$ direction [Glazer, 1972, Glazer, 1975]. According to Baettig et al. the ferroelectric order and the spontaneous polarization in $BiFeO_3$ result from the Bi^{3+} lone pair $6s^2$ electron which is sterochemically active [Baettig *et al.*, 2005]. A-site doping of $BiFeO_3$ with smaller sized RE dopants not only distorts the cation spacing between the FeO_6 octahedra (which can led to the further rotation of the octahedra) but also modifies the ferroelectric order [Baettig *et al.*, 2005, Cheng *et al.*, 2009].

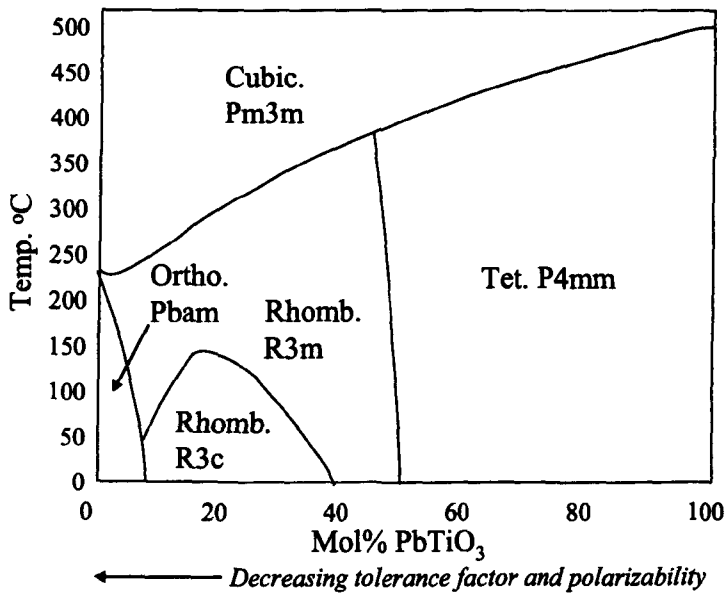

Figure 6.1. $Pb(Zr,Ti)O_3$ phase diagram.

The effect of the modifying the average ionic radius or tolerance factor (t) by cation substiton in the perovskite structure may be generally understood using the approach of [Goldschmidt, 1926, Reaney *et al.*, 1994]. Reaney et al. showed that the t gives an indication of the tilt transition temperature and the type of octahedral tilting likely to occur in any given system. In their study, Reaney et al. proposed that for $0.985 < t < 1.06$ perovskites are untilted, for $0.964 < t < 0.985$ they are tilted in antiphase only and for $t < 0.964$ they exhibit mixed in-phase and anti-phase tilting [Reaney *et al.*, 1994].

Tolerance factors calculated for the end member of the RE-doped $BiFeO_3$ solid solutions are listed in Table 6.1. All tolerance factor values are less than 0.964 and thus according to Reaney et al. all the end member ceramics should exhibit both in-phase and anti-phase tilting [Reaney *et al.*, 1994]. The orthoferrites ($REFeO_3$) have an $a^-a^-c^+$ tilt system (*Pnma* symmetry) and thus have mixed in-phase and antiphase tilting in agreement with [Reaney et

al., 2004]. However, $BiFeO_3$ has an $a^-a^-a^-$ tilt system and thus is tilted in antiphase only, in disagreement with [Reaney et al., 2004]. In the cuboctahedral cage, the Bi ion is highly polarisable and below T_C (830 °C) ferroelectric displacements along $[111]_p$ couple strongly to the octahedral rotations and force the structure to adopt a commensurate rhombohedal tilt system. In the absence of the ferroelectric displacements, i.e. above T_C in the paraelectric region, the structure reverts to an $a^-a^-c^+$ tilt system in which there are mixed in-phase and antiphase rotations. Moreover, in the $a^-a^-c^+$ tilt system, the A-site cations are known to displace in antiparallel along the $<110>_p$ giving rise to extra superstructure reflections at the $½\{eeo\}_p$ positions. Thus, above T_C, $BiFeO_3$ has antiparallel cation displacements and below T_C parallel ferroelectric displacements.

Table 6.1. Tolerance factor for the perovskites end members for the doped systems.

Composition	$BiFeO_3$	$LaFeO_3$	$NdFeO_3$	$SmFeO_3$	$GdFeO_3$
Tolerance factor	0.96	0.95	0.93	0.92	0.91

Figure 6.2 and 6.3 are plots of average tolerance factor and average A-site polarizability, respectively, versus T_C. As the average tolerance factor and A-site ionic polarisability decrease, T_C decreases. However, across the Lanthanide series, ionic polarisability is directly proportional to ionic radius and therefore it is difficult to distinguish which of the two crystallochemical factors is most important in controlling T_C in RE doped $BiFeO_3$.

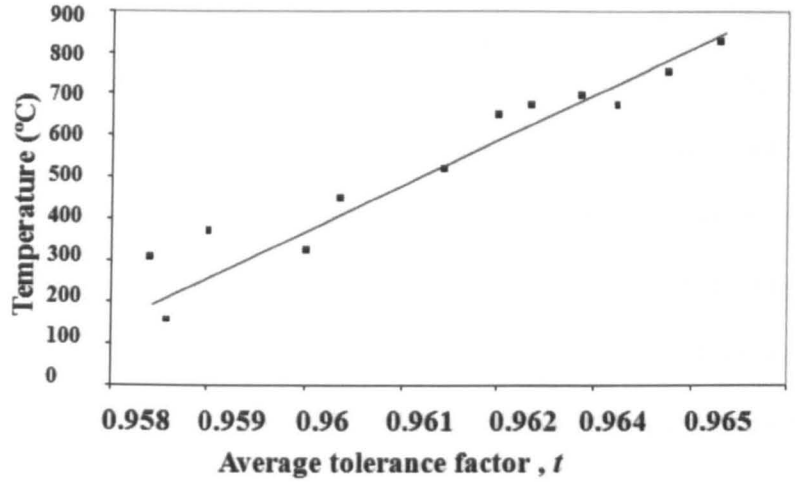

Figure 6.2. Plot of T_C versus tolerance factor for all compositions where DSC reliably indicates a phase transition.

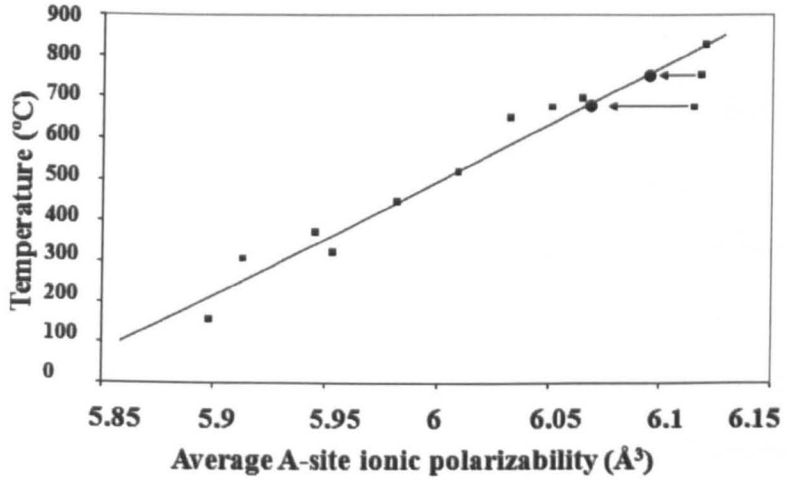

Figure 6.3. Plot of average A-site ionic polarizability for all compositions where DSC reliably indicates a phase transition. Data points using a modified polarizability for $La^{3+} \approx 5.5$ $\mathring{A}^3$ are arrowed.

In the case of RE-doped $BiFeO_3$, T_C decreases with decrease in tolerance factor and it is more likely therefore that the linear relationship of tolerance factor with T_C for RE-doped $BiFeO_3$ is secondary to that with average A-site ionic polarisability. It should be noted that the values of ionic polarisability and ionic radii were obtained from Shannon [Shannon, 1993, Shannon and Prewitt, 1969]. It is evident from the graph in Figure 6.3, that the average A-site ionic polarisabilities for 5% and 10% La-doped samples are anomalous and do not fit the linear trend. The polarizabilities for Gd^{3+}, Sm^{3+}, Nd^{3+}, La^{3+} and Bi^{3+} are quoted as 4.37, 4.74, 5.01, 6.07 and 6.12 $Å^3$, respectively, by [Shannon, 1993]. Within the highly distorted environment of the *R3c*, ferroelectric cell which is dominated by large A-site ion off centring along $[111]_p$, a polarizability of 6.07 $Å^3$ seems too large in comparison with that of Bi^{3+} 6.12 $Å^3$ and a value of ~5.5 $Å^3$ is more likely. If this value is assumed, a linear of fit with T_C vs composition is obtained for all RE doped compositions, Figure 6.3.

From Figures 6.2 and 6.3, it is clear that tolerance factor and average polarzability decrease in RE-doped $BiFeO_3$ with increase in RE concentration: a situation which replicates that observed in $Pb(Zr,Ti)O_3$ as Zr concentration increases. Moreover there is competition in the phase diagram between parallel and antiparallel A-site displacements based on the crystal chemstry of the end members, as discussed above. The net result is a strong driving force to stabilise a $PbZrO_3$ like phase intermediate between the rhombohedral ferroelectric and the orthorhombic orthoferrite structures. The transition from the high temperature $a^-a^-c^+$ *Pnma* cell to the $a^-a^-a^-$ *R3c* in $BiFeO_3$ is 1st order and therefore discontinuous [Arnold *et al.*, 2009]. From a group theoretical perspective, the transition beween the $a^-a^-c^+$ and $a^-a^-a^-$ tilt systems cannot occur directly [Howard and Stokes, 1998] and requires an intermediate step. One possible intermediate tilt system is $a^-a^-c^0$ which is compatible with the antiferroelectric

displacements that quadruple the cell in $PbZrO_3$. Overall therefore, there are several strong crystallochemical factors which encourage the stabilisation of an antiferroelectric cell in RE-doped $BiFeO_3$.

The $PbZrO_3$-like phase has been observed in all RE-doped $BiFeO_3$ systems to date [Karimi *et al.*, 2009]. Kan, Takeuchi anc co-workers, concluded that there is a universal behaviour driven by the crystallochemical factors discussed above [Kan *et al.*, 2010]. Figure 6.4 shows preliminary phase diagrams for several RE-doped $BiFeO_3$ systems which illustrate concisely the points raised. It should be noted that as the ionic radii and polarisability of the dopant RE ions decreases the critical concentration to induce structural transitions decreases, i.e. for Gd with the smallest ionic radius and lowest polarisability 10% dopant is sufficient to induce the transition while for La with the largest ionic radius more than 15% dopant is essential. This effect has also been observed in combinatorial studies of similar systems by Takeuchi and co-workers. These authors attributed the effect to a hydrostatic pressure caused by the smaller radii of the RE ions [Kan et al., 2010]. This explanation however, is incomplete in that it only takes into account the effect of the ionic radius and ignores the decrease in ionic polarisability which additionally occurs across the Lanthanide series. Similar arguments to that of Kan et al. have been used in previous classic texts, e.g. Jaffe et al. argued that in barium titanate, the isovalent substitution of Ba by Sr induces the same kind of changes in the lattice parameter and T_C as the changes caused by an external hydrostatic pressure [Jaffe *et al.*, 1971]. As part of their conclusions, Kan, Takeuchi and coworkers proposed a phase diagram of average ionic radii vs temperature for these compounds, Figure 6.5, indicating that the average ionic radii is the critical factor that controls the structura properties of RE-doped $BiFeO_3$ [Kan *et al.*, 2010]. The weakness of this argument as illustrated in Figures 6.2

and 6.3 and alluded to above, is that the ionic polarisability and radii of the lanthanide ions are intimately linked and each decreases systematically with increase in atomic number across the series so it is diffiuclt to state unambiguously which of the two is the dominant crysallochemcial factor.

It is interesting to note that in the study by Kan, Takeuchi and co-workers, there is a curvature to the line of T_C which is apparent due to their combinatorial pulse laser deposition thin film technique which ensures that there are many more compositional data points accessible. The origin of this curavature is still open to debate and requires further study.

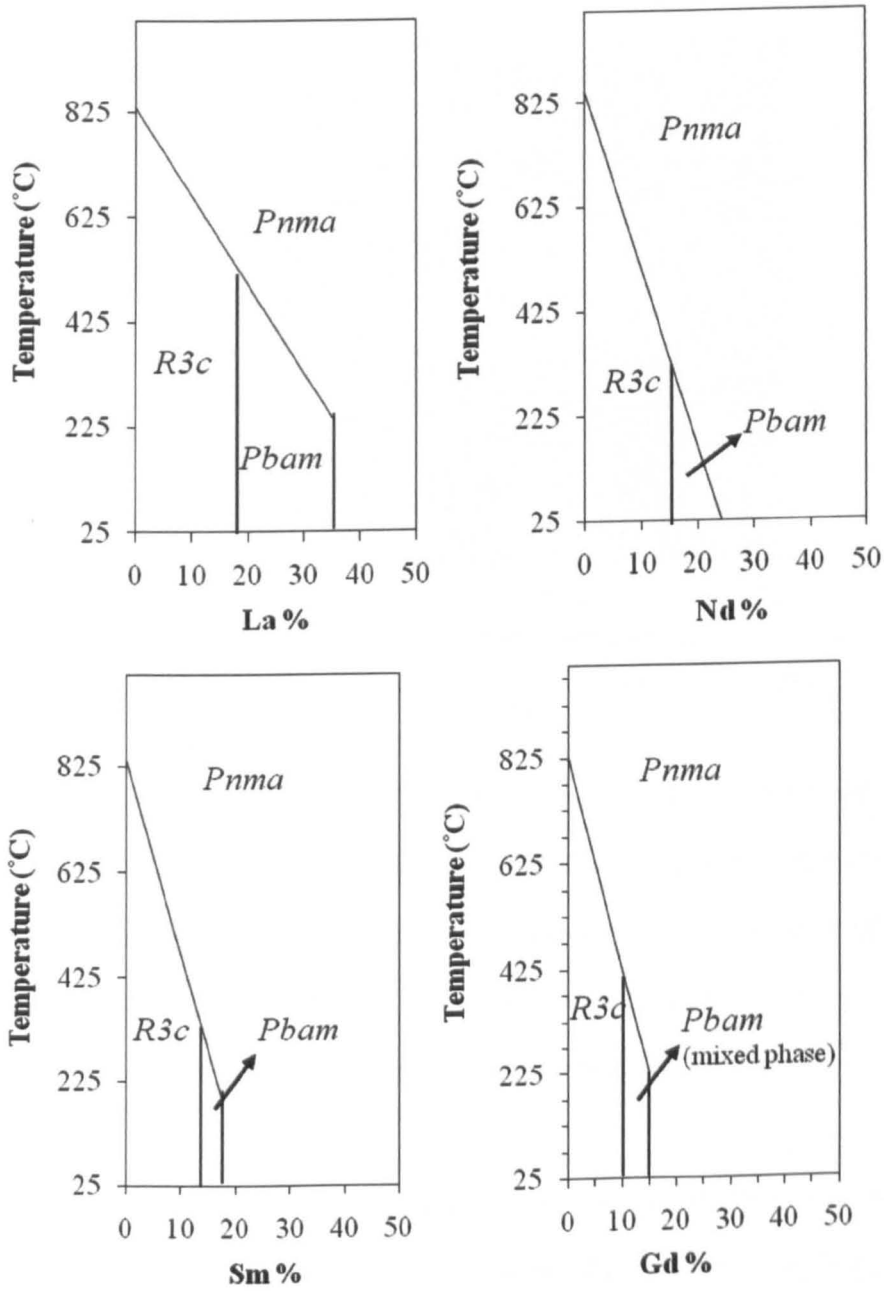

Figure 6.4. Preliminary phase diagrams for RE-doped $BiFeO_3$ derived using a combination of XRD, DSC, Raman, and TEM data.

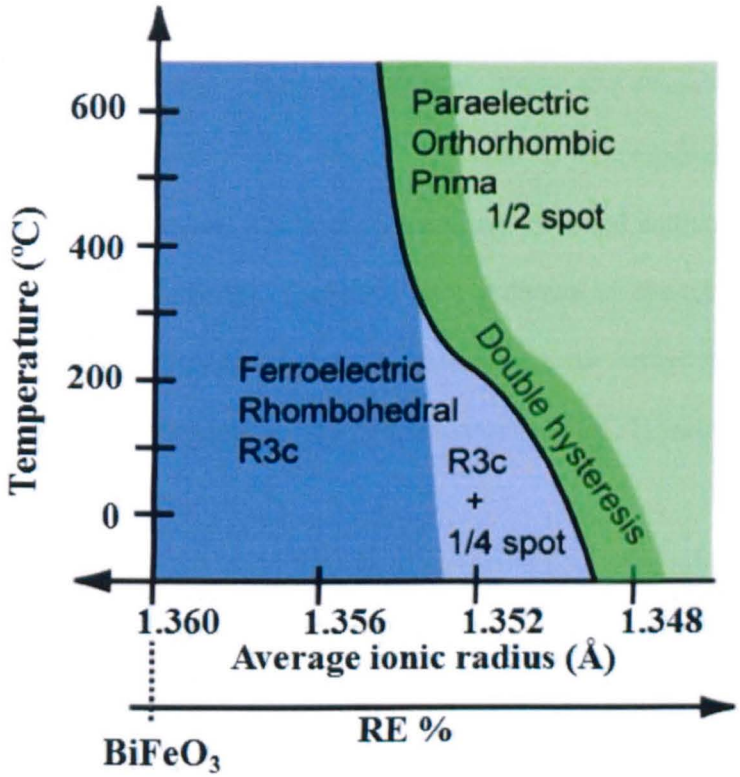

Figure 6.5. Proposed phase diagram for RE-substituted $BiFeO_3$. The black line represents the structural phase boundary between rhombohedral *R3c* in blue and the orthorhombic *Pnma* in green. At lower temperature side, the $PbZrO_3$-like phase is observed in the purple region (*R3c* + ¼ spot). The double hysteresis loop behavior as explained later emerges in the region in dark green [Kan, Takeuchi and co-workers, 2010].

In the present study, the *Pbam* model has been used to analyze the temperature dependence of the structural parameters for the $PbZrO_3$-like phase. RE substitution of Bi in $BiFeO_3$ is known to induce a stronger ferromagnetic response, which has been attributed to modification of the spiral modulation [Nalwa and Garg, 2008, Yuan and Or, 2006]. On heating, the $PbZrO_3$-like *Pbam* structure transforms to orthoferrite *Pnma* structure which is

accompanied by the large discontinuous volume change, similar to the *R3c* ro *Pnma* transition in $BiFeO_3$ [Levin *et al.*, 2010, Arnold *et al.*, 2009]. The *Pbam* to *Pnma* transition occurs in the antiferromagnetic state, Figure 6.6, and is accompanied by abrupt 90° reorientation of magnetic dipoles, within the same G-type ordered antiparallel array, which manifests itself in the macroscopic properties as a pronounced change in magnetization [Levin *et al.*, 2010]. Despite nominal G-type antiferromagnetic ordering, the $PbZrO_3$-like phase exhibits a robust ferromagnetic response [Levin *et al.*, 2010] most likely caused by canting of magnetic moments.

Studies of the bulk ferroelectric properties in this contribution were inhibited by the high conductivity of the samples under large drive fields. In contrast, however, Takeuchi and co-workers were able to measure ferroelectric properties of their Sm-doped thin film compositions, Figure 6.7, [Kan *et al.*, 2010]. They concluded that the ferroelectric properties of the RE-doped $BiFeO_3$ thin films follow the same patterns irrespective of the RE-type. Figure 6.7 exhibits the room temperature polarization vs electric field hysteresis loops for RE-doped $BiFeO_3$ thin films as a function of the average radius of the A-site ion ($r_{average}$).

The hysteretic behaviour follows a general trend in which square loops characteristic of a ferroelectric phase are present at >1.352 Å. These loops then collapse to give linear behaviour for an average A-site radius of 1.345 Å. The double hysteresis loops in the intermediate region $1.352<r_{average}<1.345$ was initially interpreted as arising form AFE switching but in later publications, e.g. [Kan *et al.*, 2010], they were attributed to a field induced 1st order transition in compositions whose T_C was marginally below room temperature.

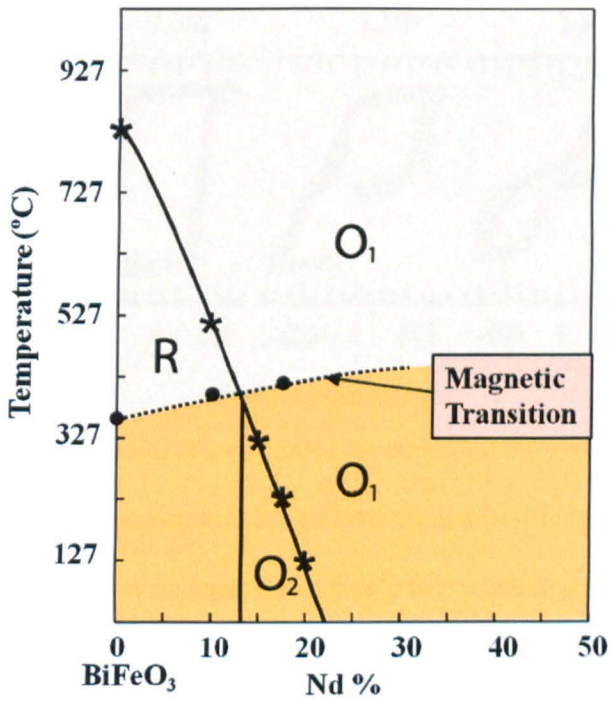

Figure 6.6. Schematic phase diagram indicating structural and magnetic transitions in the Nd doped $BiFeO_3$. The temperatures of the magnetic transitions were inferred from magnetic measurements [Levin, Karime and co-workers, 2011].

Overall, the results indicate a very intimate coupling between the displacive (tilting, cation displacements) and magnetic order parameters which is manifested in the well-defined displacement and magnetization anomalies at the temperatures of the magnetic and structural phase transitions.

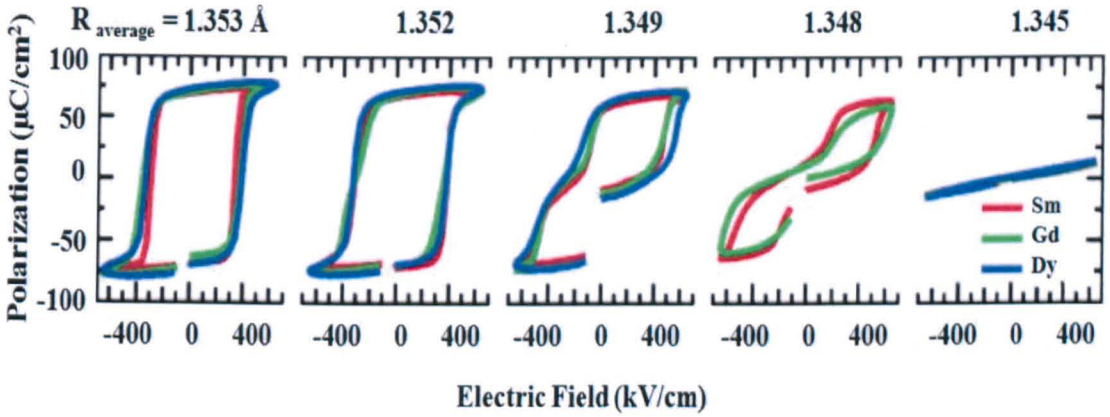

Figure 6.7. Polarization hysteresis loops across the structural transition for RE-substituted $BiFeO_3$ thin films at Room-temperature for 200 nm-thick thin films plotted for $r_{average}$. For each $r_{average}$, the hysteresis loops collapse into a single curve which demonstrates a universal behavior in ferroelectric properties of RE-doped $BiFeO_3$ [Kan *et al.*, 2010].

6.1.References

ARNOLD, D. C., KNIGHT, K. S., MORRISON, F. D. & LIGHTFOOT, P. (2009) *Ferroelectric-Paraelectric Transition in $BiFeO_3$: Crystal Structure of the Orthorhombic beta Phase.* Physical Review Letters, **102,** 027602.

BAETTIG, P., EDERER, C. & SPALDIN, N. A. (2005) *First principles study of the multiferroics $BiFeO_3$, Bi_2FeCrO_6, and $BiCrO_3$: Structure, polarization, and magnetic ordering temperature.* Physical Review B, **72,** 214105.

CHENG, C. J., KAN, D., LIM, S. H., MCKENZIE, W. R., MUNROE, P. R., SALAMANCA-RIBA, L. G., WITHERS, R. L., TAKEUCHI, I. & NAGARAJAN, V. (2009) *Structural transitions and complex domain structures across a ferroelectric-to-antiferroelectric phase boundary in epitaxial Sm-doped $BiFeO_3$ thin films.* Physical Review B, **80,** 014109.

GLAZER, A. M. (1972) *The Classification of Tilted Octahedra in Perovskites.* Acta Crystallographica, **B28,** 3384.

GLAZER, A. M. (1975) *Simple Ways of Determining Perovskite Structures.* Acta Crystallographica, **A31,** 756.

GOLDSCHMIDT, V. M. (1926) *Geochemische Verteilungsgesetze Der Elemente.* **Skrifter utg. Av det Norske Viedenskaps-Akademi i Oslo,** 1.

HOWARD, C. J. & STOKES, H. T. (1998) *Group-theoretical analysis of octahedral tilting in perovskites.* Acta Crystallographica, **B54,** 782.

JAFFE, B., COOK, W. R. J. & JAFFE, H. (1971) *Piezoelectric Ceramics,* London, Academic Press.

KAN, D., PALOVA, L., ANBUSATHAIAH, V., CHENG, C. J., FUJINO, S., NAGARAJAN, V., RABE, K. M. & TAKEUCHI, I. (2010) *Universal Behavior and Electric-Field-Induced Structural Transition in Rare-Earth-Substituted $BiFeO_3$.* Advanced Functional Materials, **20,** 1108.

KARIMI, S., REANEY, I. M., HAN, Y., POKORNY, J. & STERIANOU, I. (2009) *Crystal Chemistry and Domain Structure of Rare-Earth Doped $BiFeO_3$ Ceramics.* Journal of Materials Science, **44,** 5102.

LEVIN, I., KARIMI, S., PROVENZANO, V., DENNIS, C. L., WU, H., COMYN, T. P., STEVENSON, T. J., SMITH, R. I. & REANEY, I. M. (2010) *Reorientation of Magnetic Dipoles at the Antiferroelectric-Paraelectric Phase Transition of $Bi_{1-x}Nd_xFeO_3$ $(0.15 \leq x \leq 0.25)$.* Physical Review B, **81,** 020103.

LEVIN, I., KARIMI, S., TUCKER, M. G., WU, H., PROVENZANO, V., DENNIS, C. L., T.COMYN & REANEY, I. M. (2011) *Displacive Phase Transitions and Magnetic Structure in Nd-Substituted $BiFeO_3$.* Chemistry of Materials, **Submitted for publication.**

MICHEL, C., MOREAU, J.-M., ACHENBACH, G. D., GERSON, R. & JAMES, W. J. (1969) *Atomic Structure of Two Rhombohedral Ferroelectric Phases in the $Pb(Zr,Ti)O_3$ Solid Solution Series.* Solid State Communications, **7,** 701.

NALWA, K. S. & GARG, A. (2008) *Phase Evolution, Magnetic and Electrical Properties in Sm-Doped Bismuth Ferrite.* Journal of Applied Physics, **103,** 044101.

REANEY, I. M., COLLA, E. L. & SETTER, N. (1994) *DIELECTRIC AND STRUCTURAL CHARACTERISTICS OF BA-BASED AND SR-BASED COMPLEX PEROVSKITES AS A FUNCTION OF TOLERANCE FACTOR.* Japanese Journal of Applied Physics Part 1-Regular Papers Short Notes & Review Papers, **33,** 3984.

SHANNON, R. D. (1993) *Dielectric Polarizabilities of Ions in Oxides and Fluorides* Journal of Applied Physics, **73,** 348.

SHANNON, R. D. & PREWITT, C. T. (1969) *Effective Ionic Radii in Oxides and Fluorides.* Acta Crystallographica, **B25,** 925.

SUAREZ, D., REANEY, I. M. & LEE, W. E. (2001) *Relation Between Tolerance Factor and Tc in Aurivillius Compounds.* Journal of Material Research, **16[11],** 3199.

WOODWARD, D. I. (2004) The Crystal Chemistry of Bismuth-Based Perovskite Solid Solutions. *Engineering Materials.* Sheffield, The University of Sheffield.

WOODWARD, D. I., KNUDSEN, J. & REANEY, I. M. (2005) *Review of crystal and domain structures in the $PbZr_xTi_{1-x}O_3$ solid solution.* Physical Review B, **72,** 104110.

YUAN, G. L. & OR, S. W. (2006) *Enhanced piezoelectric and pyroelectric effects in single-phase multiferroic $Bi_{1-x}Nd_xFeO_3$ (x=0-0.15) ceramics.* Applied Physics Letters, **88,** 062905.

Chapter 7: Conclusions

All RE doped $BiFeO_3$ compositions with less than 10% RE dopant were rhombohedral with *R3c* symmetry and exhibited, superstructure and orientational and translational domains characteristic of an anti-phase tilted, ferroelectric perovskite. At higher RE concentrations, an orthorhombic structure was stabilised with Pnma symmetry whose Glazer tilt system ($a^-a^-c^+$) was identical to that of the $REFeO_3$, orthoferrite, end member. However, at the phase boundary between the orthoferrite and rhombohedral cell, a new $PbZrO_3$-like orthorhombic phase was stabilised. The structure refined well using neutron and X-ray diffraction data to the Pbam, $PbZrO_3$ cell, ($\sqrt{2}a_c, 2\sqrt{2}a_c, 2a_c$) but electron diffraction revealed a further doubling of the unit cell in the *c* direction to give a unit cell, $\sqrt{2}a_c, 2\sqrt{2}a_c, 4a_c$. The origin of the further cell doubling along *c* remains unknown.

T_C for all compositions decreased with decreasing average tolerance factor and A-site ionic polarizability preliminary phase diagrams for RE-doped $BiFeO_3$ for the studied RE dopants have been constructed. Subsequent to publication of the preliminary phase diagrams, they were broadly confirmed by Takeuchi and co-workers using combinatorial thin film studies.

Rietveld refinements of neutron powder diffraction data revealed similarities between the *R3c* to *Pnma* and *Pbam* to *Pnma* phase transitions. In particular, both structural transitions were accompanied by large discontinuous lattice volume expansion in the low-temperature *R3c* and *Pbam* phase. The PE-AFE transition between the two orthorhombic structures occurred below T_N in the G-type, antiferromagnetically ordered state and was accompanied by abrupt 90° reorientation of magnetic dipoles which manifested itself as an abrupt change of magnetization and coercive field.

Dielectric measurements as a function of temperature illustrated a significant decrease in tanδ as a function of increase in RE concentration. However, broad frequency dependent peaks in permittivity were often observed suggesting that space-charge effects still dominated the dielectric properties despite RE-doping. At no stage where peaks in permittivity associated with structural phase transitions observed. Polarisation-field measurements did not reveal any evidence of classic ferroelectric switching.

To make a final conclusion on the usefulness of different structural characterisation techniques used in this work, a summary of the strengths and weaknesses of each technique is listed below.

XRD is the most readily available characterisation technique and although it was initially helpful in finding the structural phase changes in $BiFeO_3$, it is insensitive to the displacement of anions and thus not useful in establishing the anion location and identification of the space groups dominated by such displacements.

SEM gave confidence that the ceramics were of sufficient quality in terms of porosity and second phase to warrant further study.

TEM- Electron Diffraction facilitated the study of single domains and weak cell doubling phenomena in perovskites. It was used extensively to study superlattice reflections and associated domain structure as a function of composition and temperature. Initially, space group symmetries were determined by electron diffraction prior to full structural refinement. Although only qualitative, it is more readily available in comparison to, e.g., neutron diffraction, which may only be accessed through central resources.

Raman Spectroscopy was primarily used to determine the temperature and compositions at which structural phase transitions occur. No attempt was made to quantify or model the

Raman spectra but the rapid turnaround time and the fact that it is non-destructive made this technique invaluable for determination of preliminary phase diagrams

Neutron Diffraction provides better signal to background ratio than X-ray and is sensitive to weak superlattice reflections relating to the distortion of the O-sublattice. The use of neutron diffraction in this study was the most important technique for quantitative determination of anionic positions. The low atomic scattering factor for oxygen makes anion disorder in perovskites very difficult to recognize by X-ray diffraction.

At the end it is worth mentioning that in the author's view a combination of in-situ electron and neutron diffraction gave the most effective and comprehensive overview of the structure of different phases in rare earth doped $BiFeO_3$.

Chapter 8: Future Work

- Assigning vibrational modes to strong bands observed in Raman spectra; currently under investigation, initiated within the group through collaboration with the Academy of Science, Czech Republic and exemplified by the paper:

  J. Hlinka, J. Pokorny, S. Karimi and I.M. Reaney, "Angular dispersion of oblique phonon modes by Raman scattering in $BiFeO_3$" Physical Review B, January 2011.

- Fabricate and characterise thin films of Nd-doped $BiFeO_3$. This is already underway at the University of Leeds on a joint programme with Prof. Bell. In addition, targets of Sm doped compostions have been sent to Prof. I.Takeuchi's research group at The University of Maryland, USA and to Prof. N. Valanoor's research group at The University of New South Wales, Australia.

- Investigate dopant strategies to reduce conductivity in RE-doped $BiFeO_3$ and therefore facilitate more extensive investigation into the dielectric properties of these systems. This research is already on-going via an in-house continuation of my project with a Ph.D student, K. Kalantari. The first article has been accepted:

  K. Kalantari, S. Karimi, D.C. Sinclair, I. Sterianou and I.M. Reaney, "Ti-doping to reduce conductivity in $Bi_{0.85}Nd_{0.15}FeO_3$ Ceramics" Advanced Functional Materials, Accepted March 2011.